Five-Year Wilkinson Microwave Anisotropy Probe (WMAP[1]) Observations: Likelihoods and Parameters from the WMAP data

J. Dunkley[2,3,4], E. Komatsu[5], M. R. Nolta[6], D. N. Spergel[3,7], D. Larson[8], G. Hinshaw[9] , L. Page[2], C. L. Bennett[8], B. Gold[8], N. Jarosik[2], J. L. Weiland[10], M. Halpern[11], R. S. Hill[10], A. Kogut[9], M. Limon[12], S. S. Meyer[13], G. S. Tucker[14], E. Wollack[9], E. L. Wright[15]

j.dunkley@physics.ox.ac.uk

ABSTRACT

This paper focuses on cosmological constraints derived from analysis of *WMAP* data alone. A simple ΛCDM cosmological model fits the five-year *WMAP* temperature and polarization data. The basic parameters of the model are consistent with the three-year data and now better constrained: $\Omega_b h^2 = 0.02273 \pm 0.00062$, $\Omega_c h^2 = 0.1099 \pm 0.0062$, $\Omega_\Lambda = 0.742 \pm 0.030$, $n_s = 0.963^{+0.014}_{-0.015}$, $\tau = 0.087 \pm 0.017$, $\sigma_8 = 0.796 \pm 0.036$. With five years of polarization data, we have measured the optical depth to reionization, $\tau > 0$, at 5σ significance. The redshift of an instantaneous reionization is constrained to be $z_{\rm reion} = 11.0 \pm 1.4$ with 68% confidence. The 2σ lower limit is $z_{\rm reion} > 8.2$, and the 3σ limit is $z_{\rm reion} > 6.7$. This excludes a sudden reionization of the universe at $z = 6$ at more than 3.5σ significance, suggesting that reionization was an extended process. Using two different methods for polarized foreground cleaning, and foreground marginalization, we get consistent estimates for the optical depth. This cosmological model also fits small-scale CMB data, and a range of astronomical data measuring the expansion rate

[1] *WMAP* is the result of a partnership between Princeton University and NASA's Goddard Space Flight Center. Scientific guidance is provided by the *WMAP* Science Team.

[2] Dept. of Physics, Jadwin Hall, Princeton University, Princeton, NJ 08544-0708

[3] Dept. of Astrophysical Sciences, Peyton Hall, Princeton University, Princeton, NJ 08544-1001

[4] Astrophysics, University of Oxford, Keble Road, Oxford, OX1 3RH, UK

[5] Univ. of Texas, Austin, Dept. of Astronomy, 2511 Speedway, RLM 15.306, Austin, TX 78712

[6] Canadian Institute for Theoretical Astrophysics, 60 St. George St, University of Toronto, Toronto, ON Canada M5S 3H8

[7] Princeton Center for Theoretical Physics, Princeton University, Princeton, NJ 08544

[8] Dept. of Physics & Astronomy, The Johns Hopkins University, 3400 N. Charles St., Baltimore, MD 21218-2686

[9] Code 665, NASA/Goddard Space Flight Center, Greenbelt, MD 20771

[10] Adnet Systems, Inc., 7515 Mission Dr., Suite A1C1 Lanham, Maryland 20706

[11] Dept. of Physics and Astronomy, University of British Columbia, Vancouver, BC Canada V6T 1Z1

[12] Columbia Astrophysics Laboratory, 550 W. 120th St., Mail Code 5247, New York, NY 10027-6902

[13] Depts. of Astrophysics and Physics, KICP and EFI, University of Chicago, Chicago, IL 60637

[14] Dept. of Physics, Brown University, 182 Hope St., Providence, RI 02912-1843

[15] PAB 3-909, UCLA Physics & Astronomy, PO Box 951547, Los Angeles, CA 90095-1547

and clustering of matter in the universe. We find evidence for the first time in the CMB power spectrum for a non-zero cosmic neutrino background, or a background of relativistic species, with the standard three light neutrino species preferred over the best-fit ΛCDM model with $N_{\text{eff}} = 0$ at $> 99.5\%$ confidence, and $N_{\text{eff}} > 2.3$ (95% CL) when varied. The five-year *WMAP* data improve the upper limit on the tensor-to-scalar ratio, $r < 0.43$ (95% CL), for power-law models, and halve the limit on r for models with a running index, $r < 0.58$ (95% CL). With longer integration we find no evidence for a running spectral index, with $dn_s/d\ln k = -0.037 \pm 0.028$, and find improved limits on isocurvature fluctuations. The current *WMAP*-only limit on the sum of the neutrino masses is $\sum m_\nu < 1.3$ eV (95% CL), which is robust, to within 10%, to a varying tensor amplitude, running spectral index or dark energy equation of state.

Subject headings: cosmic microwave background, cosmology: observations, polarization, early universe

1. Introduction

The *Wilkinson Microwave Anisotropy Probe* (*WMAP*), launched in 2001, has mapped out the Cosmic Microwave Background with unprecedented accuracy over the whole sky. Its observations have led to the establishment of a simple concordance cosmological model for the contents and evolution of the universe, consistent with virtually all other astronomical measurements. The *WMAP* first-year and three-year data have allowed us to place strong constraints on the parameters describing the ΛCDM model, a flat universe filled with baryons, cold dark matter, neutrinos, and a cosmological constant, with initial fluctuations described by nearly scale-invariant power law fluctuations, as well as placing limits on extensions to this simple model (Spergel et al. 2003, 2007). With all-sky measurements of the polarization anisotropy (Kogut et al. 2003; Page et al. 2007), two orders of magnitude smaller than the intensity fluctuations, *WMAP* has not only given us an additional picture of the universe as it transitioned from ionized to neutral at redshift $z \sim 1100$, but also an observation of the later reionization of the universe by the first stars.

In this paper we present cosmological constraints from *WMAP* alone, for both the ΛCDM model and a set of possible extensions. We also consider the consistency of *WMAP* constraints with other recent astronomical observations. This is one of seven five-year *WMAP* papers. Hinshaw et al. (2008) describe the data processing and basic results, Hill et al. (2008) present new beam models and window functions, Gold et al. (2008) describe the emission from Galactic foregrounds, and Wright et al. (2008) the emission from extra-Galactic point sources. The angular power spectra are described in Nolta et al. (2008), and Komatsu et al. (2008) present and interpret cosmological constraints based on combining *WMAP* with other data.

WMAP observations are used to produce full-sky maps of the CMB in five frequency bands centered at 23, 33, 41, 61, and 94 GHz (Hinshaw et al. 2008). With five years of data, we are now able to place better limits on the ΛCDM model, as well as to move beyond it to test the composition of the universe, details of reionization, sub-dominant components, characteristics of inflation, and primordial fluctuations. We have more than doubled the amount of polarized data used for cosmological analysis, allowing a better measure of the large-scale E-mode signal (Nolta et al. 2008). To this end we describe an alternative way to remove Galactic foregrounds from low resolution polarization maps in which Galactic emission is marginalized over, providing a cross-check of our results. With longer integration we also better probe the second and third acoustic peaks in the temperature angular power spectrum, and have many more year-to-year difference maps available for cross-checking systematic effects (Hinshaw et al. 2008).

The paper is structured as follows. In §2 and §3 we focus on methodology, starting in §2 by describing a new method for cleaning the polarization maps using Gibbs sampling, and presenting estimated component maps for CMB, synchrotron, and dust emission. These are used to cross-check the standard template-cleaned results. The CMB likelihood and parameter estimation methodology is described in §3. We describe a fast method for computing the large-scale temperature likelihood, based on work described in Wandelt et al. (2004), which also uses Gibbs sampling, and outline more efficient techniques for sampling cosmological parameters. In §4 we present cosmological parameter results from five years of *WMAP* data for the ΛCDM model, and discuss their consistency with recent astronomical observations. Finally we consider constraints from *WMAP* alone on a set of extended cosmological models in §5, and conclude in §6.

2. Bayesian estimation of low resolution polarization maps

The three-year *WMAP* observations (Page et al. 2007) showed that polarized diffuse emission from our Galaxy dominates the primordial signal over much of the sky, particularly at the lower frequencies probed by *WMAP*. Accurate estimation of the CMB signal at large angular scales therefore poses a significant challenge. In this section, we present results from a new method for estimating the polarized CMB signal, which serves both as a cross-check of the template cleaning method used by *WMAP*, and as a framework in which errors due to foreground uncertainty are more rigorously propagated. We start by briefly reviewing our understanding of diffuse polarized Galactic components in the microwave regime. A more detailed review was made in Page et al. (2007).

Both synchrotron and thermal dust emission are polarized to some degree due to the Galactic magnetic field, measured to have a coherent spiral structure parallel to the Galactic plane, as well as a significant turbulent component (Spitzer 1998; Beck 2001; Vallée 2005; Han 2006). The effective strength of the field is of order $\sim 10\ \mu G$, and is thought to be split roughly equally between the coherent and turbulent components (Crutcher et al. 2003). Synchrotron emission is produced by relativistic cosmic-ray electrons accelerated in this magnetic field (see Strong et al. (2007) for a review of cosmic ray propogation). For electrons with a power law distribution of energies

$$N(E) \propto E^{-p}, \tag{1}$$

the frequency dependence of the emission is characterized by antenna temperature $T(\nu) \propto \nu^\beta$ with spectral index $\beta = -(p+3)/2$, with typically $\beta \sim -3$ (Rybicki & Lightman 1979). However, since synchrotron loss is proportional to E^2, this means that older sources of electrons should have a lower energy distribution and a steeper spectral index of synchrotron emission, compared to regions of recently injected electrons. This leads to a synchrotron index that varies over the sky (Lawson et al. 1987; Reich & Reich 1988) and is expected to steepen away from the Galactic plane (Strong et al. 2007), with evidence of this behavior seen in the *WMAP* data (Bennett et al. 2003). Since the cosmic-ray electrons emit radiation almost perpendicular to the Galactic magnetic field in which they orbit, they can produce polarization fractions as high as $\sim 75\%$ (Rybicki & Lightman 1979), although integration of multiple field directions along a line of sight reduces this level. The fractional polarization observed at radio frequencies in the range 408 MHz - 2.4 GHz is further lowered due to Faraday rotation (Duncan et al. 1995; Uyaniker et al. 1999; Wolleben et al. 2006), but the integrated signal observed by *WMAP* at 23 GHz reaches upper limits of $\sim 50\%$ (Kogut et al. 2007).

Thermal emission of sub-micron sized dust grains, which absorb starlight radiation and re-emit thermally in the far infra-red with typical spectral index $\beta \sim 2$, is the dominant Galactic component at the highest frequencies probed by *WMAP*. Its intensity has been well measured by the *IRAS* and *COBE* missions and extrapolated to microwave frequencies by Finkbeiner et al. (1999). Polarization arises since grains tend

to align their long axes perpendicular to the Galactic magnetic field via, for example, the Davis-Greenstein mechanism (Davis & Greenstein 1951), and depending on their composition can be polarized up to a modeled maximum of $\sim 20\%$ parallel to their long axes (e.g., Hildebrand & Dragovan (1995)). Observations of starlight, polarized perpendicular to the dust grains, are consistent with this picture (Heiles 2000; Berdyugin et al. 2001), as are the three-year *WMAP* observations (Page et al. 2007; Kogut et al. 2007). A population of smaller dust grains formed of polycyclic aromatic hydrocarbons may also emit a significant amount of microwave radiation due to electric dipole rotational emission (Draine & Lazarian 1999; Draine & Li 2007). This question is discussed in e.g. Hinshaw et al. (2007); Dobler & Finkbeiner (2007); Gold et al. (2008) with respect to the intensity signal observed by *WMAP*. However, these small spinning dust grains are not expected to be significantly polarized (Draine 2003). Other mechanisms for producing polarized emission, including magnetic dust (Draine & Lazarian 1999), have not been observed to be dominant.

Given these two polarized foreground components, the standard method used to clean the *WMAP* polarization maps involves subtracting synchrotron and dust template maps from the total, leaving a cleaned CMB map at the Ka, Q, and V bands (Page et al. 2007; Gold et al. 2008). The templates are assumed to be exact, such that the noise properties of the cleaned CMB maps are the same as the uncleaned maps, although the error is increased to account for the small CMB signal present in the synchrotron template (Page et al. 2007). This method has proved satisfactory for cosmological interpretation, but only the central two bands (Q and V) were used in the three-year *WMAP* analysis. To confidently use the low frequency *WMAP* bands we want an independent cross-check of the result, and ideally an improved method for marginalizing over foreground uncertainty. The method described here uses a Bayesian framework for estimating low resolution CMB, synchrotron, and dust maps. We use maps with HEALPix $N_{side} = 8$ [16], with pixels of side 7.2 degrees. The main products are maps, and a covariance matrix, of the polarized CMB Q and U components, marginalized over foreground uncertainty. A similar technique has also been developed by Eriksen et al. (2006, 2007) for estimating intensity maps, and has been applied to the three-year *WMAP* temperature maps. We provide a description of our method and the main results in this paper, but further details of the method and application to simulated maps are given in a separate paper (Dunkley et al. 2008).

2.1. Map estimation method

We model the total polarized emission in antenna temperature at frequency ν as

$$\mathbf{m}_\nu = f(\nu)\mathbf{A}_c + (\nu/\nu_K)^{\beta_s}\mathbf{A}_s + (\nu/\nu_W)^{\beta_d}\mathbf{A}_d + \mathbf{n}_\nu, \tag{2}$$

where $\mathbf{m}_\nu$ is a vector of length $2N_p$ containing the Stokes Q and U signal for the CMB, synchrotron and dust components. The amplitude vectors of each component are given by $\mathbf{A}_x$, where $x = c, s, d$ for CMB, synchrotron and dust respectively, defined at $\nu_K = 22.8$ GHz for CMB and synchrotron, and $\nu_W = 93.5$ GHz for dust. The Gaussian noise, $\mathbf{n}_\nu$, is quantified by the $2N_p \times 2N_p$ noise matrix at each band, $\mathbf{N}_\nu$, which includes pixel-pixel covariance and Q-U covariance. The spectral indices of the synchrotron and dust are given by β_x, and $f(\nu)$ converts thermodynamic temperature to antenna temperature (see Hinshaw et al. (2008)). Given the observed data $\mathbf{d}_\nu$, the joint probability distribution of the parameters $\mathbf{A}_x$ and β_x can be written as $p(\mathbf{A}, \beta|\mathbf{d}) = p(\mathbf{d}|\mathbf{A}, \beta)p(\mathbf{A}, \beta)$, with prior distribution $p(\mathbf{A}, \beta)$ and Gaussian likelihood

$$-2\ln p(\mathbf{d}|\mathbf{A}, \beta) = \sum_\nu (\mathbf{d}_\nu - \mathbf{m}_\nu)^T \mathbf{N}_\nu^{-1}(\mathbf{d}_\nu - \mathbf{m}_\nu) + c, \tag{3}$$

---

[16]The number of pixels is $12N_{side}^2$, where $N_{side} = 2^3$ for r3, or resolution 3 (Gorski et al. 2005).

with a normalization that appears as an additive term c in the log-likelihood. The objective is to sample from this distribution, to obtain the marginalized distribution for the CMB amplitudes,

$$p(\mathbf{A}_c|\mathbf{d}) = \int p(\mathbf{A}, \boldsymbol{\beta}|\mathbf{d})d\mathbf{A}_s d\mathbf{A}_d d\boldsymbol{\beta}, \tag{4}$$

as well as estimates for the Galactic components. The method is applied only at low resolution, for $N_p = 768$. We form the data vectors from the four lowest frequency *WMAP* bands (K, Ka, Q, V), giving $8N_p$ data points. We start with the co-added maps and N^{-1} matrices for each band at HEALPix $N_{\mathrm{side}} = 16$. We then degrade the maps and inverse noise matrices to $N_{\mathrm{side}} = 8$, using the full noise matrices.

In the general case the spectral indices could vary pixel-by-pixel, and could take different values for Q and U. A more general modeling would also allow for non power-law indices. However, for the dust component we fix $\beta_d = 1.7$ for all pixels, motivated by Finkbeiner et al. (1999). We show in Appendix A that changing this to $\beta_d = 2$ has no effect on our results. We allow the polarized synchrotron index to vary spatially, but fix the Q and U index to be the same for a given pixel. We also define $N_i < N_p$ regions of the sky within which β_s takes a common value, rather than allow it to take a unique value at each pixel, and impose a Gaussian prior of $\beta_s = -3.0 \pm 0.15$ on the index in each region. We do not allow for a steepening of the index in our fiducial model. These priors are motivated both by our noise levels and by our understanding of the emission process: even though we expect spatial variation due to the different ages of the electron populations, the electron diffusion rate limits how much the index can vary over a short range (Strong et al. 2000, 2007). We choose $N_i = 30$ in the fiducial model, with the choice of regions discussed further in Appendix A. The prior on the index range is rather tight, as indices of -2.7 and -3.3 are physically reasonable, and a more conservative prior would be preferred. However, we have found this to be necessary for numerical stability, and check that modifying the central value to $\beta_s = -2.8$ has little effect on our estimated CMB signal. We make no prior assumptions about the CMB or synchrotron Q and U amplitudes at each pixel, but impose a prior that the dust be $< 20\%$ polarized, using the dust map $\mathbf{I}_d$ at 94 GHz from Finkbeiner et al. (1999), hereafter FDS, as a tracer of the intensity. We additionally impose a Gaussian prior on the dust Stokes parameters of $[Q_d(\hat{n}), U_d(\hat{n})] = 0 \pm 0.2I_d(\hat{n})$. This is sufficiently broad that moving the central value of the prior to e.g. 5% of the dust map (rather than 0%), has a negligible effect on results.

The distribution is therefore described by $6N_p$ amplitudes and N_i synchrotron spectral indices. We cannot sample the joint distribution $p(\mathbf{A}, \boldsymbol{\beta}|\mathbf{d})$ directly, so we use Markov Chain Monte Carlo methods to draw samples from it. It can be sliced into two conditional distributions $p(\mathbf{A}|\boldsymbol{\beta}, \mathbf{d})$ and $p(\boldsymbol{\beta}|\mathbf{A}, \mathbf{d})$, so we can use Gibbs sampling to draw alternately from each conditional distribution, constructing a Markov chain with the desired joint distribution as its stationary distribution. The sampling would go as follows for the case of one A parameter and one β parameter: we start from some arbitrary point (A_i, β_i) in the parameter space. Then we draw

$$(A_{i+1}, \beta_{i+1}), (A_{i+2}, \beta_{i+2})... \tag{5}$$

by first drawing A_{i+1} from $p(A|\beta_i, d)$ and then drawing β_{i+1} from $p(\beta|A_{i+1}, d)$. Then we iterate many times. The result is a Markov chain whose stationary distribution is $p(A, \beta|d)$. A description of Gibbs sampling can be found in Gelfand & Smith (1990), and in the cosmological literature in Wandelt et al. (2004); Eriksen et al. (2007).

For the multivariate case $\mathbf{A}$ and $\boldsymbol{\beta}$ are now vectors, and so each vector is drawn in turn. For fixed $\boldsymbol{\beta}$, the conditional distribution $p(\mathbf{A}|\boldsymbol{\beta}, \mathbf{d})$ is a $6N_p$-dimensional Gaussian, so it is possible to directly draw a sample of all $6N_p$ amplitude parameters simultaneously. The mean and variance of such a sample for a given $\boldsymbol{\beta}$ vector are derived in Dunkley et al. (2008). It is a simple step, but computationally intensive. For fixed $\mathbf{A}$,

we cannot invert the distribution $p(\boldsymbol{\beta}|\mathbf{A}, \mathbf{d})$ to draw a sample. Instead we use the Metropolis algorithm to sample $\boldsymbol{\beta}$, which has only N_i elements. The Metropolis algorithm has been described in detail in e.g., Neal (1993); Lewis & Bridle (2002); Dunkley et al. (2005).

This combination of sampling steps is commonly known as Metropolis-within-Gibbs (e.g. Geweke & Tanizaki (2001)), and has been used in astronomy to estimate Cepheid distances (Barnes et al. 2003). The full sampling, drawing a new $\mathbf{A}$ and then a new $\boldsymbol{\beta}$ in turn until convergence, produces marginalized distributions for the CMB, synchrotron, and dust amplitudes, and synchrotron indices. We form maps of each component from the mean of the marginalized distribution,

$$\langle \mathbf{A}_x \rangle = \int p(\mathbf{A}_x|\mathbf{d})\mathbf{A}_x d\mathbf{A}_x = \frac{1}{n_{\mathrm{G}}} \sum_{i=1}^{n_{\mathrm{G}}} \mathbf{A}_x^i, \tag{6}$$

where the sum is over all n_{G} elements in the chain, and $\mathbf{A}_x^i$ is the ith chain element. The covariance matrices for $\mathbf{A}_x$, including off-diagonal terms, are estimated using the same method, summing over the chain components. In this analysis we work with low resolution maps with $N_p = 768$, since the computational costs of working at higher resolution are large and our main scientific goal is to determine the polarized CMB signal at large angular scale. Tests of this method on simulated maps, constructed with three-year *WMAP* noise properties, are described in Dunkley et al. (2008). The CMB and Galactic foreground maps, and their associated cosmological parameters, are recovered with the expected χ^2 between input and output components.

2.2. Results: Low resolution polarization maps

Figures 1 and 2 show maps of the mean values and 1σ errors for the marginalized CMB, synchrotron, and dust amplitudes. We first consider the CMB results. The noise patterns for both Q and U in Figure 2 are consistent with what we expect: in regions of low Galactic emission, the errors are dominated by instrumental noise. As the Galactic plane is approached, errors from foreground uncertainty begin to dominate, in particular where the dust contribution is most uncertain. As opposed to template cleaning, which produces CMB maps at each frequency observed, this method recovers a single Q and U polarization map, and so has higher signal-to-noise than any of the individual template-cleaned maps. There is some indication of structure in the CMB signal, particularly in the Q Stokes map at the Galactic anti-center, and in the U map in the region of the North Polar Spur. While this could indicate some Galactic contamination, it is consistent with noise. Outside the P06 mask the maps are morphologically similar to the template-cleaned CMB maps co-added over Ka, Q, and V bands.

To quantify the polarization anisotropy present in the Q and U maps, we use the coordinate-independent scalar and pseudo-scalar E and B modes commonly used in cosmological analysis (Seljak 1997; Kamionkowski et al. 1997; Page et al. 2007). This decomposition provides a useful way of separating the primordial perturbation modes, since scalar, or density, perturbations give rise only to T modes and the curl-free E modes, while tensor perturbations produce T, E and divergence-free B modes. Both polarization modes probe the evolution of the decoupling and reionization epochs and are generated by Thomson scattering of a quadrupolar radiation pattern by free electrons. The anisotropy is quantified using the C_ℓ^{TE}, C_ℓ^{EE}, C_ℓ^{BB} power spectra, where

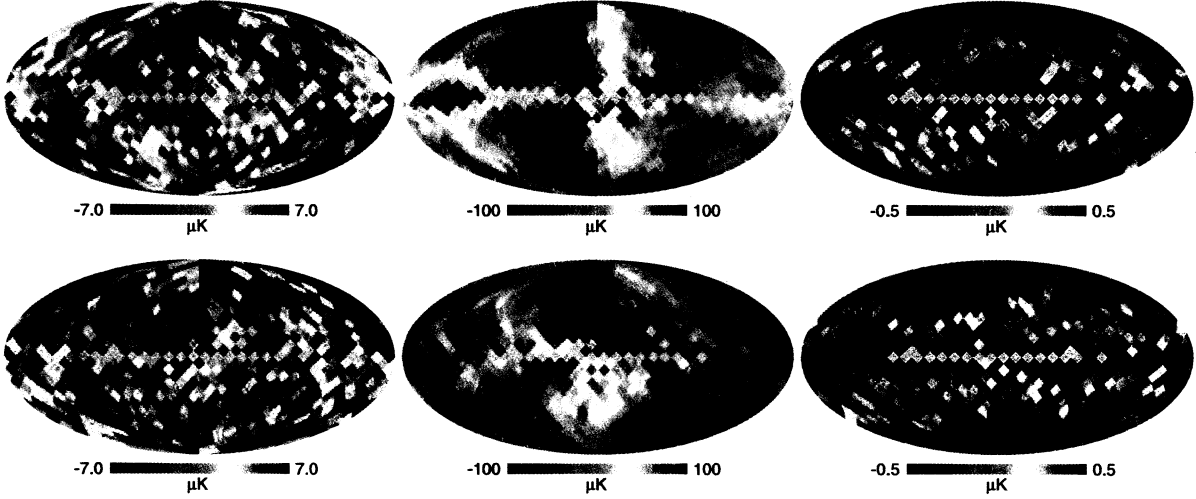$$C_\ell^{XY} = \langle a_{lm}^X a_{lm}^{Y*} \rangle. \tag{7}$$

Fig. 1.— Low resolution polarized Q (top) and U (bottom) maps of the CMB, synchrotron, and dust emission, estimated from the five-year K, Ka, Q, and V band maps using Gibbs sampling. Pixels inside the processing mask are grey. The CMB maps (left panels, thermodynamic temperature) do not show significant Galactic contamination in the plane. The synchrotron amplitudes (center, antenna temperature), are defined at K-band (22.8 GHz), and are consistent with the total K-band maps, with high Q and U emission from the North Polar Spur, and high Q emission in the Galactic plane at longitude $110 \lesssim l \lesssim 170$. The dust amplitudes (right, antenna temperature) are defined at W-band (93.5 GHz), and have a prior that bounds $P = \sqrt{Q^2 + U^2}$ to be less than 20% of the dust intensity in each pixel.

The spin-2 decomposition of the polarization maps, $a_{lm}^{E,B}$, is related to the Q and U maps by

$$[Q \pm iU](\hat{x}) = \sum_{\ell > 1} \sum_{m=-\ell}^{\ell} {}_{\mp 2}a_{\ell m} \, {}_{\mp 2}Y_{\ell m}(\hat{x}) \tag{8}$$

where ${}_{\pm 2}a_{lm} = a_{lm}^E \pm i a_{lm}^B$ (Zaldarriaga & Seljak 1997).

The optical depth to reionization is the parameter that has most effect on the low-ℓ E-mode signal. After decoupling there are no free electrons to scatter the CMB until the first stars reionize the universe at redshift z_r, scattering the intrinsic CMB quadrupole to produce a polarized signal. Its size is $\propto C_2(z_r)^{1/2}\tau(z_r)$, where τ is the optical depth, $\tau(z) = c\sigma_T \int_0^z n_e(z')dz'(dt/dz')$, with σ_T the Thompson cross section, c the speed of light and n_e the free electron density. Reionization therefore has a distinctive signature at $\ell < 10$ in the EE power spectrum, proportional to τ^2.

The measure of τ is one way to compare the Gibbs-cleaned maps produced here, with the template-cleaned maps from the main analysis (Gold et al. 2008). An agreement between the two methods does not guarantee that the inferred signal on the sky is the same using both methods, but is a necessary consistency check. We compute τ using the exact likelihood technique described in Appendix D of Page et al. (2007), with the amplitude of the first temperature acoustic peak fixed, and all other cosmological parameters fixed at best-fit ΛCDM values. The full marginalized covariance matrix is used, including pixel-pixel correlations. We find $\tau = 0.100 \pm 0.017$ for the Gibbs-cleaned maps, which is remarkably consistent with the results obtained through template cleaning, which give $\tau = 0.088 \pm 0.016$ for the KaQV data combination. Obtained using a
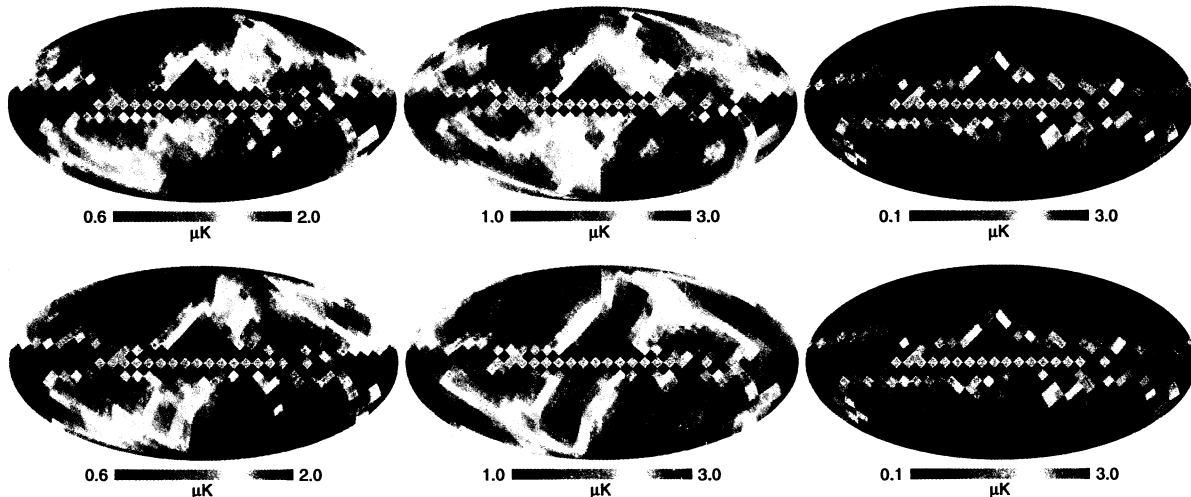
Fig. 2.— Estimated 1σ errors on the low resolution maps of the CMB (left), synchrotron (center), and dust (right) Q and U components, as shown in Figure 1. The CMB errors are more fully described by a covariance matrix, including pixel-pixel correlation and Q/U correlation, so the maps can be used for cosmological analysis. The errors on the dust maps (right) are dominated by the prior that limits the dust polarization fraction to 20%. The middle panels clearly show the two sources of uncertainty in our CMB polarization maps: detector noise in the ecliptic plane (which traces a sideways S in the map) and foreground removal uncertainties in the galactic plane.

different methodology and more fully accounting for foreground marginalization, this adds to our confidence in the detection of the CMB E-mode polarization signal, and to the errors assigned to the optical depth.

We then perform a set of tests where we test the dependence of the estimated optical depth, τ, on the prior assumptions made in the Gibbs-cleaning method, reported in Appendix A. We find that changing the dust spectral index to $\beta_d = 2$ has no effect on the results, nor does changing the location of the 30 regions in the synchrotron spectral index mask, or reducing it to 15 regions. Changing the central value of the prior to -2.8 gives a consistent $\tau = 0.103 \pm 0.018$. Changing the upper limit on the dust polarization fraction to 15% has no effect, but loosening it to 50% and 100% increasingly broadens the distribution and lowers the central value, but the results are consistent. When we include W-band in the analysis we find $\tau = 0.093 \pm 0.016$. However, for cosmological purposes we prefer not to use W band, as the residual power from template-cleaning indicates a potential systematic error (Hinshaw et al. 2008).

We also consider the goodness of fit of the fiducial model to the five-year data. Using this Bayesian method it is not easy to compare the best-fit values to those from template-cleaned maps. The sampling provides a marginalized estimate of the CMB map, with errors, rather than locating a single best-fit point. The maximum-likelihood model has $\chi^2 = 1.03$ per data point, summed over the four bands, $\sum_\nu (\mathbf{d}_\nu - \mathbf{m}_\nu)^T \mathbf{N}_\nu^{-1} (\mathbf{d}_\nu - \mathbf{m}_\nu)$, for the full-sky. We would not expect this model to have $\chi^2 = 1$ per degree of freedom, as thousands of parameters are being drawn simultaneously with the Gibbs algorithm, so the exact χ^2 peak does not get drawn. We compare the fit to simulations, which give a maximum-likelihood model with $\chi^2 = 1.01$ per data point, for simulated data whose properties match the model. The real data therefore provides a comparably good fit.
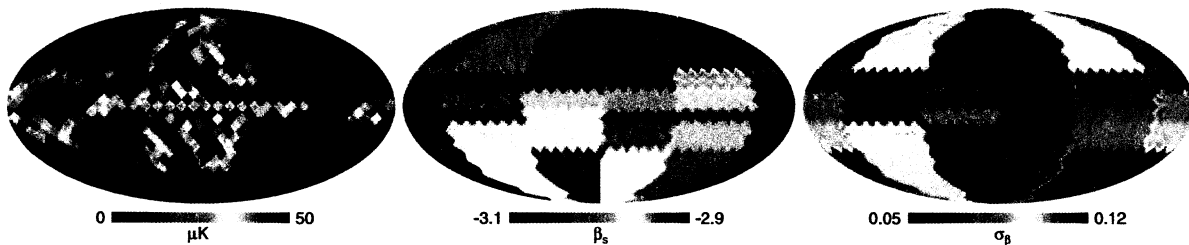
Fig. 3.— Left: The estimated synchrotron polarization amplitude $P = \sqrt{Q^2 + U^2}$ in antenna temperature at K-band, consistent with the total K-band signal in Hinshaw et al. (2008). Right two panels: The estimated synchrotron spectral index (center), and 1σ errors (right), estimated in 30 regions of the sky. A Gaussian prior of $\beta_s = -3.0 \pm 0.15$ is imposed in each region. In regions of low signal-to-noise (near the ecliptic poles), the prior drives the spectral index estimate, but the North Polar Spur and Galactic anti-center prefer a steeper index of ~ -3.1, given the prior.

In the main parameter analysis described later in this paper we use the template-cleaned polarization maps in the main pipeline, as this method has been subjected to more rigorous cross-checks and null tests. However, we check the consistency of ΛCDM parameters using both methods.

2.2.1. Synchrotron and dust polarization

The synchrotron maps shown in Figure 1 are similar to the total K-band maps (Hinshaw et al. 2008), with the total polarized amplitude shown in Figure 3. The difference between the estimated synchrotron amplitude, and the K-band amplitude, is $< 5 \, \mu K$ outside the P06 mask, and $< 8 \, \mu K$ in the Galactic plane. This is not surprising, as the synchrotron emission is expected to dominate at 23 GHz. As observed in the three-year *WMAP* data (Page et al. 2007), the signal is dominated by emission from the North Polar Spur, marked on the microwave sky map in Hinshaw et al. (2007), as well as what is often known as the 'Fan region' (e.g., Wolleben et al. (2006)), centered on Galactic coordinates $l \sim 140$, $b \sim 5$. The synchrotron emission dominates the signal at low frequencies, and so the uncertainty in the synchrotron Q and U maps, shown in Figure 2, is dominated by instrument noise, with only a small additional contribution from component marginalization in the Galactic plane. Figure 3 shows the mean synchrotron spectral index estimated in the 30 regions of the sky, together with 1σ errors. Consistent maps are found for alternative choices of index regions. The prior -3.0 ± 0.15 prevents us from drawing strong conclusions, but there is a preference in the North Polar Spur and Fan region for a steeper index of ~ -3.1. In regions of low synchrotron signal-to-noise the index is driven by the prior. There is no clear trend of the index steepening off the plane, in contrast to what is observed in the synchrotron intensity (Bennett et al. 2003). This is consistent with a recent analysis by Miville-Deschenes et al. (2008), and is the signature of a low polarization component emitting at low frequencies. This component could be an additional non-synchrotron component in the inferred intensity map. It could also be a component whose signal is depolarized, such that the observed polarized signal along a line of sight comes from a physically separate region. Higher signal-to-noise measurements, and lower frequency observations, will help resolve the issue.

The dust polarization map has a low signal-to-noise ratio, particularly far from the plane, as we only fit data in the K-V bands, excluding W band. In these regions the prior dominates the estimate of the

dust amplitude, making it hard to draw conclusions about the dust component. The error in both Q and U is driven by the prior on the polarization ampitudes and so is morphologically identical to the FDS dust intensity map. This explains why the error far from the plane is so low even though the dust can only be poorly measured there. The fractional polarization outside P06 is typically only 1-2%, where we use the degraded FDS dust map to trace intensity, and rises to $\sim$10% in some regions of the plane. This is lower than the $\sim$ 4% estimated in (Kogut et al. 2007; Gold et al. 2008). However, these maps are only estimated for $\nu \leq 61$ GHz, and in regions of low dust the prior will tend to prefer zero polarization. The fractional polarization estimate also assumes that the FDS map accurately traces the dust intensity in the *WMAP* frequency range. Inclusion of higher frequency data will tell us more about the polarized dust, and the analysis including W-band will be presented in a future release.

3. Likelihood and parameter estimation methodology

3.1. Likelihood

The *WMAP* likelihood function takes the same format as for the three-year release, and software implementation is available on LAMBDA (http://lambda.gsfc.nasa.gov) as a standalone package. It takes in theoretical CMB temperature (TT), E-mode polarization (EE), B-mode polarization (BB), and temperature-polarization cross-correlation (TE) power spectra for a given cosmological model. It returns the sum of various likelihood components: low-ℓ temperature, low-ℓ TE/EE/BB polarization, high-ℓ temperature, high-ℓ TE cross-correlation, and additional terms due to uncertainty in the *WMAP* beam determination, and possible error in the extra-galactic point source removal. There is also now an additional option to compute the TB and EB likelihood. The main improvement in the five-year analysis is the implementation of a faster Gibbs sampling method for computing the $\ell \leq 32$ TT likelihood, which we describe in Section 3.1.1.

We continue to evaluate the exact likelihood for the polarization maps at low multipole, $\ell \leq 23$, as described in Appendix D of Page et al. (2007). The input maps and inverse covariance matrix used in the main analysis are produced by co-adding the template-cleaned maps described in Gold et al. (2008). For testing, these are substituted by the Gibbs-cleaned map and inverse covariance matrix described in Section 2 of this paper. In both cases these are weighted to account for the P06 mask using the method described in Page et al. (2007). In the three-year analysis we conservatively used only the Q and V bands in the likelihood. We are now confident that Ka band is cleaned sufficiently for inclusion in analyses (see Hinshaw et al. (2008) for a discussion).

For $\ell > 32$, the TT likelihood uses the combined pseudo-C_ℓ spectrum and covariance matrix described in Hinshaw et al. (2007), estimated using V and W bands. We do not use the EE or BB power spectra at $\ell > 23$, but continue to use the TE likelihood described in Page et al. (2007), estimated using Q and V bands. The errors due to beam and point sources are treated the same as in the three-year analysis, described in Appendix A of Hinshaw et al. (2007). A discussion of this treatment can be found in Nolta et al. (2008).

3.1.1. Low-ℓ temperature likelihood

For a given set of cosmological parameters with theoretical power spectrum C_ℓ, the likelihood function returns $p(\mathbf{d}|C_\ell)$, the likelihood of the observed map $\mathbf{d}$, or its transformed a_{lm} coefficients. Originally, the likelihood code was written as a hybrid combination of a normal and lognormal distribution (Verde et al.

2003). This algorithm did not properly model the tails of the likelihood at low multipoles (Efstathiou 2004; Slosar et al. 2004; O'Dwyer et al. 2004; Hinshaw et al. 2007), and so for the three-year data the $\ell \leq 30$ likelihood was computed exactly, using

$$p(\mathbf{d}|C_\ell) = \frac{\exp[(-(1/2)\mathbf{d}^T\mathbf{C}^{-1}\mathbf{d}]}{\sqrt{\det \mathbf{C}}}, \tag{9}$$

where $\mathbf{C}$ is the covariance matrix of the data including both the signal covariance matrix and noise $\mathbf{C}(C_\ell) = \mathbf{S}(C_\ell) + \mathbf{N}$ (Hinshaw et al. 2007). This approach is computationally intensive however, since it requires the inversion of a large covariance matrix each time the likelihood is called.

In Wandelt et al. (2004) a faster method was developed to compute $p(\mathbf{d}|C_\ell)$, which we now adopt. It is described in detail in that paper, so we only briefly outline the method here. The method uses Gibbs sampling to first sample from the joint posterior distribution $p(C_\ell, \mathbf{s}|\mathbf{d})$, where C_ℓ is the power spectrum and $\mathbf{s}$ is the true sky signal. From these samples, a Blackwell-Rao (BR) estimator provides a continuous approximation to $p(C_\ell|\mathbf{d})$. When a flat prior, $p(C_\ell) = const$, is used in the sampling, we have $p(C_\ell|\mathbf{d}) \propto p(\mathbf{d}|C_\ell)$, where the constant of proportionality is independent of C_ℓ. The BR estimator can then be used as an accurate representation of the likelihood, $p(\mathbf{d}|C_\ell)$ (Wandelt et al. 2004).

The first step requires drawing samples from $p(C_\ell, \mathbf{s}|\mathbf{d})$. We cannot draw samples from the joint distribution directly, but we can from the two conditional distributions $p(\mathbf{s}|C_\ell, \mathbf{d})$ and $p(C_\ell|\mathbf{s}, \mathbf{d})$, each a slice through the $(N_p \times \ell_{\max})$-dimensional space. Samples are drawn alternately, forming a Markov Chain of points by the Gibbs algorithm, as introduced in Section 2:

$$\mathbf{s}^{i+1} \quad \leftarrow \quad p(\mathbf{s}^i|C_\ell^i, \mathbf{d}) \tag{10}$$

$$C_\ell^{i+1} \quad \leftarrow \quad p(C_\ell^i|\mathbf{s}^{i+1}, \mathbf{d}). \tag{11}$$

This samples the full distribution $p(C_\ell, \mathbf{s}|\mathbf{d})$.

The first conditional distribution is a multivariate Gaussian with mean $\mathbf{S}^i(\mathbf{S}^i + \mathbf{N})^{-1}\mathbf{d}$ and variance $[(\mathbf{S}^i)^{-1} + \mathbf{N}^{-1}]^{-1}$, so at each step a new signal vector $\mathbf{s}^{i+1}$, of size N_p, can be drawn. This is computationally demanding however, as described in Wandelt et al. (2004), requiring the solution of a linear system of equations $\mathbf{Mv} = \mathbf{w}$, with $\mathbf{M} = 1 + \mathbf{S}^{1/2}\mathbf{N}^{-1}\mathbf{S}^{1/2}$. These are solved at each step using the conjugate gradient technique, which is sped up by finding an approximate inverse for $\mathbf{M}$, a preconditioner. This requires computation of the inverse noise matrix, $\mathbf{N}^{-1}$ in spherical harmonic space, which is done by computing the components of $\mathbf{N}^{-1}$ term by term using spherical harmonics in pixel space. There are more efficient ways to compute $\mathbf{N}^{-1}$ (Hivon et al. 2002; Eriksen et al. 2004), but computing the preconditioner is a one-time expense, and it is only necessary to compute harmonics up to $\ell = 30$.

The second conditional distribution, $p(C_\ell|\mathbf{s}, \mathbf{d})$ is an inverse Gamma distribution, from which a new C_ℓ vector of size $\ell_{\max}$ can be rapidly drawn using the method in Wandelt et al. (2004). Sampling from these two conditional distributions is continued in turn until convergence, at which point the sample accurately represents the underlying distribution. This is checked in practice using a jacknife test that compares likelihoods from two different samples.

Finally, once the joint distribution $p(C_\ell, \mathbf{s}|\mathbf{d})$ has been pre-computed, the likelihood for any given model C_ℓ is obtained by marginalizing over the signal $\mathbf{s}$, $p(\mathbf{d}|C_\ell) \propto \int p(C_\ell, \mathbf{s}|\mathbf{d})d\mathbf{s}$, which holds for a uniform prior distribution $p(C_\ell)$. In practice this is computed using the Blackwell-Rao estimator,

$$p(\mathbf{d}|C_\ell) \propto \int p(C_\ell|\mathbf{s})p(\mathbf{s}|\mathbf{d})d\mathbf{s} \approx \frac{1}{n_{\mathrm{G}}} \sum_{i=1}^{n_{\mathrm{G}}} p(C_\ell|\mathbf{s}^i) \tag{12}$$
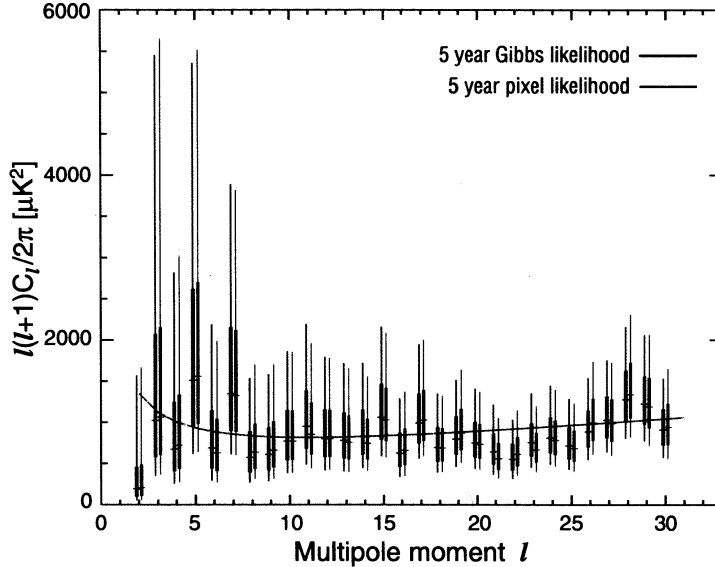
Fig. 4.— This figure compares the low-ℓ TT power spectrum computed with two different techniques. At each ℓ value, we plot the maximum likelihood value (tic mark), the region where the likelihood is greater than 50% of the peak value (thick line) and the region where the likelihood is greater than 95% of the peak value (thin line). The black lines (left side of each pair) are estimated by Gibbs sampling using the ILC map smoothed with a 5 degree Gaussian beam (at HEALPIX $N_{\text{side}} = 32$). The light blue line (right side of the pair) is estimated with a pixel-based likelihood code with $N_{\text{side}} = 16$. The slight differences between the points are primarily due to differences in resolution. At each multipole, the likelihood is sampled by fixing the other C_ℓ values at a fiducial spectrum (red).

where the sum is over all n_G samples in the Gibbs chain. Since $p(C_\ell|\mathbf{s}^i) = p(C_\ell|\sigma_\ell^i)$, where $\sigma_\ell = (2\ell + 1)^{-1} \sum_m |s_{\ell m}|^2$, and $s_{\ell m}$ are the spherical harmonic coefficients of $\mathbf{s}$, one only needs to store σ_ℓ^i at each step in the Gibbs sampling. Then, each time the likelihood is called for a new C_ℓ, one computes $\mathcal{L} = \sum_{i=1}^{n_G} p(C_\ell|\sigma_\ell^i)/n_G$. This requires only $O(\ell_{\max} n_G)$ computations, compared to the full $O(N_p^3)$ evaluation of equation 9. This speed-up also means that the exact likelihood can be used to higher resolution than is feasible with the full evaluation, providing a more accurate estimation.

Code details: Choice of ℓ limits, smoothing, and resolution

The code used for *WMAP* is adapted from the MAGIC Gibbs code described in Wandelt (2003); Wandelt et al. (2004). The input temperature map is the five-year ILC map described in Gold et al. (2008). Because the Blackwell-Rao estimator works poorly in low signal-to-noise regions, we did not attempt to use it for the polarization data. To produce correct results, the Gibbs sampler requires an accurate model of the data. This means that the signal covariance matrix $\mathbf{S}(C_\ell)$ cannot be approximated to be zero except for multipoles where the smoothing make the signal much less than the noise. For the full *WMAP* data set, this would require sampling out to $\ell \sim 1000$, with $N_{\text{side}} = 512$. This is computationally expensive, taking more than of order 10^4 processor-hours to converge (O'Dwyer et al. 2004). Instead we reduce the resolution and smooth the data to substantially reduce the required multipole range, speeding up the computation.

The ILC map is smoothed to 5.0 degree FWHM, and sampled at $N_{\rm side} = 32$. The process of smoothing the data has the side effect of correlating the noise. Correlated noise slows down the Gibbs sampling, as it takes longer to draw a sample from $p(\mathbf{s}|C_\ell, \mathbf{d})$. We therefore add uncorrelated white noise to the map such that it dominates over the smoothed noise. However, the added noise must not be so large that it changes the likelihood of the low-ℓ modes; cosmic variance must remain dominant over the noise (Eriksen et al. 2007), so we add 2 μK of noise per pixel. In Appendix B the noise power spectra are shown.

The Gibbs sampler converges much more slowly in regions of low signal to noise. Because of this, we only sample spectra out to $\ell = 51$ and fix the spectrum for $51 < \ell \le 96$ to a fiducial value, and set it to zero for $\ell > 96$. The BR estimator is only used up to $\ell = 32$ for cosmological analysis, so we marginalize over the $32 < \ell \le 51$ spectrum. The likelihood is therefore $p(L|d) = \int p(L, H|d)dH$, where L and H refer to the low, $\ell \le 32$, and higher, $32 < \ell \le 51$, parts of the power spectrum. Examination of the BR estimator show it to have a smooth distribution. Tests of the results to various input choices, including choice of resolution, are given in Appendix B. We note that by using the low-ℓ likelihood only up to $\ell \le 32$, this breaks the likelihood into a low and high ℓ part, which introduces a small error by ignoring the correlation between these two parts of the spectrum. However, this error is small, and it is unfeasible, in a realistic sampling time, to use the BR estimator over the entire ℓ range probed by *WMAP*.

In Figure 4 we show slices through the C_ℓ distribution obtained from the BR estimator, compared to the pixel likelihood code. The estimated spectra agree well. Some small discrepancies are due to the pixel code using $N_{\rm side} = 16$, compared to the higher resolution $N_{\rm side} = 32$ used for the Gibbs code.

3.2. Parameter Estimation

We use the Markov Chain Monte Carlo methodology described in Spergel et al. (2003, 2007) to explore the probability distributions for various cosmological models, using the five-year *WMAP* data and other cosmological data sets. We map out the full distribution for each cosmological model, for a given data set or data combination, and quote parameter results using the means and 68% confidence limits of the marginalized distributions, with

$$\langle x_i \rangle = \int d^N x L(d|x) p(x) x_i = \frac{1}{M} \sum_{j=1}^{M} x_i^j \tag{13}$$

where x_i^j is the jth value of the ith parameter in the chain. We also give 95% upper or lower limits when the distribution is one-tailed. We have made a number of changes in the five-year analysis, outlined here and in Appendix C.

We parameterize our basic ΛCDM cosmological model in terms of the following parameters:

$$\{\omega_b, \omega_c, \Omega_\Lambda, \tau, n_s, \Delta_{\mathcal{R}}^2\}, \{A_{SZ}\} \tag{14}$$

defined in Table 1. $\Delta_{\mathcal{R}}^2$ is the amplitude of curvature perturbations, and n_s the spectral tilt, both defined at pivot scale $k_0 = 0.002/\text{Mpc}$. In this simplest model we assume instantaneous reionization of the universe, with optical depth τ. The contents of the Universe, assuming a flat geometry, are quantified by the baryon density ω_b, the cold dark matter (CDM) density ω_c and a cosmological constant, Ω_Λ. We treat the contribution to the power spectrum by Sunyaev-Zeldovich fluctuations as in Spergel et al. (2007), adding the predicted template spectrum from Komatsu & Seljak (2002), multiplied by an amplitude A_{SZ}, to the total spectrum. We limit $0 < A_{SZ} < 2$ and impose unbounded uniform priors on the remaining six parameters.

Parameter	Description
ω_b	Baryon density, $\Omega_b h^2$
ω_c	Cold dark matter density, $\Omega_c h^2$
Ω_Λ	Dark energy density, with $w = -1$ unless stated
$\Delta_{\mathcal{R}}^2$	Amplitude of curvature perturbations at $k_0 = 0.002/\text{Mpc}$
n_s	Scalar spectral index at $k_0 = 0.002/\text{Mpc}$
τ	Reionization optical depth
A_{SZ}	SZ marginalization factor
$dn_s/d\ln k$	Running in scalar spectral index
r	Ratio of the amplitude of tensor fluctuations to scalar fluctuations
α_{-1}	Fraction of anti-correlated CDM isocurvature (See Sec 5.1.3)
α_0	Fraction of uncorrelated CDM isocurvature (See Sec 5.1.3)
N_{eff}	Effective number of relativistic species (assumed neutrinos)
ω_ν	Massive neutrino density, $\Omega_\nu h^2$
Ω_k	Spatial curvature, $1 - \Omega_{\text{tot}}$
w	Dark energy equation of state, $w = p_{DE}/\rho_{DE}$
Y_P	Primordial Helium fraction
x_e	Ionization fraction of first step in two-step reionization
z_r	Reionization redshift of first step in two-step reionization
σ_8	Linear theory amplitude of matter fluctuations on $8\ h^{-1}$ Mpc scales
H_0	Hubble expansion factor ($100h\ \text{Mpc}^{-1}\text{km s}^{-1}$)
$\sum m_\nu$	Total neutrino mass (eV) $\sum m_\nu = 94\Omega_\nu h^2$
Ω_m	Matter energy density $\Omega_b + \Omega_c + \Omega_\nu$
$\Omega_m h^2$	Matter energy density
t_0	Age of the universe (billions of years)
z_{reion}	Redshift of instantaneous reionization
η_{10}	Ratio of baryon to photon number densities, $10^{10}(n_b/n_\gamma) = 273.9\ \Omega_b h^2$

Table 1: Cosmological parameters used in the analysis. http://lambda.gsfc.nasa.gov lists the marginalized values for these parameters for all of the models discussed in this paper.

We also consider extensions to this model, parameterized by

$$\{dn_s/d\ln k, r, \alpha_{-1}, \alpha_0, \Omega_K, w, \omega_\nu, N_{\text{eff}}, Y_P, x_e, z_r\} \tag{15}$$

also defined in Table 1. These include cosmologies in which the primordial perturbations have a running scalar spectral index $dn_s/d\ln k$, a tensor contribution with tensor-to-scalar ratio r, or an anti-correlated or uncorrelated isocurvature component, quantified by α_{-1}, α_0. They also include models with a curved geometry Ω_k, a constant dark energy equation of state w, and those with massive neutrinos $\sum m_\nu = 94\Omega_\nu h^2$ eV, varying numbers of relativistic species N_{eff}, and varying primordial Helium fraction Y_P. There are also models with non-instantaneous 'two-step' reionization as in Spergel et al. (2007), with an initial ionized step at z_r with ionized fraction x_e, followed by a second step at $z = 7$ to a fully ionized universe.

These parameters all take uniform priors, and are all sampled directly, but we bound $N_{\text{eff}} < 10$, $w > -2.5$, $z_r < 30$ and impose positivity priors on r, α_{-1}, α_0, ω_ν, Y_p, and Ω_Λ, as well as requiring $0 < x_e < 1$. The tensor spectral index is fixed at $n_t = -r/8$. We place a prior on the Hubble constant of $20 < H_0 < 100$, but this only affects non-flat models. Other parameters, including σ_8, the redshift of reionization, z_{reion}, and the age of the universe, t_0, are derived from these primary parameters and described in Table 1. A more extensive set of derived parameters are provided on the LAMBDA website.
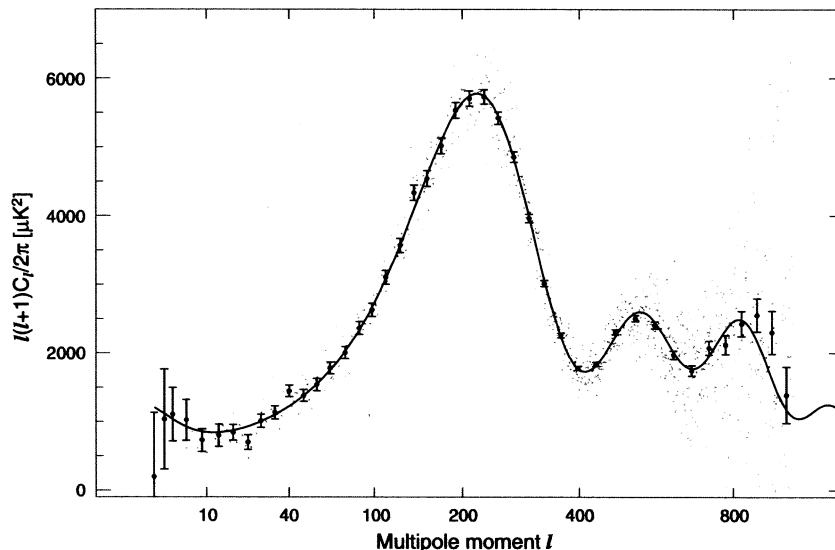
Fig. 5.— The temperature angular power spectrum corresponding to the *WMAP*-only best-fit ΛCDM model. The grey dots are the unbinned data; the black data points are binned data with 1σ error bars including both noise and cosmic variance computed for the best-fit model.

We continue to use the CAMB code (Lewis et al. 2000) to generate the CMB power spectra for a given set of cosmological parameters. Given the improvement in the *WMAP* data, we have determined that distortions to the spectra due to weak gravitational lensing should now be included. We use the lensing option in CAMB which roughly doubles the time taken to generate a model, compared to the unlensed case.

We have made a number of changes in the parameter sampling methodology. Our main pipeline now uses an MCMC code originally developed for use in Bucher et al. (2004), which has been adapted for *WMAP*. For increased speed and reliability, it incorporates two changes in the methodology described in Spergel et al. (2007). It uses a modified sampling method that generates a single chain for each model (instead of the four, or eight, commonly used in cosmological analyses). We also use an alternative spectral convergence test that can be run on a single chain, developed in Dunkley et al. (2005), instead of the Gelman & Rubin test used in Spergel et al. (2007). These are both described in Appendix C. We also use the publicly available CosmoMC sampling code (Lewis & Bridle 2002) as a secondary pipeline, used as an independent cross-check for a limited set of models.

4. The ΛCDM Cosmological Model

4.1. *WMAP* five-year parameters

The ΛCDM model, described by just six parameters, is still an excellent fit to the *WMAP* data. The temperature and polarization angular power spectra are shown in Nolta et al. (2008). With more observation the errors on the third acoustic peak in the temperature angular power spectrum have been reduced. The TE cross-correlation spectrum has also improved, with a better measurement of the second anti-correlation at $\ell \sim 500$. The low-ℓ signal in the EE spectrum, due to reionization of the universe, is now measured with

Parameter	3 Year Mean	5 Year Mean	5 Year Max Like
$100\Omega_b h^2$	2.229 ± 0.073	2.273 ± 0.062	2.27
$\Omega_c h^2$	0.1054 ± 0.0078	0.1099 ± 0.0062	0.108
Ω_Λ	0.759 ± 0.034	0.742 ± 0.030	0.751
n_s	0.958 ± 0.016	$0.963^{+0.014}_{-0.015}$	0.961
τ	0.089 ± 0.030	0.087 ± 0.017	0.089
$\Delta_\mathcal{R}^2$	$(2.35 \pm 0.13) \times 10^{-9}$	$(2.41 \pm 0.11) \times 10^{-9}$	2.41×10^{-9}
σ_8	0.761 ± 0.049	0.796 ± 0.036	0.787
Ω_m	0.241 ± 0.034	0.258 ± 0.030	0.249
$\Omega_m h^2$	0.128 ± 0.008	0.1326 ± 0.0063	0.131
H_0	$73.2^{+3.1}_{-3.2}$	$71.9^{+2.6}_{-2.7}$	72.4
$z_{\rm reion}$	11.0 ± 2.6	11.0 ± 1.4	11.2
t_0	13.73 ± 0.16	13.69 ± 0.13	13.7

Table 2: ΛCDM model parameters and 68% confidence intervals from the five-year *WMAP* data alone. The three-year values are shown for comparison. For best estimates of parameters, the marginalized 'Mean' values should be used. The 'Max Like' values correspond to the single model giving the highest likelihood.

higher significance (Nolta et al. 2008). The best-fit 6 parameter model, shown in Figure 5, is successful in fitting three TT acoustic peaks, three TE cross-correlation maxima/minima, and the low-ℓ EE signal. The model is compared to the polarization data in Nolta et al. (2008). The consistency of both the temperature and polarization signals with ΛCDM continues to validate the model.

The five-year marginalized distributions for ΛCDM, shown in Table 2 and Figures 6 and 7, are consistent with the three-year results (Spergel et al. 2007), but the uncertainties are all reduced, significantly so for certain parameters. With longer integration of the large-scale polarization anisotropy, there has been a significant improvement in the measurement of the optical depth to reionization. There is now a 5σ detection of τ, with mean value $\tau = 0.087 \pm 0.017$. This can be compared to the three-year measure of $\tau = 0.089 \pm 0.03$. The central value is little altered with two more years of integration, and the inclusion of the Ka band data, but the limits have almost halved. This measurement, and its implications, are discussed in Sec 4.1.1.

The higher acoustic peaks in the TT and TE power spectra also provide more information about the ΛCDM model. Longer integration has resulted in a better measure of the height and position of the third peak. The highest multipoles have a slightly higher mean value relative to the first peak, compared to the three-year data. This can be attributed partly to improved beam modeling, and partly to longer integration time reducing the noise. The third peak position constrains $\Omega_m^{0.275}h$ (Page et al. 2003), while the third peak height strongly constrains the matter density, $\Omega_m h^2$. In this region of the spectrum, the WMAP data are noise-dominated so that the errors on the angular power spectrum shrink as $1/t$. The uncertainty on the matter density has dropped from 12% in the first year data to 8% in the three year data and now 6% in the five year data. The CDM density constraints are compared to three-year limits in Figure 6. The spectral index still has a mean value 2.5σ less than unity, with $n_s = 0.963^{+0.014}_{-0.015}$. This continues to indicate the preference of a red spectrum consistent with the simplest inflationary scenarios (Linde 2005; Boyle et al. 2006), and our confidence will be enhanced with more integration time.

Both the large scale EE spectrum and the small scale TT spectrum contribute to an improved measure of the amplitude of matter fluctuations. With the CMB we measure the amplitude of curvature fluctuations,
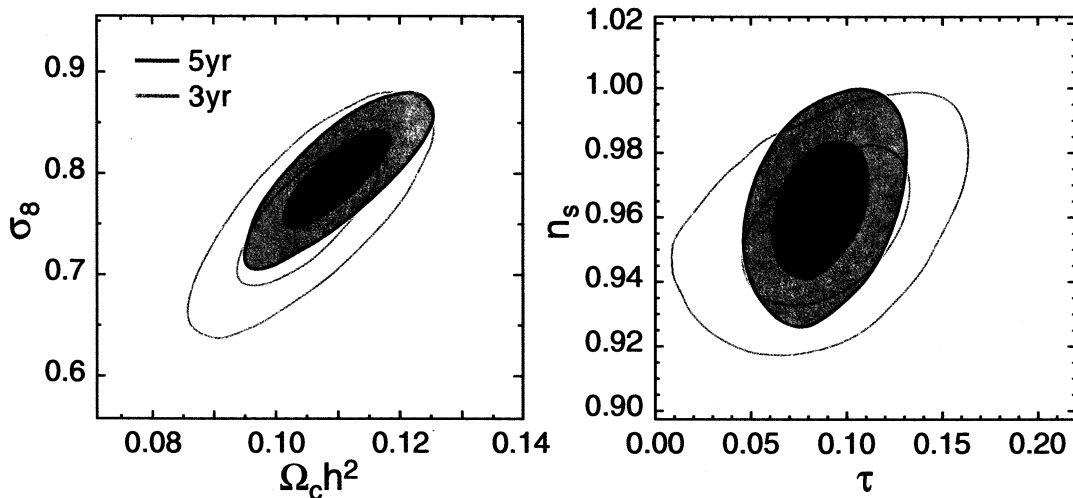
Fig. 6.— Constraints on ΛCDM parameters from the five-year *WMAP* data. The two-dimensional 68% and 95% marginalized limits are shown in blue. They are consistent with the three-year constraints (grey). Tighter limits on the amplitude of matter fluctuations, σ_8, and the cold dark matter density $\Omega_c h^2$, arise from a better measurement of the third temperature (TT) acoustic peak. The improved measurement of the EE spectrum provides a 5σ detection of the optical depth to reionization, τ, which is now almost uncorrelated with the spectral index n_s.

quantified by $\Delta_{\mathcal{R}}^2$, but we also derive limits on σ_8, the amplitude of matter fluctuations on $8h^{-1}$Mpc scales. A higher value for τ produces more overall damping of the CMB temperature signal, making it somewhat degenerate with the amplitude, $\Delta_{\mathcal{R}}^2$, and therefore σ_8. The value of σ_8 also affects the height of the acoustic peaks at small scales, so information is gained from both temperature and polarization. The five-year data give $\sigma_8 = 0.796 \pm 0.036$, slightly higher than the three-year result, driven by the increase in the amplitude of the power spectrum near the third peak. The value is now remarkably consistent with new measurements from weak lensing surveys, as discussed in Section 4.2.

4.1.1. Reionization

Our observations of the acoustic peaks in the TT and TE spectrum imply that most of the ions and electrons in the universe combined to make neutral hydrogen and helium at $z \simeq 1100$. Observations of quasar spectra show no Gunn-Peterson trough at $z > 5.8$ (Fan et al. 2000, 2001) implying that the universe was nearly fully ionized by $z = 5.7$. How did the universe make the transition from being nearly fully neutral to fully ionized? The astrophysics of reionization has been a very active area of research in the past decade. Several recent reviews (Barkana & Loeb 2006; Fan et al. 2006; Furlanetto et al. 2006; Meiksin 2007) summarize the current observations and theoretical models. Here, we highlight a few of the important issues and discuss some of the implications of the *WMAP* measurements of optical depth.
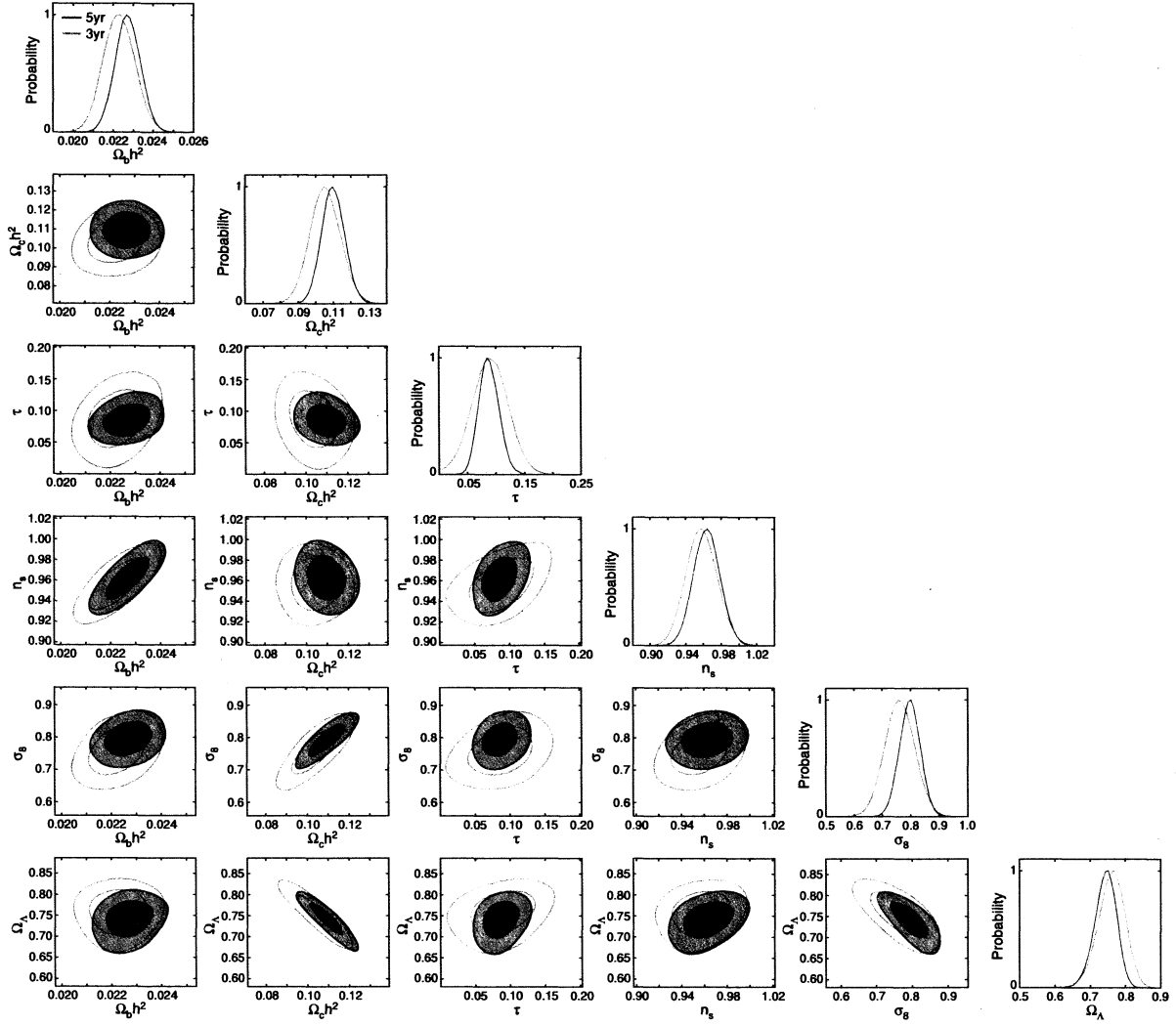
Fig. 7.— Constraints from the five-year *WMAP* data on ΛCDM parameters (blue), showing marginalized one-dimensional distributions and two-dimensional 68% and 95% limits. Parameters are consistent with the three-year limits (grey) from Spergel et al. (2007), and are now better constrained.
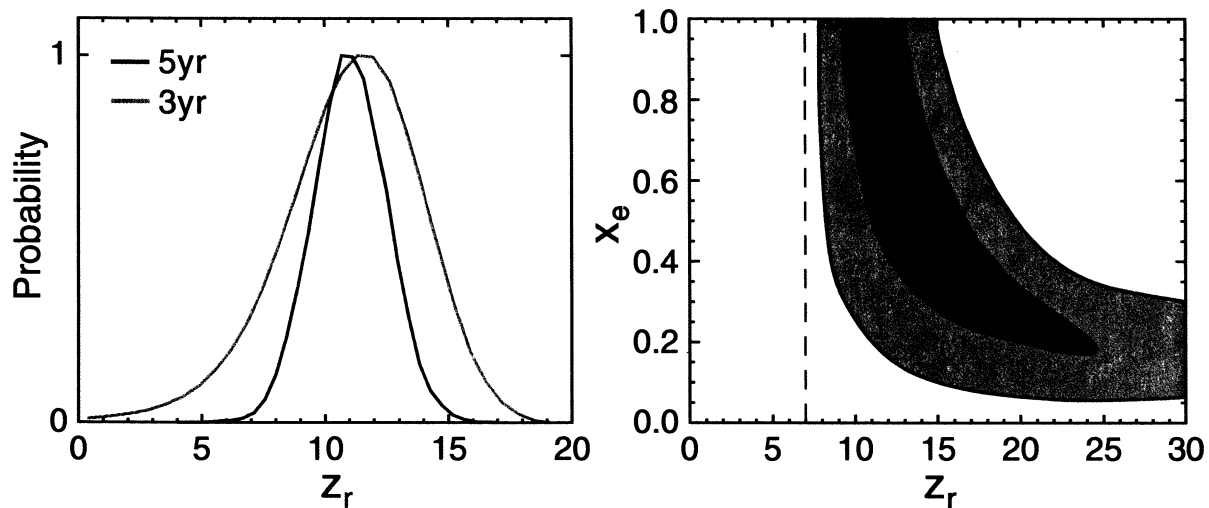
Fig. 8.— Left: Marginalized probability distribution for z_{reion} in the standard model with instantaneous reionization. Sudden reionization at $z = 6$ is ruled out at 3.5σ, suggesting that reionization was a gradual process. Right: In a model with two steps of reionization (with ionization fraction x_e at redshift z_r, followed by full ionization at $z = 7$), the *WMAP* data are consistent with an extended reionization process.

What objects reionized the universe? While high redshift galaxies are usually considered the most likely source of reionization, AGNs may also have played an important role. As galaxy surveys push towards ever higher redshift, it is unclear whether the known population of star forming galaxies at $z \sim 6$ could have ionized the universe (see e.g., Bunker et al. (2007)). The EE signal clearly seen in the *WMAP* five-year data (Nolta et al. (2008); §2) implies an optical depth, $\tau \simeq 0.09$. This large optical depth suggests that higher redshift galaxies, perhaps the low luminosity sources appearing in $z > 7$ surveys (Stark et al. 2007), played an important role in reionization. While the known population of AGNs can not be a significant source of reionization (Bolton & Haehnelt 2007; Srbinovsky & Wyithe 2007), an early generation of supermassive black holes could have played a role in reionization (Ricotti & Ostriker 2004; Ricotti et al. 2007). This early reionization would also have an impact on the CMB.

Most of our observational constraints probe the end of the epoch of reionization. Observations of $z > 6$ quasars (Becker 2001; Djorgovski et al. 2001; Fan et al. 2006; Willott et al. 2007) find that the Lyman-α optical depth rises rapidly. Measurements of the afterglow spectrum of a gamma ray burst at $z = 6.3$ (Totani et al. 2006) suggest that universe was mostly ionized at $z = 6.3$. Lyman alpha emitter surveys (Taniguchi et al. 2005; Malhotra & Rhoads 2006; Kashikawa et al. 2006; Iye et al. 2006; Ota et al. 2007) imply a significant ionized fraction at $z = 6.5$. The interpretation that there is a sudden change in the properties of the IGM remains a subject of active debate (Becker et al. 2007; Wyithe et al. 2008).

The *WMAP* data place new constraints on the reionization history of the universe. The *WMAP* data best constrains the optical depth due to reionization at moderate redshift ($z < 25$) and only indirectly constrains the redshift of reionization. If reionization is sudden, then the *WMAP* data implies that $z_{\mathrm{reion}} = 11.0 \pm 1.4$, shown in Figure 8, and now excludes $z_{\mathrm{reion}} = 6$ at more than 99.9% CL. The combination of the *WMAP* data implying that the universe was mostly reionized at $z \sim 11$ and the measurements of rapidly rising optical depth at $z \sim 6 - 6.5$ suggest that reionization was an extended process rather than a sudden transition. Many
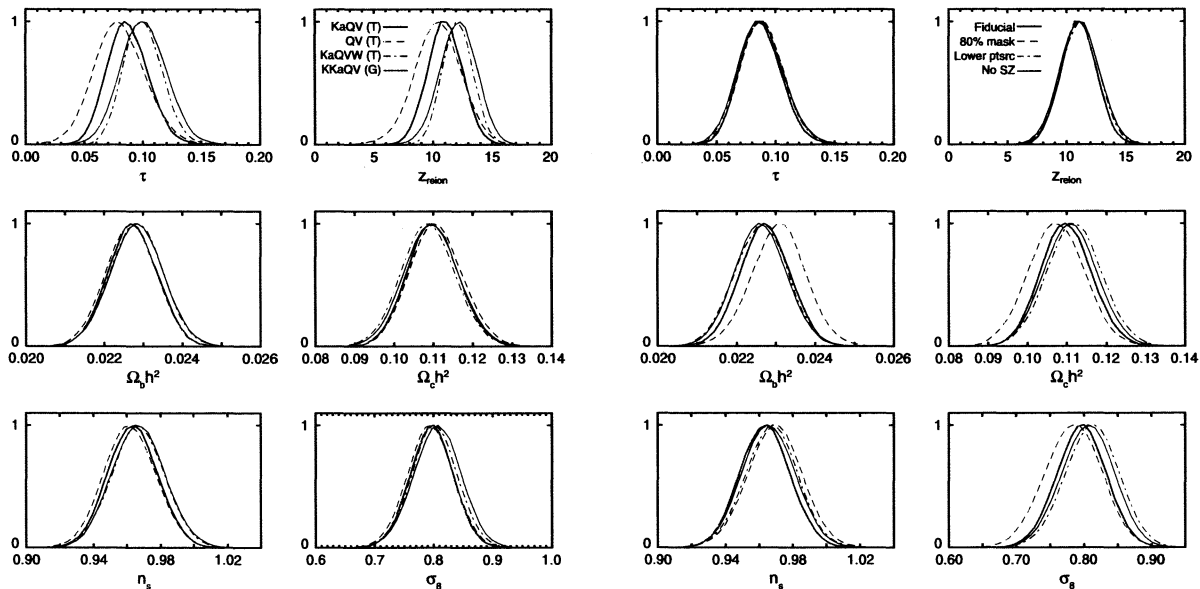
Fig. 9.— Effect of foreground treatment and likelihood details on ΛCDM parameters. Left: The number of bands used in the template cleaning (denoted 'T'), affects the precision to which τ is determined, with the standard KaQV compared to QV and KaQVW, but has little effect on other cosmological parameters. Using maps cleaned by Gibbs sampling (KKaQV (G)) also gives consistent results. Right: Lowering the residual point source contribution ('lower ptsrc') and removing the marginalization over an SZ contribution ('No SZ') affects parameters by $< 0.4\sigma$. Using a larger mask ('80% mask') has a greater effect, increasing $\Omega_b h^2$ by 0.5σ, but is consistent with the effects of noise.

early studies of reionization envisioned a rapid transition from a neutral to a fully ionized universe occurring as ionized bubbles percolate and overlap. As Figure 8 shows, the *WMAP* data suggests a more gradual process with reionization beginning perhaps as early as $z \sim 20$ and strongly favoring $z > 6$. *This suggests that the universe underwent an extended period of partial reionization.* The limits were found by modifying the ionization history in CAMB to include two steps in the ionization fraction at late times ($z < 30$): the first at z_r with ionization fraction x_e, the second at $z = 7$ with $x_e = 1$. Several studies (Cen 2003; Chiu et al. 2003; Wyithe & Loeb 2003; Haiman & Holder 2003; Yoshida et al. 2004; Choudhury & Ferrara 2006; Iliev et al. 2007; Wyithe et al. 2008) suggest that feedback produces a prolonged or perhaps even, multi-epoch reionization history.

While the current *WMAP* data constrain the optical depth of the universe, the EE data does not yet provide a detailed constraint on the reionization history. With more data from *WMAP* and upcoming data from Planck, the EE spectrum will begin to place stronger constraints on the details of reionization (Kaplinghat et al. 2003; Holder et al. 2003; Mortonson & Hu 2008). These measurements will be supplemented by measurements of the Ostriker-Vishniac effect by high resolution CMB experiments which is sensitive to $\int n_e^2 dt$ (Jaffe & Kamionkowski 1998).

4.1.2. Sensitivity to foreground cleaning

As the E-mode signal is probed with higher accuracy, it becomes increasingly important to test how much the constraint on τ, $z_{\rm reion}$, and the other cosmological parameters, depend on details of the Galactic foreground removal. Tests were done in Page et al. (2007) to show that τ was insensitive to a set of variations in the dust template used to clean the maps. In Figure 9 we show the effect on ΛCDM parameters of changing the number of bands used in the template-cleaning method: discarding Ka band in the 'QV' combination, or adding W band in the 'KaQVW' combination. We find that τ (and therefore $z_{\rm reion}$) is sensitive to the maps, but the dispersion is consistent with noise. As expected, the error bars are broadened for the QV combined data, and the mean value is $\tau = 0.080 \pm 0.020$. When W band is included, the mean value is $\tau = 0.100 \pm 0.015$. We choose not to use the W band map in our main analysis however, as noted in Section 2.1, because there appears to be excess power in the cleaned map at $\ell = 7$. This indicates a potential systematic error, and is discussed further in Hinshaw et al. (2008). The other cosmological parameters are only mildly sensitive to the number of bands used. This highlights the fact that τ is no longer as strongly correlated with other parameters, as in earlier WMAP data (Spergel et al. 2003, 2007), notably with the spectral index of primordial fluctuations, n_s (Figure 6).

We also test the parameters obtained using the Gibbs-cleaned maps described in Section 2, which use the K, Ka, Q, and V band maps. Their distributions are also shown in Figure 9, and have mean $\tau = 0.100 \pm 0.018$. This is less than 1σ higher than the KaQV template-cleaned maps but uses a independent method. The other cosmological parameters are changed by less than 0.3σ compared to the template-cleaned results. This consistency gives us confidence that the parameter constraints are little affected by foreground uncertainty.

4.1.3. Sensitivity to likelihood details

The likelihood code used for cosmological analysis has a number of variable components that have been fixed using our best estimates. Here we consider the effect of these choices on the five-year ΛCDM parameters. The first two are the treatment of the residual point sources, and the treatment of the beam error, both discussed in Nolta et al. (2008). The multi-frequency data are used to estimate a residual point source amplitude of $A_{ps} = 0.011 \pm 0.001 \, \mu K^2 {\rm sr}$, which scales the expected contribution to the cross-power spectra of sources below our detection threshold. It is defined in Hinshaw et al. (2007); Nolta et al. (2008), and is marginalized over in the likelihood code. The estimate comes from QVW data, whereas the VW data give $0.007 \pm 0.003 \, \mu K^2 {\rm sr}$, both using the KQ85 mask described in Hinshaw et al. (2008). The right panels in Figure 9 shows the effect on a subset of parameters of lowering A_{ps} to the VW value, which leads to a slightly higher n_s, $\Omega_c h^2$ and σ_8, all within 0.4σ of the fiducial values, and consistent with more of the observed high-ℓ signal being due to CMB rather than unresolved point sources. We also use $A_{ps} = 0.011 \, \mu K^2 {\rm sr}$ with no point source error, and find a negligible effect on parameters ($< 0.1\sigma$). The beam window function error is quantified by ten modes, and in the standard treatment we marginalize over them, following the prescription in Hinshaw et al. (2007). We find that removing the beam error also has a negligible effect on parameters. This is discussed further in Nolta et al. (2008), who considers alternative treatments of the beam and point source errors.

The next issue is the treatment of a possible contribution from Sunyaev Zeldovich fluctuations. We account for the SZ effect in the same way as in the three-year analysis, marginalizing over the amplitude of the contribution parameterized by the Komatsu-Seljak model (Komatsu & Seljak 2002). The parameter A_{SZ} is unconstrained by the WMAP data, but is not strongly degenerate with any other parameters. In

Figure 9 we show the effect on parameters of setting the SZ contribution to zero. Similar to the effect of changing the point source contribution, the parameters depending on the third peak are slightly affected, with a $< 0.25\sigma$ increase in n_s, $\Omega_c h^2$, σ_8 and similar decrease in baryon density.

Another choice is the area of sky used for cosmological interpretation, or how much we mask out to account for Galactic contamination. Gold et al. (2008) discuss the new masks used for the five-year analysis, with the KQ85 mask used as standard. We test the effect of using the more conservative KQ80 mask, and find a more noticeable shift. The quantity $\Omega_b h^2$ is increased by 0.5σ, and n_s, $\Omega_c h^2$ and σ_8 all decreased by $\sim 0.4\sigma$. This raised concerns that the KQ85 mask contains residual foreground contamination, but as discussed in Nolta et al. (2008), this shift is found to be consistent with the effects of noise, tested with simulations. We also confirm that the effect on parameters is even less for ΛCDM models using *WMAP* with external data, and that the choice of mask has only a small effect on the tensor amplitude, raising the 95% confidence level by $\sim$5%.

Finally, we test the effect on parameters of varying aspects of the low-ℓ TT treatment. These are discussed in Appendix B, and in summary we find the same parameter results for the pixel-based likelihood code compared to the Gibbs code, when both use $\ell \leq 32$. Changing the mask at low-ℓ to KQ80, or using the Gibbs code up to $\ell \leq 51$, instead of $\ell \leq 32$, has a negligible effect on parameters.

4.2. Consistency of the ΛCDM model with other data sets

While the *WMAP* data alone place strong constraints on cosmological parameters, there has been a wealth of results from other cosmological observations in the last few years. These observations can generally be used either to show consistency of the simple ΛCDM model parameters, or to constrain more complicated models. In this section we describe various current astronomical data sets that provide cosmological information. A subset of the data is used to place combined constraints on extended cosmological models in Komatsu et al. (2008). Here we compare a much broader set of data to the *WMAP* ΛCDM model.

4.2.1. Small-scale CMB measurements

A number of recent CMB experiments have probed smaller angular scales than *WMAP* can reach and are therefore more sensitive to the higher order acoustic oscillations and the details of recombination. Since the three-year *WMAP* analysis, there have been new temperature results from the Arcminute Cosmology Bolometer Array Receiver (ACBAR), both in 2007 (Kuo et al. 2007) and in 2008 (Reichardt et al. 2008). They have measured the angular power spectrum at 145 GHz to 5' resolution, over $\sim$600 deg^2. Their results are consistent with the model predicted by the *WMAP* five-year data, shown in Figure 10, although ACBAR is calibrated using *WMAP*, so the data are not completely independent.

Figure 10 also shows data from the BOOMERANG, CBI and VSA experiments, which agree well with *WMAP*. There have also been new observations of the CMB polarization from two ground-based experiments, QUaD, operating at 100 GHz and 150 GHz (P. Ade et al. 2007), and CAPMAP, at 40 GHz and 100 GHz (Bischoff et al. 2008). Their measurements of the EE power spectrum are shown in Nolta et al. (2008), together with detections already made since 2005 (Leitch et al. 2005; Sievers et al. 2007; Barkats et al. 2005; Montroy et al. 2006), and are all consistent with the ΛCDM model parameters.

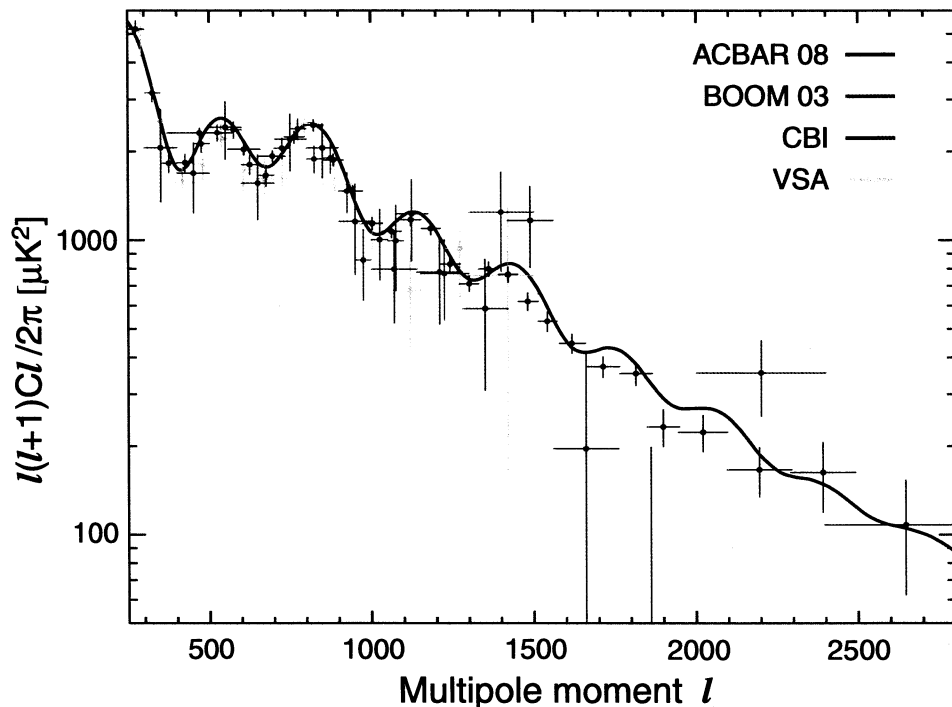In our combined analysis in Komatsu et al. (2008) we use two different data combinations. For the first

Fig. 10.— The best-fit temperature angular power spectrum from *WMAP* alone (red), is consistent with data from recent small-scale CMB experiments: ACBAR, CBI, VSA and BOOMERANG.

we combine four data sets. This includes the 2007 ACBAR data (Kuo et al. 2007), using 10 bandpowers in the range $900 < \ell < 2000$. The values and errors were obtained from the ACBAR web site. We also include the three external CMB data sets used in Spergel et al. (2003): the Cosmic Background Imager (CBI; Mason et al. (2003); Sievers et al. (2003); Pearson et al. (2003); Readhead et al. (2004)), the Very Small Array (VSA; Dickinson et al. (2004)) and BOOMERANG (Ruhl et al. 2003; Montroy et al. 2006; Piacentini et al. 2006). As in the three-year release we only use bandpowers that do not overlap with the signal-dominated *WMAP* data, due to non-trivial cross-correlations, so we use seven bandpowers for CBI (in the range $948 < \ell < 1739$), five for VSA ($894 < \ell < 1407$) and seven for BOOMERANG ($924 < \ell < 1370$), using the lognormal form of the likelihood. Constraints are also found by combining *WMAP* with the 2008 ACBAR data, using 16 bandpowers in the range $900 < \ell < 2000$. In this case the other CMB experiments are not included. We do not use additional polarization results for parameter constraints as they do not yet improve limits beyond *WMAP* alone.

4.2.2. Baryon Acoustic Oscillations

The acoustic peak in the galaxy correlation function is a prediction of the adiabatic cosmological model. It was first detected using the SDSS luminous red galaxy (LRG) survey, using the brightest class of galaxies at mean redshift $z = 0.35$ by Eisenstein et al. (2005). The peak was detected at $100 h^{-1}$Mpc separation, providing a standard ruler to measure the ratio of distances to $z = 0.35$ and the CMB at $z = 1089$,

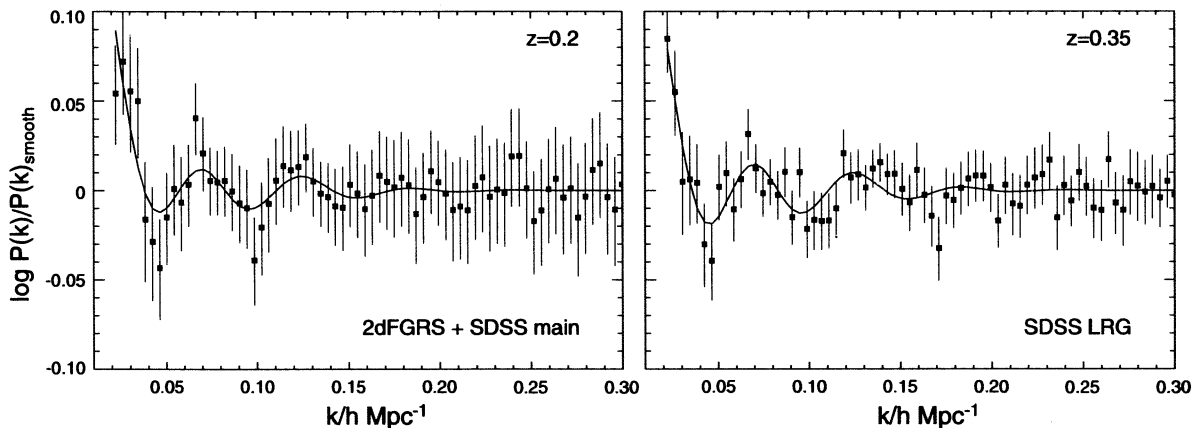Fig. 11.— Baryon Acoustic Oscillations expected for the best-fit ΛCDM model (red lines), compared to BAO in galaxy power spectra calculated from (left) combined SDSS and 2dFGRS main galaxies, and (right) SDSS LRG galaxies, by Percival et al. (2007a). The observed and model power spectra have been divided by $P(k)_{\mathrm{smooth}}$, a smooth cubic spline fit described in Percival et al. (2007a).

and the absolute distance to $z = 0.35$. More recently Percival et al. (2007b) have obtained a stronger detection from over half a million SDSS main galaxies and LRGs in the DR5 sample. They detect baryon acoustic oscillations (BAO) with over 99% confidence. A combined analysis was then undertaken of SDSS and 2dFGRS by Percival et al. (2007a). They find evidence for BAO in three catalogs: at mean redshift $z = 0.2$ in the SDSS DR5 main galaxies plus the 2dFGRS galaxies, at $z = 0.35$ in the SDSS LRGs, and in the combined catalog. Their data are shown in Figure 11, together with the *WMAP* best-fit model. The BAO are shown by dividing the observed and model power spectra by $P(k)_{\mathrm{smooth}}$, a smooth cubic spline fit described in Percival et al. (2007a). The observed power spectra are model-dependent, but were calculated using $\Omega_m = 0.25$ and $h = 0.72$, which agrees with our maximum-likelihood model.

The scale of the BAO is analyzed to estimate the geometrical distance measure at $z = 0.2$ and $z = 0.35$,

$$D_V(z) = [(1+z)^2 D_A^2 cz / H(z)]^{1/3}, \tag{16}$$

where D_A is the angular diameter distance and $H(z)$ the Hubble parameter. They find $r_s/D_V(0.2) = 0.1980 \pm 0.0058$ and $r_s/D_V(0.35) = 0.1094 \pm 0.0033$. Here r_s is the comoving sound horizon scale at recombination. Our ΛCDM model, using the *WMAP* data alone, gives $r_s/D_V(0.2) = 0.1946 \pm 0.0079$ and $r_s/D_V(0.35) = 0.1165 \pm 0.0042$, showing the consistency between the CMB measurement at $z = 1089$ and the late-time galaxy clustering. However, while the $z = 0.2$ measures agree to within 1σ, the $z = 0.35$ measurements have mean values almost 2σ apart. The BAO constraints are tighter then the *WMAP* predictions, which shows that they can improve upon the *WMAP* parameter determinations, in particular on Ω_Λ and $\Omega_m h^2$.

We use the combined bounds from both surveys to constrain models as described in Percival et al. (2007a), adding a likelihood term given by $-2 \ln L = X^T C^{-1} X$, with

$$X^T = [r_s/D_V(0.2) - 0.1980, r_s/D_V(0.35) - 0.1094] \tag{17}$$

and $C^{11} = 35059$, $C^{12} = -24031$, $C^{22} = 108300$, including the correlation between the two measurements. We also consider constraints using the SDSS LRG limits derived by Eisenstein et al. (2005), using the

combination

$$A(z) = D_V(z)\sqrt{\Omega_m H_0^2}/cz \tag{18}$$

for $z = 0.35$ and computing a Gaussian likelihood $-2\ln L = (A - 0.469(n_s/0.98)^{-0.35})^2/0.017^2$. See Komatsu et al. (2008) for further discussion of the BAO data.

4.2.3. Galaxy power spectra

We can compare the predicted fluctuations from the CMB to the shape of galaxy power spectra, in addition to the scale of acoustic oscillations. The SDSS galaxy power spectum from DR3 (Tegmark et al. 2004) and the 2dFGRS spectrum (Cole et al. 2005) were shown to be in good agreement with the *WMAP* three-year data, and used to place tighter constraints on cosmological models (Spergel et al. 2007), but there was some tension between the preferred values of the matter density ($\Omega_m = 0.236 \pm 0.020$ with 2dFGRS and 0.265 ± 0.030 with SDSS).

More recently two studies used photometric redshifts to estimate the galaxy power spectrum from the photometric-redshift catalogue of LRGs from the SDSS fourth data release (DR4, Padmanabhan et al. (2007); Blake et al. (2007)). Padmanabhan et al. (2007) compute the 3D real-space clustering power spectrum of the SDSS LRGs, probing galaxies in redshift range $0.2 < z < 0.6$. Their estimates of $\Omega_m = 0.30 \pm 0.03$, and $\Omega_b/\Omega_m = 0.18 \pm 0.04$, for a fixed Hubble constant of $h = 70$, are consistent with our data, and with the Blake et al. (2007) analysis which finds $\Omega_m h = 0.195 \pm 0.023$ and $\Omega_b/\Omega_m = 0.16 \pm 0.036$, for $h = 0.75$.

More precise measurements of the LRG power spectrum were then obtained from redshift measurements: Tegmark et al. (2006) used LRGs from SDSS DR4 in the range $0.01h/\mathrm{Mpc} < k < 0.2h/\mathrm{Mpc}$ combined with the three-year *WMAP* data to place strong constraints on cosmological models. However, there is a disagreement between the matter density predicted using different minimum scales, if the non-linear modeling used in Tegmark et al. (2006) is adopted. Using the three-year *WMAP* data combined with the LRG spectrum we find $\Omega_m = 0.228 \pm 0.019$, using scales with $k < 0.1h$ Mpc^{-1}, and $\Omega_m = 0.248 \pm 0.018$ for $k < 0.2h$ Mpc^{-1}. These constraints are obtained for the 6 parameter ΛCDM model, following the non-linear prescription in Tegmark et al. (2006). This agrees with results obtained from the DR5 main galaxy and LRG sample (Percival et al. 2007c), who argue that this shows evidence for scale-dependent bias on large-scales, which could explain the observed differences in the early SDSS and 2dFGRS results. While the *WMAP* five year ΛCDM model, with $\Omega_m = 0.258 \pm 0.030$, is not inconsistent with the measured spectra, we choose not to use the galaxy power spectra to place joint constraints on the majority of models in Komatsu et al. (2008). For ΛCDM we test joint constraints using the SDSS DR3 and 2dFGRS data separately, using the method described in Spergel et al. (2007), and using the SDSS DR4 LRG spectrum following the method in Tegmark et al. (2006).

4.2.4. Type Ia Supernovae

In the last decade Type Ia supernovae have become an important cosmological probe, and have provided the first direct evidence for the acceleration of the universe by measuring the luminosity distance as a function of redshift. The observed dimness of high redshift supernovae ($z \sim 0.5$) was first measured by Riess et al. (1998); Schmidt et al. (1998); Perlmutter et al. (1999), confirmed with more recent measurements including Nobili et al. (2005); Krisciunas et al. (2005); Clocchiatti et al. (2006); Astier et al. (2006), and extended to higher redshift by Riess et al. (2004) who found evidence for the earlier deceleration of the universe. The
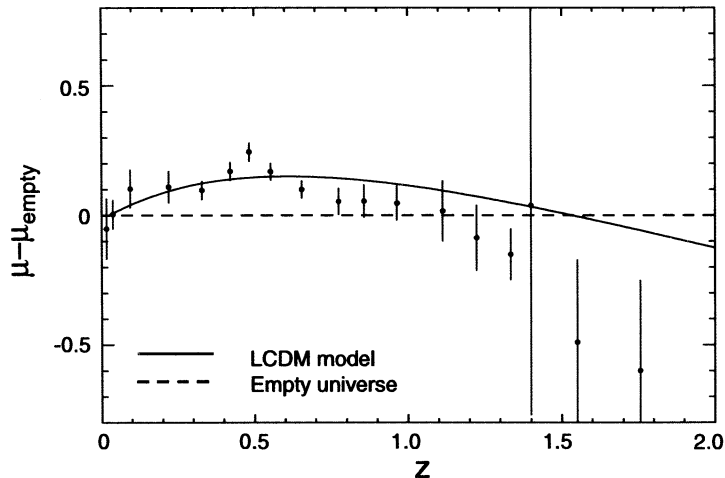
Fig. 12.— The red line shows the luminosity distance relationship predicted for the best-fit WMAP-only model (right column in Table 2). The points show supernova observations from HST (Riess et al. 2007), ESSENCE (Miknaitis et al. 2007), and SNLS (Astier et al. 2006). The plot shows the deviation of the luminosity distances from the empty universe model. The binned data combination is from Wright (2007).

sample of high redshift supernovae has grown by over 80 since the three-year *WMAP* analysis. Recent HST measurements of 21 new high redshift supernova by Riess et al. (2007) include 13 at $z > 1$, allowing the measurement of the Hubble expansion $H(z)$ at distinct epochs and strengthening the evidence for a period of deceleration followed by acceleration. The ESSENCE Supernova Survey has also recently reported results from 102 supernovae discovered from 2002 to 2005 using the 4-m Blanco Telescope at the Cerro Tololo Inter-American Observatory (Miknaitis et al. 2007), of which 60 are used for cosmological analysis (Wood-Vasey et al. 2007). A combined cosmological analysis was performed of the complete supernova data set by Davis et al. (2007).

We confirm in Figure 12 that the recently observed supernovae are consistent with the ΛCDM model, which predicts the luminosity distance μ_{th} as a function of redshift and is compared to the observed data from three independent Type Ia supernovae samples. In our combined analysis we use 135 supernova in the 'Gold' sample, consisting of the original Gold sample described in Riess et al. (2004), updated with revised distance measurements and supplemented by those observed using HST in Riess et al. (2007), together with 60 from the ESSENCE survey, and 115 supernova from the Supernova Legacy Survey (SNLS, Astier et al. (2006)), as described in Spergel et al. (2007). For each supernova the luminosity distance predicted from theory is compared to the observed value. This is derived from measurements of the apparent magnitude m and the inferred absolute magnitude M, to estimate a luminosity distance $\mu_{obs} = 5 \log[d_L(z)/\mathrm{Mpc}] + 25$. The likelihood is given by

$$-2 \ln L = \sum_i [\mu_{obs,i}(z_i) - \mu_{th,i}(z_i, M_0)]^2 / \sigma_{obs,i}^2 \qquad (19)$$

summed over all supernovae, where the absolute magnitude is marginalized over (Lewis & Bridle 2002) and σ_{obs} is the observational error accounting for extinction, intrinsic redshift dispersion, K-correction and light curve stretch factors.

Data	Parameter	Lensing limits	5-year *WMAP* limits
CFHTLS Wide	$\sigma_8(\Omega_m/0.25)^{0.64}$	0.785 ± 0.043	0.814 ± 0.090
100 Sq Deg	$\sigma_8(\Omega_m/0.24)^{0.59}$	0.84 ± 0.07	0.832 ± 0.088
COSMOS 2D	$\sigma_8(\Omega_m/0.3)^{0.48}$	0.81 ± 0.17	0.741 ± 0.069
COSMOS 3D	$\sigma_8(\Omega_m/0.3)^{0.44}$	$0.866^{+0.085}_{-0.068}$	0.745 ± 0.067

Table 3: Measurements of combinations of the matter density, Ω_m, and amplitude of matter fluctuations, σ_8, from weak lensing observations (Fu et al. 2008; Benjamin et al. 2007; Massey et al. 2007), compared to *WMAP*.

4.2.5. Hubble constant measurements

The *WMAP* estimated value of the Hubble constant, $H_0 = 71.9^{+2.6}_{-2.7}s^{-1}$ Mpc^{-1}, assuming a flat geometry, is consistent with the HST measurement of $H_0 = 72 \pm 8$ km s^{-1} Mpc^{-1} (Freedman et al. 2001), where the error includes random and systematic uncertainties. It also agrees within 1σ with a set of measurements from gravitationally lensed systems (Koopmans et al. 2003), measurements from SZ and X-ray observations (Bonamente et al. 2006), and measurements of the Cepheid distances to nearby galaxies that give $H_0 = 73 \pm 6$ km s^{-1} Mpc^{-1} (Riess et al. 2005). More recent measurements include the calibration of the Cepheid distance scale using the distance to the Maser-host galaxy NGC4258 (Macri et al. 2006), with an inferred measure 74 ± 7 km s^{-1} Mpc^{-1} that agrees with the *WMAP* value, and a new measure of the Tully-Fisher zero-point (Masters et al. 2006), that also implies 74 ± 7 km s^{-1} Mpc^{-1}. However, a compilation of Cepheid distance measurements for ten galaxies using HST by Sandage et al. (2006) prefer a lower Hubble constant of 62 ± 6 km s^{-1} Mpc^{-1}, almost 2σ lower than the *WMAP* value. A low measure is also favored by new measurements of an eclipsing binary in M33 (Bonanos et al. 2006), which would imply a reduction to $H_0 = 61$ km s^{-1} Mpc^{-1} of the measurement by Freedman et al. (2001). The opposite effect is found using revised parallaxes for Cepheids (van Leeuwen et al. 2007), which would raise the Sandage et al. (2006) value to 70 ± 5 km s^{-1} Mpc^{-1} and the Freedman et al. (2001) value to 76 ± 8 km s^{-1} Mpc^{-1}. Despite this range of preferred values, none of these measurements are inconsistent with our *WMAP* result for ΛCDM. We only include Hubble constant results for a small set of our combined constraints, using the Freedman et al. (2001) value of 72 ± 8 km s^{-1} Mpc^{-1}, with a Gaussian prior.

4.2.6. Weak Lensing

Weak gravitational lensing is produced by the distortion of galaxy images by the mass distribution along the line of sight. There have been significant advances in the measurement of this effect in recent years, and in the understanding of systematic effects in lensing analyses (e.g., Massey et al. (2007)). There have been improvements in measurements of redshift distributions, and better understanding of intrinsic alignment effects (Hirata et al. 2007), making it a valuable cosmological probe complementary to the CMB. Many early results by lensing surveys favored higher amplitudes of mass fluctuations than preferred by *WMAP*: $\sigma_8 = 0.94^{+0.10}_{-0.14}(\Omega_m/0.25)^{-0.52}$ from the RCS survey (Hoekstra et al. 2002), $0.91 \pm 0.8(\Omega_m/0.25)^{-0.49}$ from the VIRMOS-DESCART survey (Van Waerbeke et al. 2005), and 0.88 ± 0.06 (for $\Omega_m = 0.3$) from the Canada-France-Hawaii Telescope Legacy Survey (CFHTLS) (Hoekstra et al. 2006). However, new measurements of the two-point correlation functions from the third year CFHTLS Wide survey (Fu et al. 2008), covering 57 deg^2, favor a lower amplitude consistent with the *WMAP* measurements: $\sigma_8(\Omega_m/0.25)^{0.64} = 0.785 \pm 0.043$, which agrees with the inferred value from *WMAP*. A comparison of the lensing results with the equivalent

limits derived from *WMAP* is given in Table 3. This shift is due to an improved estimate of the galaxy redshift distribution from CFHTLS-Deep (Ilbert et al. 2006), compared to the distribution obtained from Hubble Deep Field photometric redshifts, a small region of sky whose redshift distribution was dominated by systematic errors. Their measured signal is also in agreement with results from the 100 Square Degree Survey (Benjamin et al. 2007), a compilation of data from the earlier CFHTLS-Wide, RCS and VIRMOS-DESCAT surveys, together with the more recent GABoDS survey (Hetterscheidt et al. 2007) with sky coverage 113 deg^2 and average source redshift $z \sim 0.8$. They find $\sigma_8(\Omega_m/0.24)^{0.59} = 0.84 \pm 0.07$, also consistent with *WMAP*. Both these analyses rely on a two-dimensional measurement of the shear field, comparing the 2D correlation functions with theoretical predictions. Cosmic shear has also been successfully measured in three-dimensions by the HST COSMOS survey (Massey et al. 2007), using redshift information to providing a measure of the mass fluctuation $\sigma_8(\Omega_m/0.3)^{0.44} = 0.866^{+0.085}_{-0.068}$, and a significant improvement over 2D limits from the same sample. This measure is somewhat higher than the *WMAP* value, as shown in Table 3, although not inconsistent.

Weak lensing is also produced by the distortion of the CMB by the intervening mass distribution. This signal can be probed by measuring the correlation of the gravitationally lensed CMB with tracers of large scale structure. A study was done with the *WMAP* first-year data combined with a sample of LRGs from SDSS, but no signal was detected, consistent with theoretical expectation (Hirata et al. 2004). Two recent analyses have found the first evidence for the cross-correlated lensing signal (Smith et al. 2007; Hirata et al. 2008). They use the three-year *WMAP* data correlated with NVSS radio sources (Smith et al. 2007), finding a 3.4σ detection of the correlation, and *WMAP* combined with data from NVSS and SDSS, using both LRGS and quasars (Hirata et al. 2008), finding a correlation with a 2.1σ level of significance. The cross-correlation in both cases is consistent with the five-year *WMAP* ΛCDM model.

4.2.7. Integrated Sachs-Wolfe Effect

Correlation between large-scale CMB temperature fluctuations and large-scale structure is expected in the ΛCDM model due to the change in gravitational potential as a function of time, and so provides a test for dark energy (Boughn et al. 1998). Evidence of a correlation was found in the first-year *WMAP* data (e.g., Nolta et al. (2004)), and has been improved with recent large scale structure data. A recent analysis by Ho et al. (2008) combine 2MASS, SDSS LRGs, SDSS quasars and NVSS radio sources with the *WMAP* three-year data, finding a 3.7σ detection of ISW, consistent with a universe described by the ΛCDM model. They also find a low signal at high redshift $z > 1$, as expected. A similar study by Giannantonio et al. (2008) find a 4σ detection of the correlation. Other recent studies have concentrated on individual data sets, finding a correlation at the level expected with the SDSS DR4 galaxies (Cabré et al. 2006), at high redshift with SDSS qusars (Giannantonio et al. 2006), and with the NVSS radio galaxies (Pietrobon et al. 2006; McEwen et al. 2007).

4.2.8. Ly-α Forest

The Lyα forest seen in quasar spectra probes the underlying matter distribution on small scales, and so provides a long lever arm that can potentially place powerful constraints on the neutrino mass and a running spectral index. However, because they indirectly probe the underlying mass fluctuations, the relationship between absorption line structure and mass fluctuations must be fully understood to be used in a cosmological

analysis. The power spectrum of the Lyα forest has been used to constrain the shape and amplitude of the primordial power spectrum (Viel et al. 2004; McDonald et al. 2005; Seljak et al. 2005; Desjacques & Nusser 2005), and recent results combine the three-year *WMAP* data with the power spectrum obtained from the LUQAS sample of VLT-UVES spectra (Viel et al. 2006) and SDSS QSO spectra (Seljak et al. 2006). Both groups found similar results, suggesting a higher value for σ_8 than consistent with *WMAP*. However, measurements by Kim et al. (2007) of the probability distribution of the Lyα flux have been compared to simulations with different cosmological parameters and thermal histories (Bolton et al. 2007). They imply that the temperature-density relation for the IGM is close to isothermal or inverted, which would result in a smaller amplitude for the power spectrum than previously inferred. This reduction in σ_8 would bring the constraints more in line with the five-year *WMAP* value of $\sigma_8 = 0.796 \pm 0.036$. Given these uncertainties, we choose not to use the Lyα forest data for the main results presented in Komatsu et al. (2008). However, constraints on the running of the spectral index are discussed, using data described in Seljak et al. (2006). With more data and further analyses, the Lyα forest measurements, which probe small scales at intermediate redshifts, have the potential to be a powerful cosmological test.

4.2.9. Big-Bang Nucleosynthesis

WMAP measures the baryon abundance at decoupling, and the ΛCDM model constraint is $\Omega_b h^2 = 0.02273 \pm 0.00062$, with a baryon to photon ratio of $\eta_{10}(\text{WMAP}) = 6.225 \pm 0.170$. Light element abundances also depend on the baryon abundance, but at an earlier epoch, in the first few minutes after the Big Bang. The consistency of these measurements is therefore a powerful test of the Big Bang model. We can infer the BBN-predicted values of η_{10} that correspond to the observed abundances of deuterium, helium, and lithium, and compare them to the CMB. Steigman (2007) reviews the current status of BBN measurements. Deuterium measurements provide the strongest test, and give $\eta_{10}(D) = 6.0 \pm 0.4$ based on new measurements by O'Meara et al. (2006) of a metal-poor damped Lyα system along the sight line of QSO SDSS 1558-003. This is consistent with the *WMAP* measurement. The ^{3}He abundance is more poorly constrained at $\eta_{10}(^3\text{He}) = 5.6^{+2.2}_{-1.4}$ from the measure of $y_3 = 1.1 \pm 0.2$ by Bania et al. (2002). The abundance of ^{4}He corresponds to smaller baryon abundances than consistent with *WMAP*: $\eta_{10}(^4\text{He}) = 2.7^{+1.2}_{-0.9}$ from a measure of $Y_P = 0.240 \pm 0.006$, incorporating data from Izotov & Thuan (2004); Olive & Skillman (2004); Gruenwald et al. (2002) by Steigman (2007). However, observations of five HII regions using new atomic data by Peimbert et al. (2007) predict $\eta_{10}(^4\text{He}) = 7.8 \pm 2$, and higher values are also favored by Fukugita & Kawasaki (2006), both more consistent with *WMAP*.

Measurements of the neutral lithium abundance in low-metallicity stars indicate values two times smaller than the BBN prediction from the CMB. The abundance is often expressed as logarithmic abundance, $[\text{Li}]_P = 12 + \log_{10}(\text{Li}/\text{H})$, and measurements have found $[\text{Li}]_P \sim 2.2 - 2.25$ (Charbonnel & Primas 2005), $[\text{Li}]_P \sim 2.37 \pm 0.05$ (Meléndez & Ramírez 2004) and more recently $[\text{Li}]_P \sim 2.1$ by Asplund et al. (2005). These measurements pose a potential problem for the standard picture, and could be a signature of new early universe physics (see e.g., Coc et al. (2004); Richard et al. (2005); Jedamzik (2004)). However, arguments have been made that the discrepancy could be due to systematics, destruction of lithium in an earlier generation of stars, or uncertainties in the stellar temparature scale (Fields et al. 2005; Steigman 2006; Asplund et al. 2005). A possible solution has recently been proposed using new observations of stars in the globular cluster NGC 6397 (Korn et al. 2006). They find evidence that as the stars age and cool, the proportion of lithium in their atmospheres drops, indicating that transport processes within the star lead to the destruction of lithium. By extrapolating backwards in time, they infer an initial lithium content of the

stars $[Li]_P = 2.54 \pm 0.1$. This is in good agreement with BBN predictions, giving $\eta_{10}(Li) = 5.4 \pm 0.6$. More observations will help determine whether this is the correct explanation for the observed discrepancy.

4.2.10. Strong Lensing

Because the strong lensing cross-section is exponentially sensitive to distance, the number of strongly lensed quasars has the potential to probe cosmology, as a dark energy dominated universe predicts a large number of gravitational lenses (Turner 1990; Fukugita et al. 1990). Until recently, attempts to use this method have been limited both by the lack of large lens searches with well-understood systematics, and by uncertainties in both the source and lens populations. However, for both optically and radio-selected strongly lensed surveys, the observational data continues to improve. The CLASS radio band survey now has a large statistical sample of radio lenses (Myers et al. 2003; Koopmans et al. 2003; York et al. 2005). Analyses of this sample yields estimates for $\Omega_\Lambda \simeq 0.72 - 0.78$ (Mitchell et al. 2005; Chae 2007). Oguri et al. (2008) have recently analyzed the large statistical lens sample from the Sloan Digital Sky Quasar Lens Search (Oguri et al. 2006), a sample that avoids many of the limitations of previous optical surveys. For a $w = -1$, flat cosmology, they find $\Omega_\Lambda = 0.74^{+0.11}_{-0.15}$(stat.)$^{+0.13}_{-0.06}$(syst.). These values are all consistent with our best fit cosmology.

The abundance of giant arcs has the potential to probe both the mass distribution in clusters and the underlying cosmology. Recent surveys have detected large numbers of giant arcs (Gladders et al. 2003; Sand et al. 2005; Hennawi et al. 2008). A number of authors have argued that their number and size is problematic for ΛCDM (Li et al. 2006; Broadhurst & Barkana 2008). This discrepancy has led to interest in early dark energy models (Fedeli & Bartelmann 2007) that predict higher lensing cross-sections. However, because of the sensitivity to the mass distribution, there is controversy over the predictions of ΛCDM models. Detailed numerical simulations (Meneghetti et al. 2007; Hennawi et al. 2007; Hilbert et al. 2007a; Neto et al. 2007) find that the lens cross-sections are sensitive to the details of the mass distribution as well as to the effect of baryon physics (Wambsganss et al. 2007; Hilbert et al. 2007b): most of these effects tend to increase the predicted number of giant arcs. Detailed comparisons between numerical simulations and systematic observational studies will be essential for this technique to be a useful test of cosmological models.

4.2.11. Galaxy clusters

Because clusters are easily detected and probe the high mass end of the mass distribution, they probe the amplitude of density fluctuations and of large-scale structure. Cluster observations at optical wavelengths provided some of the first evidence for a low density universe with the current preferred cosmological parameters (see e.g., the Fan et al. (1997) analysis which found $\sigma_8 = 0.83 \pm 0.15$ and $\Omega_m = 0.3 \pm 0.1$). Observers are now using a number of different techniques for identifying cluster samples: large optical samples, X-ray surveys, lensing surveys (see e.g., Wittman et al. (2006)) and Sunyaev-Zeldovich surveys. The challenge for all of these survey techniques is to accurately determine the selection function and the relationship between astronomical observables and mass. Over the past few years, there has been significant progress in improving the astronomical observable mass/light relationship in both the optical (Lin et al. 2006; Sheldon et al. 2007; Reyes et al. 2008; Rykoff et al. 2008) and the X-ray (Sheldon et al. 2001; Reiprich & Böhringer 2002; Kravtsov et al. 2006; Arnaud et al. 2007; Hoekstra 2007). There are now large new optical cluster samples (Bahcall et al. 2003; Hsieh et al. 2005; Miller et al. 2005; Koester et al. 2007) and new X-ray samples (Pierre

et al. 2006).

While there has been tension between σ_8 estimates from different cluster techniques, most recent results are converging on values close to the *WMAP* best fit value of $\sigma_8 = 0.796 \pm 0.036$. Cosmological constraints from RCS (Gladders et al. 2007) finds $\Omega_m = 0.30^{+0.12}_{-0.11}$ and $\sigma_8 = 0.70^{+0.27}_{-0.1}$. Rozo et al. (2007) argues for $\sigma_8 > 0.76$ (95% confidence level) from SDSS BCG samples. Mantz et al. (2007) find $\Omega_m = 0.27^{+0.06}_{-0.05}$ and $\sigma_8 = 0.77^{+0.07}_{-0.06}$ for a flat model based on the Jenkins et al. (2001) mass function and the Reiprich & Böhringer (2002) mass-luminosity calibration. With a 30% higher zero-point, Rykoff et al. (2008) find that their data are best fit by $\sigma_8 = 0.85$ and $\Omega_m = 0.24$. Bergé et al. (2007) report $\sigma_8 = 0.92^{+0.26}_{-0.30}$ for $\Omega_m = 0.24$ from their joint CFHTLS/XMM-LSS analysis. Over the next few years, cosmologists anticipate a number of large SZ surveys that have the potential to make accurate measurements of σ_8. Planck (Bartlett et al. 2008) should detect a large and well defined cluster sample. Simulations and theoretical analysis suggest a tight correlation between SZ signal and cluster mass (da Silva et al. 2004; Motl et al. 2005; Nagai 2006; Reid & Spergel 2006; Afshordi 2007). While SZ surveys are beginning to test these relationships (Muchovej et al. 2007), they will need to be empirically tested in large samples before the SZ measurements are competitive with other techniques.

4.2.12. Galaxy peculiar velocities

By measuring galaxy velocity fields, observations can probe the growth rate of structure. For nearby galaxies where accurate density measurements are possible, these galaxy velocity fields can be compared directly to observations of large-scale structure. For larger scale surveys, measurements of redshift space distortions can be used to infer the growth rate of structure. While none of these measurements yet has the precision of the cosmological tests used in the joint analyses, they do provide an independent consistency check (see Nesseris & Perivolaropoulos (2008) for a recent review).

One approach is to use objects with well-determined distances to look for deviations from the Hubble flow. Measurements of Tully-Fisher distances to galaxies enable a direct comparison of these deviations from the Hubble flow to the local density field (Strauss & Willick 1995; Dekel 2000; Zaroubi et al. 2001). For example, the Park & Park (2006) analysis of the peculiar velocities in the SFI sample find $\sigma_8 \Omega_m^{0.6} = 0.56^{+0.27}_{-0.21}$. With the much large SFI++ sample (Springob et al. 2007), the precision of this test should improve. Nearby supernova also show deviations from the local flow and can be used as velocity field probes (Riess et al. 1995; Haugbølle et al. 2007). Using the currently available data sets, Gordon et al. (2007) correlate peculiar velocities of nearby supernova and find $\sigma_8 = 0.79 \pm 0.22$.

With the development of deep large-scale structure surveys, cosmologists have now been able measure β, the amplitude of redshift space distortions as a function of redshift. When combined with a measurement of the bias, b, this yields a determination of the growth rate of structure $f \equiv d\ln G/d\ln a = \beta b$, where G is the growth factor. For Einstein gravity theories, regardless of the nature of the dark energy, we expect $f \simeq \Omega^\gamma$ with $\gamma \simeq 6/11$ (see Polarski & Gannouji (2007) for a more accurate fitting function). Analysis of redshift space distortions in the 2dF galaxy redshift survey (Peacock et al. 2001; Verde et al. 2002; Hawkins et al. 2003) find $\beta = 0.47 \pm 0.08$ at $z \simeq 0.1$, consistent with the ΛCDM predictions for the best fit *WMAP* parameters. The Tegmark et al. (2006) analysis of the SDSS LRG sample finds $\beta = 0.31 \pm 0.04$ at $z = 0.35$. The Ross et al. (2007) analysis of the 2dF-SDSS LRG sample find $\beta = 0.45 \pm 0.05$ at z = 0.55. The Guzzo et al. (2008) analysis of 10,000 galaxies in the VIMOS-VLT Deep Survey finds that $\beta = 0.70 \pm 0.26$ at $z = 0.8$ and infer $d\ln G/d\ln a = 0.91 \pm 0.36$, consistent with the more rapid growth due to matter domination at this
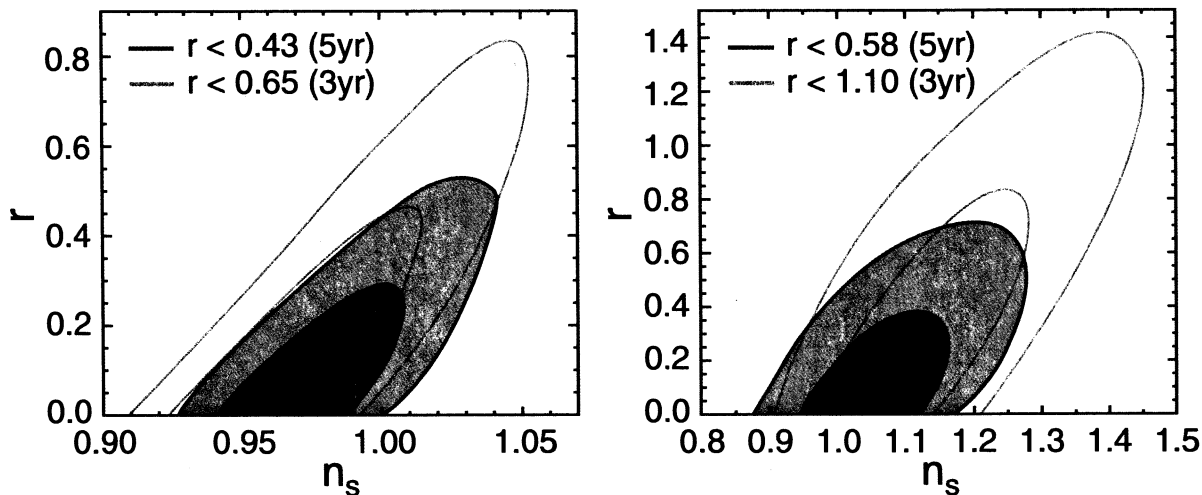
Fig. 13.— Two-dimensional marginalized constraints (68% and 95% confidence levels) on inflationary parameters r, the tensor-to-scalar ratio, and n_s, the spectral index of fluctuations, defined at $k_0 = 0.002/\text{Mpc}$. One-dimensional 95% upper limits on r are given in the legend. Left: The five-year *WMAP* data places stronger limits on r (shown in blue) than three-year data (grey). This excludes some inflationary models including $\lambda\phi^4$ monomial inflaton models with $r \sim 0.27$, $n_s \sim 0.95$ for 60 e-folds of inflation. Right: For models with a possible running spectral index, r is now more tightly constrained due to measurements of the third acoustic peak. Note: the two-dimensional 95% limits correspond to $\Delta(2\ln L) \sim 6$, so the curves intersect the $r = 0$ line at the $\sim 2.5\sigma$ limits of the marginalized n_s distribution.

epoch expected in a ΛCDM model. The da Ângela et al. (2008) analysis of a QSO sample finds $\beta = 0.60^{+0.14}_{-0.11}$ at $z = 1.4$ and use the clustering length to infer the bias. Extrapolating back to $z = 0$, they find a matter density of $\Omega_m = 0.25^{+0.09}_{-0.07}$.

Peculiar velocity measurements can also probe the shape of the galaxy power spectrum. The Watkins & Feldman (2007) analysis of large scale flows finds that the power spectrum space parameter $\Gamma \simeq \Omega_m h = 0.13^{+0.09}_{-0.05}$, consistent with ΛCDM values.

5. Extended cosmological models with *WMAP*

The *WMAP* data place tight constraints on the simplest ΛCDM model parameters. In this section we describe to what extent *WMAP* data constrain extensions to the simple model, in terms of quantifying the primordial fluctuations and determining the composition of the universe beyond the standard components. Komatsu et al. (2008) present constraints for *WMAP* combined with other data, and offer a more detailed cosmological interpretation of the limits.
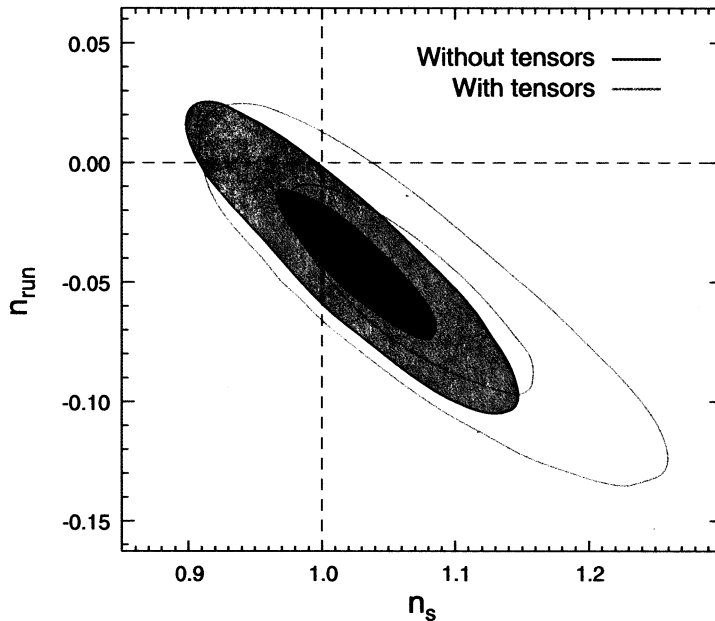
Fig. 14.— Two-dimensional marginalized limits for the spectral index, n_s, defined at $k_0 = 0.002/\mathrm{Mpc}$, and the running of the index $dn_s/d\ln k$ (marked n_{run}). Models with no tensor contribution, and with a tensor contribution marginalized over, are shown. In both cases the models are consistent with a power-law spectral index, with $dn_s/d\ln k = 0$, as expected from the simplest inflationary models.

5.1. Primordial perturbations

5.1.1. Tensor fluctuations

In the ΛCDM model, primordial scalar fluctuations are adiabatic and Gaussian, and can be described by a power law spectrum,

$$\Delta_{\mathcal{R}}^2(k) \propto \left(\frac{k}{k_0}\right)^{n_s-1}, \tag{20}$$

producing CMB angular power spectra consistent with the data. Limits can also be placed on the amplitude of tensor fluctuations, or gravitational waves, that could have been generated at very early times. They leave a distinctive large-scale signature in the polarized B-mode of the CMB (e.g., Basko & Polnarev (1980); Bond & Efstathiou (1984)), that provides a clean way to distinguish them from scalar fluctuations. However, we have not yet reached sensitivities to strongly constrain this signal with the polarization data from *WMAP*. Instead we use the tensor contribution to the temperature fluctuations at large scales to constrain the tensor-to-scalar ratio r. We define $r = \Delta_h^2(k_0)/\Delta_{\mathcal{R}}^2(k_0)$, where Δ_h^2 is the amplitude of primordial gravitational waves (see Komatsu et al. (2008)), and choose a pivot scale $k_0 = 0.002/\mathrm{Mpc}$.

The *WMAP* data now constrain $r < 0.43$ (95% CL). This is an improvement over the three-year limit of $r < 0.65$ (95% CL), and comes from the more accurate measurement of the second and third acoustic peaks. The dependence of the tensor amplitude on the spectral index is shown in Figure 13, showing the $n_s - r$ degeneracy (Spergel et al. 2007): a larger contribution from tensors at large scales can be offset by an increased spectral index, and an overall decrease in the amplitude of fluctuations, shown in Table 4. The

Parameter	Tensors	Running	Tensors+Running
r	< 0.43 (95% CL)		< 0.58 (95% CL)
$dn_s/d\ln k$		-0.037 ± 0.028	-0.050 ± 0.034
n_s	0.986 ± 0.022	$1.031^{+0.054}_{-0.055}$	$1.087^{+0.072}_{-0.073}$
σ_8	$0.777^{+0.040}_{-0.041}$	0.816 ± 0.036	0.800 ± 0.041

Table 4: Selection of cosmological parameter constraints for extensions to the ΛCDM model including tensors and/or a running spectral index.

degeneracy is partially broken with a better measure of the TT spectrum. There is a significant improvement in the limit on models whose scalar fluctuations can vary with scale, with a power spectrum with a 'running' spectral index,

$$n_s(k) = n_s(k_0) + \frac{1}{2}\frac{dn_s}{d\ln k}\ln\left(\frac{k}{k_0}\right). \tag{21}$$

The limit from *WMAP* is now $r < 0.58$ (95% CL), about half the three-year value $r < 1.1$ (Spergel et al. 2007).

What do these limits tell us about the early universe? For models that predict observable gravitational waves, it allows us to exclude more of the parameter space. The simplest inflationary models predict a nearly scale-invariant spectrum of gravitational waves (Grishchuk 1975; Starobinsky 1979). In a simple classical scenario where inflation is driven by the potiential $V(\phi)$ of a slowly rolling scalar field, the predictions (Lyth & Riotto 1999) are

$$r \simeq 4\alpha/N \tag{22}$$

$$1 - n_s \simeq (\alpha + 2)/2N \tag{23}$$

for $V(\phi) \propto \phi^\alpha$, where N is the number of e-folds of inflation between the time when horizon scale modes left the horizon and the end of inflation. For N=60, the $\lambda\phi^4$ model with $r \simeq 0.27$, $n_s \simeq 0.95$ is now excluded with more than 95% confidence. An $m^2\phi^2$ model with $r \simeq 0.13$, $n_s \simeq 0.97$ is still consistent with the data. Komatsu et al. (2008) discuss in some detail what these measurements, and constraints for combined data sets, imply for a large set of possible inflationary models and potentials.

With $r = 0$ also fitting the data well, models that do not predict an observable level of gravitational waves, including multi-field inflationary models (Polarski & Starobinsky 1995; Garcia-Bellido & Wands 1996), D-brane inflation (Baumann & McAllister 2007), and ekpyrotic or cyclic scenarios (Khoury et al. 2001; Boyle et al. 2004), are not excluded if one fits for both tensors and scalars.

5.1.2. Scale dependence of spectral index

The running of the spectral index has been the subject of some debate in light of *WMAP* observations, with the three-year data giving limits of $dn_s/d\ln k = -0.055 \pm 0.030$, showing some preference for decreasing power on small scales (Spergel et al. 2007). Combined with high-ℓ CBI and VSA CMB data, a negative running was preferred at $\sim 2\sigma$. A running index is not predicted by the simplest inflationary models (see e.g., Kosowsky & Turner (1995)), and the detection of a scale dependence would have interesting consequences for early universe models. Deviations from a power law index, and their consequences, have been considered by a number of groups in light of three-year data, including Easther & Peiris (2006); Kinney et al. (2006);
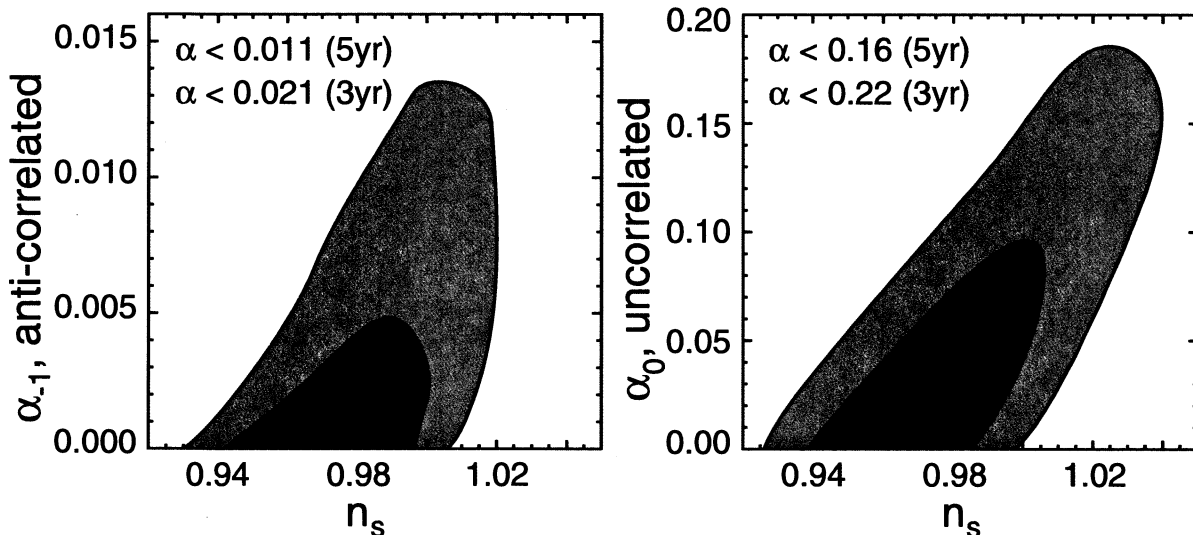
Fig. 15.— Marginalized two-dimensional limits (68% and 95%) on the amplitude of possible CDM entropy (or isocurvature) fluctuations. The one-dimensional 95% upper limits are given in the legend. Left: Anti-correlated fluctuations are tightly constrained, placing limits on curvaton models. Right: Uncorrelated fluctuations, corresponding to axion models for dark matter, add less power to the CMB spectrum than the anti-correlated case, for a given α, so higher values of α_0 are allowed (than α_{-1}), by the data. In both cases the amplitude is correlated with the spectral index of curvature fluctuations n_s, which compensates for the large scale power added by the CDM entropy fluctuations.

Shafieloo & Souradeep (2007); Verde & Peiris (2008), using various parameterizations. In this analysis, and in Komatsu et al. (2008) we consider only a running index parameterized as in Eqn 21.

We show in Figure 14 that with a better determination of the third acoustic peak, coupled with improved beam determination, the five-year *WMAP* data do not significantly prefer a scale-dependent index. The limit on the running is $dn_s/d\ln k = -0.037 \pm 0.028$ for models with no tensor contribution. The running is anti-correlated with the tensor amplitude (Spergel et al. 2003, 2007), so the positive prior on the tensor amplitude leads to a more negative running preferred, $dn_s/d\ln k = -0.050 \pm 0.034$, when a tensor contribution is marginalized over. Both limits are well within 2σ of zero, showing no evidence of departure from a power law spectral index.

5.1.3. Entropy perturbations

The simplest classical single-field inflation models predict solely adiabatic fluctuations, but entropy (or isocurvature) fluctuations are also predicted in a wide range of scenarios, including axions (Seckel & Turner 1985; Linde 1985), multi-field inflation (Polarski & Starobinsky 1994; Garcia-Bellido & Wands 1996; Linde & Mukhanov 1997), and decay of fields such as the curvaton (Lyth & Wands 2002; Moroi & Takahashi 2001; Bartolo & Liddle 2002; Lyth et al. 2003). They may be correlated with the adiabatic fluctuations to some degree, depending on the model. Most physical scenarios generate only CDM or baryon entropy fluctuations

Parameter	$\beta = -1$	$\beta = 0$
α_{-1}	< 0.011 (95% CL)	
α_0		< 0.16 (95% CL)
n_s	0.983 ± 0.017	0.987 ± 0.022
σ_8	$0.778^{+0.039}_{-0.038}$	0.777 ± 0.038

Table 5: Subset of cosmological parameter constraints for ΛCDM models with additional anti-correlated ($\beta = -1$) or uncorrelated ($\beta = 0$) entropy fluctuations.

(Bond & Efstathiou 1987; Peebles 1987), with perturbation

$$\mathcal{S}_c = \frac{\delta\rho_c}{\rho_c} - \frac{3\delta\rho_\gamma}{4\rho_\gamma}, \tag{24}$$

for CDM with density ρ_c. Neutrino modes are also possible (Bucher et al. 2000). It has been known for some time that the CMB data cannot be fit by pure entropy fluctuations (Stompor et al. 1996; Langlois & Riazuelo 2000), but a contribution may be allowed. Several groups have placed limits on a variety of models using the *WMAP* one-year and three-year data (Peiris et al. 2003; Valiviita & Muhonen 2003; Bucher et al. 2004; Beltran et al. 2004; Dunkley et al. 2005; Kurki-Suonio et al. 2005; Lewis 2006; Bean et al. 2006; Trotta 2007; Keskitalo et al. 2007), finding no strong evidence for entropy fluctuations. Significant levels have been found to be consistent with the CMB data (Bucher et al. 2004; Moodley et al. 2004; Bean et al. 2006), but require correlated admixtures of CDM and neutrino isocurvature perturbations that are hard to motivate physically.

Here, and in Komatsu et al. (2008), we quantify the relative contributions to the angular power spectrum following Beltran et al. (2004); Bean et al. (2006), with

$$C_\ell = (1 - \alpha)C_\ell^{\mathcal{R}} + \alpha C_\ell^{\mathcal{S}} + 2\beta\sqrt{\alpha(1 - \alpha)}C_\ell^X, \tag{25}$$

summing the spectra from curvature fluctuations $C_\ell^{\mathcal{R}}$, entropy fluctuations $C_\ell^{\mathcal{S}}$ with power spectrum

$$\Delta_S^2(k)\delta^3(\mathbf{k} - \mathbf{k}') = (k/2\pi)^3\langle\mathcal{S}_c(\mathbf{k})\mathcal{S}_c(\mathbf{k}')\rangle, \tag{26}$$

and a cross-correlation spectrum C_ℓ^X with power spectrum $\Delta_X^2(k)\delta^3(\mathbf{k} - \mathbf{k}') = (k/2\pi)^3\langle-\mathcal{R}(\mathbf{k})\mathcal{S}_c(\mathbf{k}')\rangle$. This follows the definition of the curvature perturbation $\mathcal{R}$ in Komatsu et al. (2008), which gives large-scale temperature anisotropy $\Delta T/T = -\mathcal{R}/5$. An anti-correlated spectrum with $\beta = -1$ gives a positive C_ℓ^X on large scales.

Limits are found for α_{-1}, corresponding to anti-correlated models with $\beta = -1$. This could correspond to a curvaton scenario in which inflation is driven by an inflaton field, but CDM perturbations are generated by the decay of a distinct curvaton field (see e.g., Lyth & Wands (2002)). In this case we make the assumption that the spectral index of the anti-uncorrelated entropy fluctuations is equal to the adiabatic spectral index. We do not find evidence for curvaton entropy pertubations, finding a limit from *WMAP* of $\alpha_{-1} < 0.011$ (95% CL), shown in Figure 15 and in Table 5. This is half the three-year limit, and places strong lower limits on the possible density of the curvaton at its decay, in this scenario, compared to the total energy density (Komatsu et al. 2008). If the curvaton dominated at decay, the perturbations would be purely adiabatic. Where has the improvement come from? The pure entropy spectrum and the cross-correlated spectrum both add large scale power, so a similar degeneracy is seen with the spectral index, and
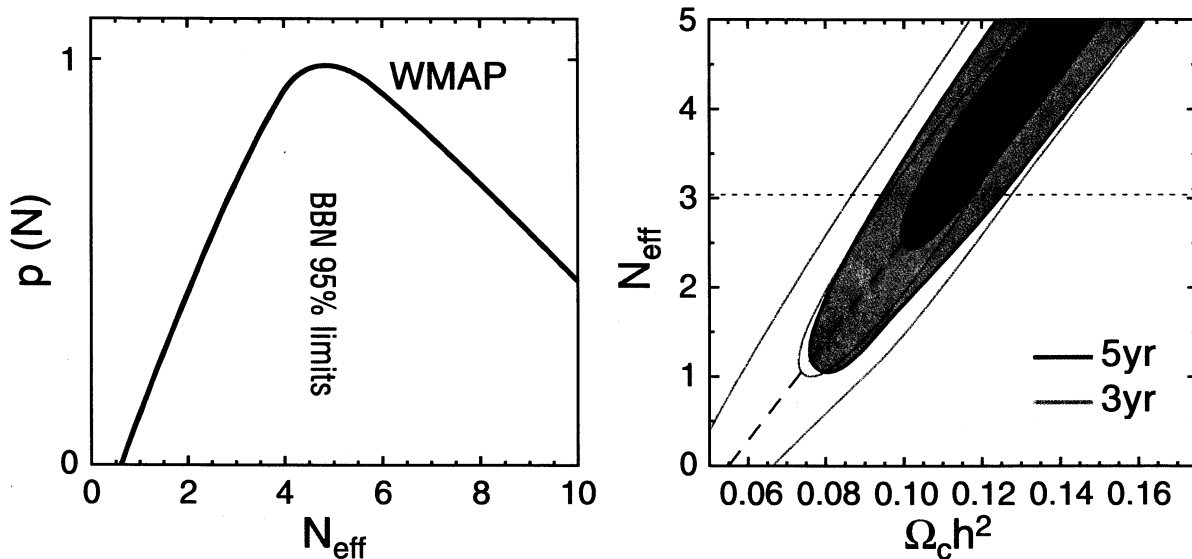
Fig. 16.— Evidence for a non-zero effective number of neutrino species, N_{eff}. Left: The marginalized probability distribution gives $N_{eff} > 2.3$ (95% CL) from *WMAP* alone. The best-fit ΛCDM model with $N_{eff} = 0$ is a poorer fit to the data than $N_{eff} = 3$, with $\Delta\chi^2 = 8.2$. Inferred 95% limits from big bang nucleosynthesis (BBN) observations are highlighted. Right: Joint two-dimensional distribution for N_{eff} and the CDM density, $\Omega_c h^2$, with five-year limits in blue, compared to three-year limits in grey. The degeneracy valley of constant z_{eq} is shown dashed, indicating that the CMB is now sensitive to the effect of neutrino anisotropic stress, which breaks the degeneracy.

σ_8, as in the case where the tensor amplitude is varied. The entropy spectrum is also out of phase with the adiabatic spectrum, so the improved TE measurements combine with the third peak TT spectrum to tighten the limits.

We also place limits on α_0, corresponding to an uncorrelated model with $\beta = 0$. In this case the entropy spectral index is set to be scale invariant. Komatsu et al. (2008) describe how this corresponds to entropy perturbations created by axions, which would constitute some part of the dark matter budget. The limit is $\alpha_0 < 0.16$ (95% CL), ten times higher than the anti-correlated amplitude, but still preferring pure adiabatic fluctuations. Without the large-scale power contribution from the anti-correlated spectrum, a much larger amplitude is permitted, but with the same degeneracy with the spectral index and σ_8. This has implications for the maximum deviation from adiabaticity of axion dark matter and photons. Komatsu et al. (2008) provide a discussion of the theoretical implications of these limits, and those for combined data, for both models considered.

5.2. Composition and geometry of the Universe

5.2.1. Number of relativistic species

Neutrinos are expected to play an important role in the dynamics of the early universe. For standard parameters, they contribute about 40% of the energy density of the universe during the radiation epoch
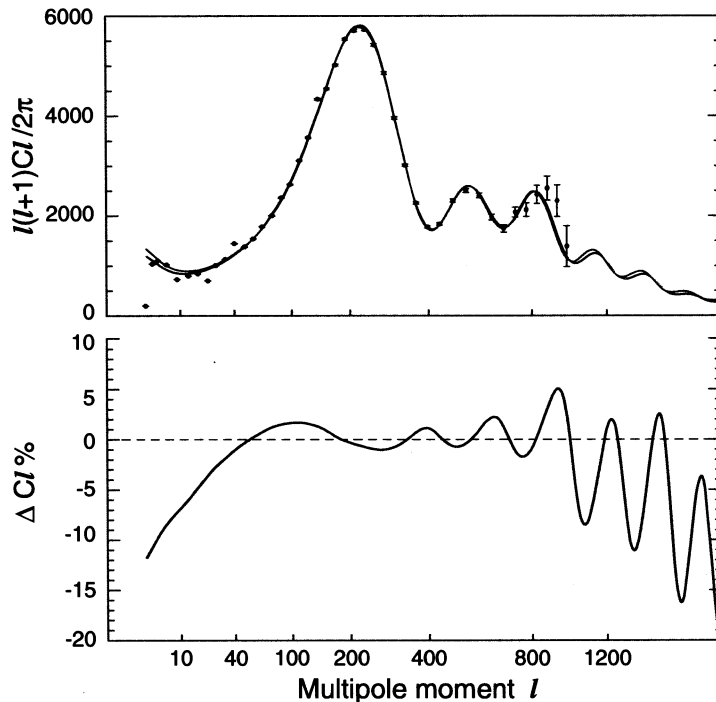
Fig. 17.— Comparison of the CMB angular power spectrum for the best-fit ΛCDM models with the standard $N_{\text{eff}} = 3.04$ neutrino species (red), and with $N_{\text{eff}} = 0$ species (blue). The lower panel shows the fractional difference between the two spectra when N_{eff} is increased from 0 to 3.04. The $N_{\text{eff}} = 0$ model has a lower $\Omega_m h^2$ in order to fit the third peak, and a lower spectral index, n_s, compared to the $N_{\text{eff}} = 3.04$ model.

and about 11% of the energy density of the universe at $z \sim 1100$ (very close to the energy density in baryons). Because neutrinos contribute to the expansion of the universe and stream relativistically out of density fluctuations, they produce a significant imprint on the growth rate of structure and on the structure of the microwave background fluctuations. The amplitude of these effects depend upon N_{eff}, the number of effective neutrino species. By 'effective neutrinos species', we are counting any particle that is relativistic at $z \sim 1000 - 3000$, couples very weakly to the baryon-electron-photon fluid, and has very weak self-interactions. Because we know neutrinos exist, we associate 'neutrinos' with 'light relativistic particle', but note that in the strictest sense we limit only light relativistic species, as the cosmological constraints are sensitive to the existence of *any* light species produced during the big bang or any additional contribution to the energy density of the universe (e.g., primordial magnetic fields).

Measurements of the width of the Z provide very tight limits on the number of neutrino species: $N_\nu = 2.984 \pm 0.008$ (Particle Data Book), consistent with the 3 light neutrino species in the standard model. Because of non-thermal effects due to the partial heating of neutrinos during the $e^\pm$ annihilations, and other small corrections, the effective number of species is 3.0395 (Dicus et al. 1982; Mangano et al. 2002). Most analyses of the number of neutrino species with three-year *WMAP* data (Spergel et al. 2007; Ichikawa et al. 2007; Mangano et al. 2007; Hamann et al. 2007; de Bernardis et al. 2007) relied on combining CMB measurements with probes of the growth rate of structure. Since one of the signatures of the number of neutrino species is a change in the growth rate of structure, there are degeneracies between the properties of

Parameter	Limits
N_{eff}	> 2.3 (95% CL)
$\sum m_\nu$	< 1.3 eV (95% CL)
Y_P	< 0.45 (95% CL)

Table 6: Constraints on neutrino properties and the primordial helium fraction.

the neutrinos and of the dark energy. Neutrinos, however, leave a distinctive signature directly on the CMB power spectrum (see Bashinsky & Seljak (2004) for detailed discussion): the neutrinos not only suppress the CMB peak heights, they also shift the acoustic peak positions. While the effects that depend on shifts in the epoch of matter/radiation equality are degenerate with changes in the matter density, the effects of neutrino free-streaming are distinct. Changes in the baryon/matter ratio and the baryon/photon ratio also have their own imprints on the Silk damping scale and on the acoustic scale. With five years of data, we are now able to see evidence of the effects of the neutrinos on the CMB power spectrum.

Figure 16 shows the limits on the number density of neutrinos and the density in dark matter. The degeneracy valley, shown in the right panel, corresponds to a constant ratio of matter density to radiation density, or equivalently a measurement of the expansion factor at matter radiation equality:

$$
\begin{aligned}
1 + z_{eq} &= a_{eq}^{-1} = \frac{\rho_c + \rho_b}{\rho_\gamma + \rho_\nu} \\
&\simeq 40500 \, \frac{\Omega_c h^2 + \Omega_b h^2}{1 + 0.23 N_{\text{eff}}}.
\end{aligned}
\tag{27}
$$

With only 3 years of data and a lack of precision on the third peak position and height, *WMAP* was not able to make a clear detection of neutrinos (or relativistic species); however, the data did provide a $\sim 2\sigma$ hint of the effects of neutrino anisotropic stresses (Melchiorri & Serra 2006). Figure 16 shows that the five year data alone, we now constrain the number density of relativistic species: $N_{\text{eff}} > 2.3$ (95% CL). By bounding $N_{\text{eff}} < 10$, and choosing a uniform prior on N_{eff}, this level of significance depends somewhat on the prior. We therefore test the significance of the constraint by comparing two ΛCDM models: one with $N_{\text{eff}} = 0$, and one with the standard $N_{\text{eff}} = 3.04$. We find that the data prefer $N_{\text{eff}} = 3.04$. The best-fit model has $\Delta(-2 \ln L) = 8.2$ less than the $N_{\text{eff}} = 0$ best-fit model, corresponding to evidence for relativistic species at $> 99.5\%$ confidence. The CMB power spectra corresponding to these two models, and their fractional difference, are shown in Figure 17. The model with no neutrinos has a lower matter density, $\Omega_m h^2$, in order to keep z_{eq} fixed. The improvement in likelihood between the two models comes from both the low-ℓ and high-ℓ TT spectrum, with a small contribution from the TE spectrum. We also check that this evidence does not go away if we relax the assumption of a power-law spectral index, by testing a model with a variable running, $dn_s/d \ln k \neq 0$.

Komatsu et al. (2008) combine *WMAP* data with other distance indicators (which constrain $\Omega_c h^2$) and finds a stronger limit on the number density of neutrino species: $N_{\text{eff}} = 4.4 \pm 1.5$. These limits will continue to improve as CMB measurements of the higher peaks improve. The CMB constraints on the number of relativistic species at redshift $\sim$1000-3000 complement constraints from big bang nucleosynthesis and from particle accelerators. Measurements of the abundance of Helium are sensitive to the expansion rate of the universe during its first few minutes (Steigman et al. 1977). The agreement between the best fit value from big bang nucleosynthesis, $N_{\text{eff}} = 3.24 \pm 1.2$ (95% confidence interval) (Cyburt et al. (2005), Particle Data Book 2007), with the best fit CMB value is another consistency check for standard cosmology.
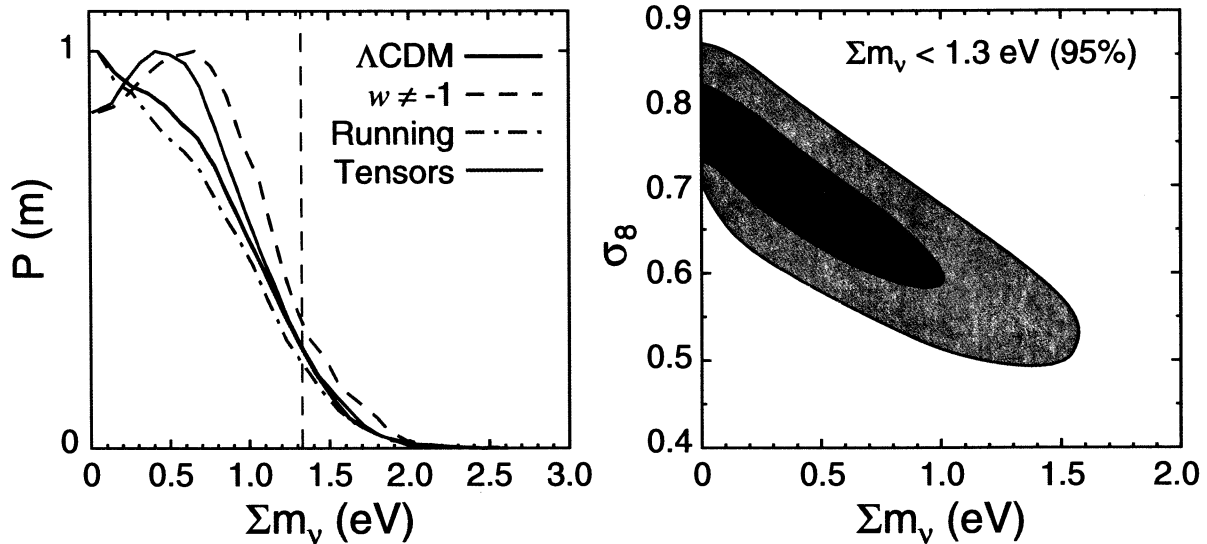
Fig. 18.— Limits on the sum of neutrino masses with the *WMAP* five-year data. Left: The marginalized one-dimensional limit from *WMAP* alone is $\sum m_\nu$ < 1.3 eV (95% CL). This is raised by <10% with marginalization over a running spectral index, tensor fluctuations, or a dark energy equation of state w. Right: The neutrino mass is anti-correlated with σ_8, the amplitude of matter fluctuations.

5.2.2. Neutrino mass

Cosmological data places limits on the mass of neutrinos. Atmospheric and solar neutrino experiments show that neutrinos are massive (see Mohapatra et al. (2005)), and measure the difference between the square of their masses, $m_{\nu i}^2 - m_{\nu j}^2$. Cosmological measurements constrain the sum of the masses $\sum m_\nu$ due to their effect on the propagation of perturbations, on the clustering of matter, and on the expansion rate of the universe (Bond & Szalay 1983; Ma 1996; Hu et al. 1998). The mass has a large effect on the matter power spectrum, as massive neutrinos do not cluster as well as cold dark matter, leading to a suppression in power on small scales. Neutrinos also affect the CMB at earlier times: if the fraction of dark matter that is warm is raised, acoustic oscillations in the photon-baryon plasma are less strongly damped for modes that entered the horizon while the neutrinos were relativistic, raising the acoustic peak amplitudes. The radiation-like behavior at early times also changes the expansion rate, shifting the peak positions.

These effects are somewhat degenerate with other parameters, so CMB data alone cannot limit the mass as well as when combined with other data. With the three-year *WMAP* data alone the limits were $\sum m_\nu$ < 1.8 eV (Spergel et al. 2007), and < 0.66 eV when combined with other data. Since the three-year *WMAP* analysis there have been many studies of the constraints, as discussed in Komatsu et al. (2008).

The five-year *WMAP* data now gives an upper limit on the total mass to be $\sum m_\nu$ < 1.3 eV (95% CL), shown in Table 6. We have checked that this upper limit is robust to the choice of cosmological models. The upper limit is raised by < 10% when we include tensor fluctuations, a running spectral index, or a constant $w \neq -1$ equation of state of dark energy, as shown in Figure 18. This dependence on additional parameters is consistent with earlier investigations by e.g., Crotty et al. (2004); Zunckel & Ferreira (2007). A larger neutrino mass raises the amplitude of the higher acoustic peaks, hence the observed degeneracy

with σ_8 (Figure 18). Stronger constraints come from combining the CMB data with probes of the expansion rate and clustering of matter at later times: Komatsu et al. (2008) find $\sum m_\nu < 0.61$ (95% CL) for *WMAP* combined with additional data.

5.2.3. *Primordial Helium Abundance*

In most cosmological analyses the primordial helium abundance is fixed to be $Y_P = 0.24$, motivated by observations discussed in Sec 4.2.9. The effect of the abundance on the CMB spectrum is small, but provides an independent cross-check of the BBN results, and probes for any difference between the helium abundance during the first few minutes, and after 300,000 years. The abundance affects the CMB at small scales due to the recombination process. The number density of electrons before recombination depends on the helium fraction through $n_e = n_b(1 - Y_P)$ where n_b is the baryon number density. Changing the electron number density changes the mean free path of Compton scattering, which affects the Silk damping scale. A larger Y_p increasingly damps the power on small scales, as shown in Trotta & Hansen (2004).

Constraints from the first-year *WMAP* data were presented in Trotta & Hansen (2004); Huey et al. (2004); Ichikawa & Takahashi (2006), with 99% upper limits of $Y_P < 0.65$ inferred (Trotta & Hansen 2004). A subsequent analysis of the three-year data gave $Y_P < 0.61$ at 95% confidence, tightened to 0.25 ± 0.10 with small-scale CMB data (Ichikawa et al. 2007). We now find $Y_P < 0.45$ (95% CL) with the five-year *WMAP* data. Higher values allowed by the thre-year data are disfavored with a better measure of the third acoustic peak height. With future small-scale CMB measurements constraints should significantly improve (Ichikawa et al. 2007).

5.2.4. *Curvature of the universe*

In combination with other data, *WMAP* observations place strong constraints on the geometry of the universe (Spergel et al. 2007). The CMB measures with high accuracy the angular scale at which acoustic oscillations are imprinted at the last scattering surface, $\theta_* = 0.5952 \pm 0.0017$ °. However, this alone does not provide a good measure of the geometry, as there is a degeneracy with the expansion rate of the universe since last scattering. This is shown in Figure 19, indicating the degeneracy between the dark energy density Ω_Λ and the curvature Ω_k. With *WMAP* alone the curvature is poorly constrained to $\Omega_k = -0.099^{+0.085}_{-0.100}$, with $\Omega_\Lambda < 0.76$ (95% CL), assuming a Hubble prior of $20 < H_0 < 100$ and $\Omega_\Lambda > 0$. The same degeneracy is seen, although slightly broadened, when the dark energy equation of state is allowed to vary. However, in both cases the Hubble constant decreases with increasingly negative curvature, taking values inconsistent with observation. This degeneracy can be used to constrain the curvature by combining observations (Jungman et al. 1996). In the three-year *WMAP* analysis, Spergel et al. (2007) showed that the degeneracy is truncated with the addition of only one piece of additional cosmological data (Type Ia supernovae, or the HST measurement of the Hubble constant, or galaxy power spectra), tightly constraining any deviations from flatness. Komatsu et al. (2008) draw similar conclusions with currently available data, and discuss the current limits on the spatial curvature from recent observations.
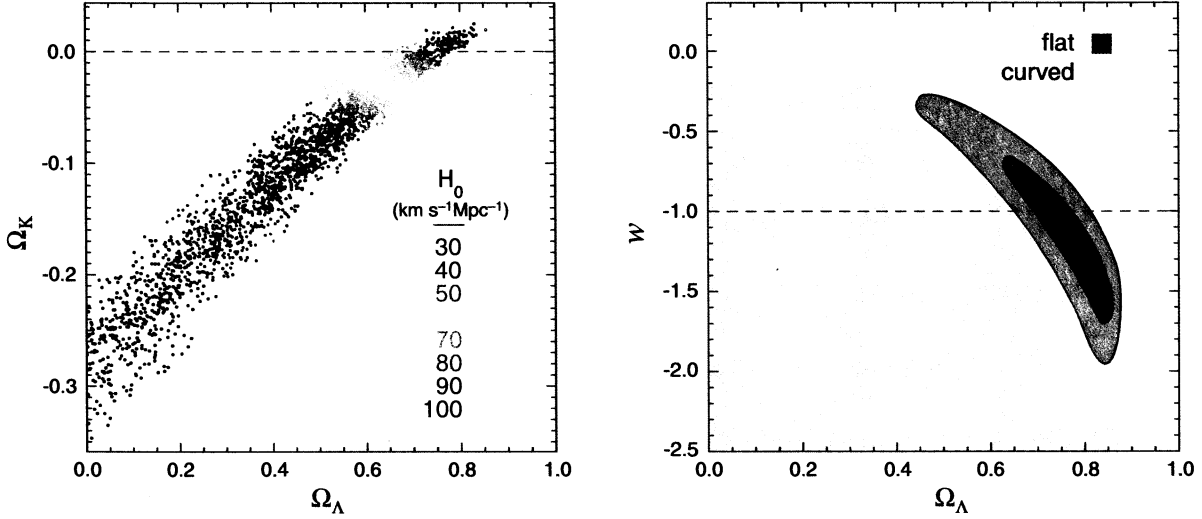
Fig. 19.— Left: The points show the set of non-flat models consistent with the *WMAP* data, colored by the Hubble constant values. *WMAP* measures the acoustic peak scale to high accuracy, but does not constrain the curvature, Ω_k, by itself. However, the highly curved models have a low Hubble constant, inconsistent with observation. Right: Constraints on the dark energy equation of state, w, and the dark energy density, Ω_Λ, from *WMAP* alone. With a Hubble constant $H_0 < 100$, weak limits can be placed on w in a flat universe, shown by the blue contours, but the dark energy density and equation of state are unconstrained (with the 95% confidence level shaded grey) if the assumption of flatness is relaxed. Limits are significantly improved when *WMAP* is combined with additional data (Komatsu et al. 2008).

5.2.5. Dark energy properties

The ΛCDM model requires a non-zero dark energy density $\Omega_\Lambda = 0.742 \pm 0.030$ to fit the data, which is assumed to be in the form of a cosmological constant. We do not have an explanation for this component of the universe. A natural explanation could be a vacuum energy density (Carroll et al. 1992), but if so, we are faced with the fine-tuning problem to explain its observed value, 120 orders of magnitude smaller than expected from field theory arguments. Alternative explanations include quintessence (Peebles & Ratra 1988; Wetterich 1988; Ferreira & Joyce 1998) or modifications to gravity (Deffayet et al. 2002). Testing the dark energy equation of state today, and as a function of cosmic time will help identify the possible explanation.

The CMB by itself cannot place strong limits on the equation of state $w = p/\rho$, but by measuring the acoustic peak positions and heights, and constraining $\Omega_m h^2$ with the third peak, limits the range of models to a degeneracy between Ω_m and w, shown in Figure 19. The dark energy in these models is allowed to cluster. With a prior on the Hubble constant $H_0 < 100$, *WMAP* alone places weak limits $w = -1.06^{+0.41}_{-0.42}$, with $\Omega_\Lambda = 0.73^{+0.10}_{-0.11}$. If flatness is not assumed, the *WMAP* data cannot constrain w or Ω_Λ due to the geometric degeneracy, also shown in Figure 19. However, the situation is significantly improved when *WMAP* is combined with astronomical data measuring the expansion rate and clustering of matter at late times. Komatsu et al. (2008) discuss limits obtained from various data in combination with *WMAP*, and find w constrained to be -1 to within 6% for a flat universe and constant equation of state.

6. Conclusions

The simple six parameter ΛCDM model continues to fit the *WMAP* data. With five years of observations, we have better measured both the temperature and polarization anisotropy of the CMB. This has allowed us to measure with smaller errors, compared to the three-year analysis, the third acoustic peak in the temperature spectrum, and the low-ℓ polarization signal, leading to improved constraints on the cosmological parameters describing the contents of the universe, and the primordial fluctuations that seeded structure. The observations continue to be well fit by the predictions of the simplest inflationary models, with a scale-invariant spectrum of fluctuations disfavored. Consistency with the TE cross-correlation spectrum, now measured with better accuracy, provides additional confidence in this simple model.

We have detected the optical depth to reionization with high significance. This measurement implies that reionization of the universe likely took place gradually, as it constrains a sudden reionization to be earlier than consistent with other observations. With more data, it will become possible to use the polarization data to better quantify the ionization history. Given the improvement in this measurement, and with a view to interpreting future large-scale polarization measurements, we develop an alternative way to remove Galactic foregrounds from low resolution polarization maps, which includes marginalization over uncertainties in the Galactic signal. We find consistent results using this method and the standard template-cleaning method.

Considering a range of extended models, we continue to find that the standard ΛCDM model is consistently preferred by the data. The improved measurement of the third peak now requires the existence of light relativistic species, assumed to be neutrinos, at high confidence. The standard scenario has three neutrino species, but the three-year *WMAP* data could not rule out models with none. The ΛCDM model also continues to succeed in fitting a substantial array of other observations. Certain tensions between other observations and those of *WMAP*, such as the amplitude of matter fluctuations measured by weak lensing surveys and using the Ly-α forest, and the primordial lithium abundance, have either been resolved with improved understanding of systematics, or show promise of being explained by recent observations. With further *WMAP* observations we will better probe both the universe at a range of epochs, measuring fluctuation characteristics to probe the initial inflationary process, or other non-inflationary scenario, improving measurements of the composition of the universe at the recombination era, and characterizing the reionization process in the universe.

A.   Tests of polarization cleaning using Gibbs sampling

There are a number of prior assumptions made in the Gibbs-cleaning code used to estimate polarized CMB and Galactic foregrounds. Here we test their effect on the estimated CMB maps, using the stand-alone τ code described in Page et al. (2007) as a diagnostic. The value of τ is varied, and the exact likelihood computed for fixed TT first peak height, and fixed cosmological parameters.

We do not place priors on the Q and U amplitude of synchrotron emission, but do limit the spectral behavior. In the fiducial model we assume a power-law spectral index, with spectral indices defined using the spectral index mask in Figure 3. Within each of the 30 regions, the index has a Gaussian prior -3.0 ± 0.15. Changing the mask to have an alternative 30 regions where the sky is divided into equal-sized regions, or only 15, has almost no effect on the recovered τ (see Table 7), and recovers spectral index maps with similar features. The North Polar Spur and Galactic anti-center consistently prefer spectral indices of ~ -3.1, given the prior. To use many more regions would require some modification to the current sampling method: the index parameters are sampled using Metropolis steps, so many more parameters would take a much longer time to converge. Alternative methods have been used in e.g. Eriksen et al. (2007) to sample index parameters. Since the Gaussian prior is rather tight, we test its effect by both moving the central value to -2.8, and widening the range to ± 0.2. When it is broadened, the convergence is poor unless we also impose a hard prior of $\beta > -2.5$. In this case we find $\tau = 0.096 \pm 0.18$, close to the fiducial value. To use broader priors it may be necessary to impose alternative priors on the indices, such as Jeffrey's priors (Eriksen et al. 2007).

We make assumptions about both the spectral index and amplitude of the dust emission. The index is fixed at $\beta_d = 1.7$ in the fiducial model. Changing it to $\beta = 2$ has no effect on the recovered τ value, as shown in Table 7. We also impose priors on the amplitudes of the dust Q and U Stokes vectors. In the fiducial case the amplitude of Q and U in each pixel, defined at W band, has a Gaussian prior $0 \pm 0.2 I_d(n)$, where I_d is the intensity of dust from the FDS map, as well as a hard bound on the polarization amplitude, $P(n) < 0.2 I_d(n)$. If the upper limit is raised to 50% in both cases, much higher than expected theoretically, there is a stronger degeneracy between the CMB and dust components, and the error on τ is raised and the central value lowered, with $\tau = 0.090 \pm 0.021$. This effect increases if we set the limit at 100%, or fully polarized, in which case $\tau = 0.085 \pm 0.025$. We also checked with the three-year data that varying the central value of the prior to $Q = 0.05 \cos(2\gamma_K) I_d$, $U = 0.05 \sin(2\gamma_K) I_d$, where γ_K are the K-band polarization angles,

Description	τ
Fiducial	0.101 ± 0.017
Index mask 2 (30 regions)	0.098 ± 0.017
Index mask 3 (15 regions)	0.100 ± 0.017
$\beta_s = -2.8 \pm 0.15$	0.103 ± 0.018
$\beta_s = -3.0 \pm 0.2$	0.096 ± 0.018
$\beta_d = 2$	0.100 ± 0.017
$P_d \leq 0.5 I_d$	0.090 ± 0.021
$P_d \leq I_d$	0.085 ± 0.025
KKaQVW	0.093 ± 0.016

Table 7: Limits on the optical depth, τ, for a variety of assumptions made for Gibbs sampling the low resolution polarization maps.
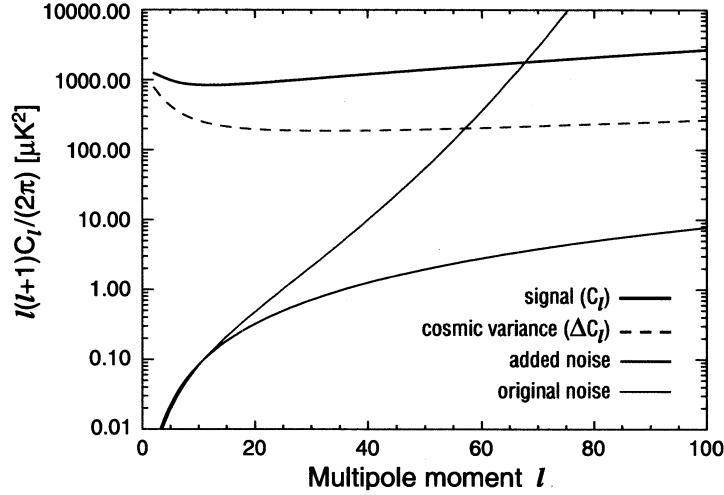
Fig. 20.— The angular power spectra of signal and noise components in the smoothed ILC map used for Gibbs sampling the low-ℓ temperature spectrum. Uncorrelated noise, at 2 μK per pixel (red), is added to the smoothed ILC map to speed up the sampling, and then is assumed to be the only noise present. This assumption is inaccurate at low ℓ, as it ignores the true noise (blue), but the error is negligible since it is significantly lower than cosmic variance (green).

had a negligible effect on the results. In the absence of a good prior for the polarization amplitudes (e.g. from higher frequency observations), this highlights the importance of the dust intensity map as a means of limiting the polarized dust contribution.

Finally, we use the KKaQV data combination for our fiducial result, but find similar limits on the optical depth when W band is included, with $\tau = 0.093 \pm 0.016$. However, we choose not to use W band in the standard analysis, due to concerns about systematic effects (Hinshaw et al. 2008).

B.   Low-ℓ TT likelihood cross checks

We have switched from the pixel likelihood to a Blackwell-Rao (BR) estimator at low ell, so perform several tests to verify that the new likelihood 1) is consistent with the pixel likelihood, 2) is insensitive to several choices of input data, and 3) is properly converged. Many of our checks involve comparing likelihoods. Because the likelihood is a function on a high dimensional space, we do not check it everywhere. Instead

resolution parameter	4	5
smoothing FWHM	9.1831°	5.0°
σ_{noise}/pixel [μK]	1.0	2.0
ℓ_{max} sampled	32	51
ℓ_{max} conditioned	48	96

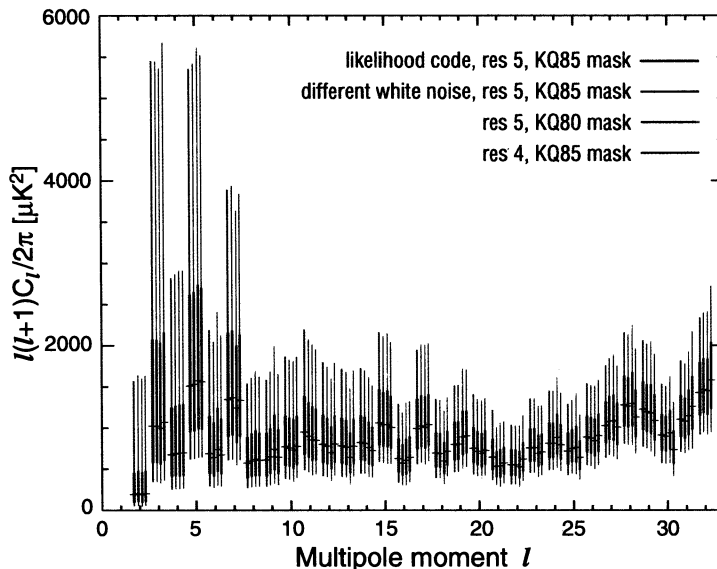Table 8: Parameters used for sampling the low-ℓ TT likelihood at two different resolutions.

Fig. 21.— The level of variation in the low-ell TT Gibbs likelihood that arises from different input parameters. The spectrum estimated from the standard input (black) is compared to results obtained using a different white noise realization (blue), using a larger mask (KQ80,red), and degrading to $N_{\rm side} = 16$ (green) rather then 32. The likelihood does fluctuate with these changes, but has a negligible effect on cosmological parameters. The values shown at each multipole correspond to maximum likelihood values obtained by fixing the spectrum of other multipoles at fiducial values. The error bars show where the likelihood is at 50% and 5% of its peak value.

we choose some fiducial spectrum and compute slices through the likelihood. We compare these conditional likelihoods, typically in the form of maximum likelihood values and full-width-half-max error bars between different low-ℓ likelihood methods. We also compare ΛCDM cosmological parameters obtained using the different inputs.

The first comparison is between the pixel-based code and the Gibbs code. Figure 4 showed a comparison of the C_ℓ likelihoods, with no significant differences, even though they use different resolutions. The cosmological parameters are unchanged for the two codes. Next, the Gibbs sampling can use maps degraded to $N_{\rm side} = 16$ or 32 (or higher resolution). Table 8 lists details of runs at these two different resolutions, including the standard deviation of Gaussian white noise added to the smoothed maps. The power spectrum of the white noise for the $N_{\rm side} = 32$ case, is compared to the input noise and cosmic variance in Figure 20. Power spectra are sampled up to $\ell_{\rm max}$ (sampled), and the sampled CMB skies are constructed with the sampled power spectra and by conditioning on a constant fiducial spectrum out to a higher value of $\ell_{\rm max}$ (conditioned). In Figure 21 the estimated spectra are compared, using the fiducial KQ85 mask. There are some small differences, but the spectra are consistent.

We also show in Figure 21 that the spectra obtained are almost identical for two different realizations for the added uncorrelated white noise, and that using the larger KQ80 mask, compared to the fiducial KQ85, has a small effect on the spectra and cosmological parameters, consistent with noise. Finally we compare results for different $\ell_{\rm max}$ used in the BR estimator. The standard set-up uses $\ell_{\rm max} = 32$; using the low-ℓ

likelihood up to $\ell = 51$ has almost no effect on cosmological parameters.

C.   Parameter estimation details

C.1.   Sampling method

In the primary pipeline, only one chain is run for each model, rather than the typical four or eight parallel chains used in most MCMC cosmological analyses. This is possible as our spectral convergence test only requires a single chain. The starting points are picked as good-fitting points from previous analyses (e.g., a good-fitting value from the three-year *WMAP* analysis), or previous test chains, which means that no initial burn-in need be removed. Starting afresh with the five-year data, one can always use a point lying in the *WMAP* three-year limits as a starting point. This would not be the case for entirely new distributions, or much improved data, in which case we run a short initial exploratory chain to find the high likelihood region.

The covariance matrix from which trial steps are drawn, is chosen using a best guess for the covariance C of the distribution being sampled. For a multi-variate Gaussian with covariance $\mathbf{C}$, the optimal trial covariance matrix is $\mathbf{C}_T = (\sigma_T/\sigma_0)^2 \mathbf{C}$, where

$$\frac{\sigma_T}{\sigma_0} \approx \frac{2.4}{\sqrt{D}} \tag{C1}$$

for D-dimensional distributions (Hanson & Cunningham 1998; Dunkley et al. 2005). This relation also holds for somewhat non-Gaussian distributions. At each step we draw a vector $\mathbf{G}$ of D Gaussian unit variance zero mean random variates, and compute a trial set of parameters $\mathbf{x}_T$, starting from the current position $\mathbf{x}_i$, where

$$\mathbf{x}_T = \mathbf{x}_i + \sqrt{\mathbf{C}_T}\mathbf{G}. \tag{C2}$$

Using an appropriate covariance matrix can speed up the sampling time by a factor of hundreds. In practice we have a good idea of the covariance from previous cosmological analyses, so this is always used as a starting point. With significantly different data, or with new parameters, a best guess is made. The chains are then run for a few thousand steps, and then updated if the matrix is inadequate. This is determined by the acceptance rate of the chain, which should be $\sim 15 - 25\%$ and by the chain efficiency, using the spectral test described in the next section. A second or third update may be required for models such as those with curved geometries with variable dark energy equation of state. Once a good covariance matrix is found, the chains are run for typically 20,000 steps, and then tested for convergence. Convergence for ΛCDM chains typically takes place after only $\sim$6000 iterations, although at this point the 1D and 2D distributions are noisy. In practice we then run all the chains for longer than the convergence limit, typically for 100,000 iterations, in order to get well sampled histograms. The chains are not thinned before analysis.

C.2.   Spectral convergence test

A chain has 'converged' when its statistical properties reflect those of the underlying distribution with sufficient accuracy. To determine this stopping point, we use the spectral convergence test described in Dunkley et al. (2005) in our main parameter pipeline. The power spectrum of each parameter of the chain is used as a diagnostic, to check whether the chain has (1) sampled the distribution in such a way that it

is unbiased by correlations, and (2) sampled enough points that statistics can be estimated with sufficient accuracy. The Gelman & Rubin test (Gelman & Rubin 1992), commonly used in cosmology, can sometimes fail to test the first point, producing a false positive.

To estimate the power spectrum $P(k)$ from a chain of length N we construct $\hat{P}_j = |a_j|^2$, where $j = 2\pi k/N$, by taking the discrete Fourier Transform of the chain of values for each parameter, x,

$$a_j = \frac{1}{\sqrt{N}} \sum_{n=0}^{N-1} x(n) \, \exp\left[i2\pi(jn/N)\right] \tag{C3}$$

where $-(N/2 - 1) < j < N/2$. $x(n)$ is the value at each iteration n, so chains stored in weighted format are converted to unweighted arrays for analysis. Since the Metropolis algorithm produces chains which are correlated on small scales, the power spectrum tends to a white noise spectrum on large scales, and turns over to a spectrum with suppressed power at large k, with the turnover position reflecting the inverse correlation length. In Dunkley et al. (2005) it is shown that the spectrum can be fit by the following template:

$$P(k) = P_0 \frac{(k^*/k)^\alpha}{(k^*/k)^\alpha + 1}, \tag{C4}$$

with P_0 giving the amplitude of the white noise spectrum in the $k \to 0$ limit. k^* indicates the position of the turnover to a different power law behavior, characterized by α, at large k. This model is shown in Figure 3 of Dunkley et al. (2005), fitting the noisy spectrum of a parameter from a chain. The model fits the noise-averaged spectrum of a real chain obtained from Monte-Carlo simulations, also shown in Dunkley et al. (2005).

To fit the parameters $\ln P_0, k^*$ and α to $\hat{P}_j$ using least squares for a finite chain, we have

$$\ln \hat{P}_j = \ln[P_0] + \ln\left[\frac{(Nk^*/2\pi j)^\alpha}{1 + (Nk^*/2\pi j)^\alpha}\right] - \gamma + r_j, \tag{C5}$$

where $\gamma = 0.577216$ is the Euler-Mascheroni constant, and r_j are random measurement errors. The parameters are fit over the range of Fourier modes $1 \leq j \leq 10j^*$, for a spectrum with $j^* = k^*(N/2\pi)$, so we iterate twice to converge on the j^* limit.

For convergence, the largest scales probed must be in the white noise regime $P(k) \sim k^0$, defined by the requirement $j^* > 20$ for each parameter. This insures that the correlated points are not biasing the distribution and indicates that the chain is drawing points throughout the full region of high probability. To test sufficient accuracy, we require the convergence ratio $r = \sigma_{\bar{x}}^2/\sigma_0^2$ to be less than 1% for each parameter, where $\sigma_{\bar{x}}^2$ is the variance in the sample mean, and σ_0^2 is the variance of the sampled parameter. The Gelman & Rubin test incorporates a similar ratio: their R statistic roughly translates to $R \sim 1 + r$, but the quantity is calculated using multiple parallel chains. It is shown in Dunkley et al. (2005) that r can be estimated using a single chain, since estimating the sample mean variance of a long chain, with zero mean, is equivalent to estimating $P(k)$ at $k = 0$:

$$\sigma_{\bar{x}}^2 = \left\langle \bar{x}^2 \right\rangle \approx \frac{1}{N} \cdot P(k = 0). \tag{C6}$$

In practice we rescale each parameter to have zero mean and unit variance before computing its power spectrum. Then we estimate the value of P_0 for each parameter, to compute $r = P_0/N$. We require $r < 0.01$, but in practice obtain much smaller values, typically with $r < 0.001$.

REFERENCES

Afshordi, N. 2007, ArXiv e-prints, 704

Arnaud, M., Pointecouteau, E., & Pratt, G. W. 2007, A&A, 474, L37

Asplund, M., Nissen, P. E., Lambert, D. L., Primas, F., & Smith, V. V. 2005, in IAU Symposium, ed. V. Hill, P. François, & F. Primas, 53–58

Astier, P., et al. 2006, A&A, 447, 31

Bahcall, N. A., et al. 2003, ApJS, 148, 243

Bania, T. M., Rood, R. T., & Balser, D. S. 2002, Nature, 415, 54

Barkana, R. & Loeb, A. 2006, MNRAS, 371, 395

Barkats, D. et al. 2005, ApJ, 619, L127

Barnes, III, T. G., Jefferys, W. H., Berger, J. O., Mueller, P. J., Orr, K., & Rodriguez, R. 2003, ApJ, 592, 539

Bartlett, J. G., Chamballu, A., Melin, J.-B., Arnaud, M., & Members of the Planck Working Group 5. 2008, Astronomische Nachrichten, 329, 147

Bartolo, N. & Liddle, A. R. 2002, Phys. Rev. D, 65, 121301

Bashinsky, S. & Seljak, U. 2004, Phys. Rev. D, 69, 083002

Basko, M. M. & Polnarev, A. G. 1980, MNRAS, 191, 207

Baumann, D. & McAllister, L. 2007, Phys. Rev. D, 75, 123508

Bean, R., Dunkley, J., & Pierpaoli, E. 2006, Phys. Rev., D74, 063503

Beck, R. 2001, Space Science Reviews, 99, 243, kluwer Academic Publishers

Becker, G. D., Rauch, M., & Sargent, W. L. W. 2007, ApJ, 662, 72

Becker, R. H. e. a. 2001, AJ, 122, 2850

Beltran, M., Garcia-Bellido, J., Lesgourgues, J., & Riazuelo, A. 2004, Phys. Rev., D70, 103530

Benjamin, J., et al. 2007, MNRAS, 381, 702

Bennett, C. L., et al. 2003, ApJ, 583, 1

Berdyugin, A., Teerikorpi, P., Haikala, L., Hanski, M., Knude, J., & Markkanen, T. 2001, A&A, 372, 276

Bergé, J., et al. 2007, ArXiv e-prints, 712

Bischoff, C., et al. 2008, ArXiv e-prints, 802

Blake, C., Collister, A., Bridle, S., & Lahav, O. 2007, MNRAS, 374, 1527

Bolton, J. S. & Haehnelt, M. G. 2007, MNRAS, 382, 325

Bolton, J. S., Viel, M., Kim, T. ., Haehnelt, M. G., & Carswell, R. F. 2007, ArXiv e-prints, 711

Bonamente, M., Joy, M. K., LaRoque, S. J., Carlstrom, J. E., Reese, E. D., & Dawson, K. S. 2006, ApJ, 647, 25

Bonanos, A. Z., et al. 2006, ApJ, 652, 313

Bond, J. R. & Efstathiou, G. 1984, ApJ, 285, L45

Bond, J. R. & Efstathiou, G. 1987, MNRAS, 226, 655

Bond, J. R. & Szalay, A. S. 1983, ApJ, 274, 443

Boughn, S. P., Crittenden, R. G., & Turok, N. G. 1998, New Astronomy, 3, 275

Boyle, L. A., Steinhardt, P. J., & Turok, N. 2004, Phys. Rev. D, 69, 127302

—. 2006, Physical Review Letters, 96, 111301

Broadhurst, T. & Barkana, R. 2008, ArXiv e-prints, 801

Bucher, M., Dunkley, J., Ferreira, P. G., Moodley, K., & Skordis, C. 2004, Physical Review Letters, 93, 081301

Bucher, M., Moodley, K., & Turok, N. 2000, Phys. Rev. D, 62, 083508

Bunker, A., Stanway, E., Ellis, R., McMahon, R., Eyles, L., Lacy, M., Stark, D., & Chiu, K. 2007, in Astronomical Society of the Pacific Conference Series, Vol. 380, Deepest Astronomical Surveys, ed. J. Afonso, H. C. Ferguson, B. Mobasher, & R. Norris, 27–+

Cabré, A., Gaztañaga, E., Manera, M., Fosalba, P., & Castander, F. 2006, MNRAS, 372, L23

Carroll, S. M., Press, W. H., & Turner, E. L. 1992, ARA&A, 30, 499

Cen, R. 2003, ApJ, 591, L5

Chae, K.-H. 2007, ApJ, 658, L71

Charbonnel, C. & Primas, F. 2005, A&A, 442, 961

Chiu, W. A., Fan, X., & Ostriker, J. P. 2003, Astrophys. J., 599, 759

Choudhury, T. R. & Ferrara, A. 2006, MNRAS, 371, L55

Clocchiatti, A., et al. 2006, ApJ, 642, 1

Coc, A., Vangioni-Flam, E., Descouvemont, P., Adahchour, A., & Angulo, C. 2004, ApJ, 600, 544

Cole, S., et al. 2005, MNRAS, 362, 505

Crotty, P., Lesgourgues, J., & Pastor, S. 2004, Phys. Rev., D69, 123007

Crutcher, R., Heiles, C., & Troland, T. 2003, in Lecture Notes in Physics, Berlin Springer Verlag, Vol. 614, Turbulence and Magnetic Fields in Astrophysics, ed. E. Falgarone & T. Passot, 155–181

Cyburt, R. H., Fields, B. D., Olive, K. A., & Skillman, E. 2005, Astroparticle Physics, 23, 313

da Ângela, J., et al. 2008, MNRAS, 383, 565

da Silva, A. C., Kay, S. T., Liddle, A. R., & Thomas, P. A. 2004, MNRAS, 348, 1401

Davis, L. J. & Greenstein, J. L. 1951, ApJ, 114, 206

Davis, T. M., et al. 2007, ApJ, 666, 716

de Bernardis, F., Melchiorri, A., Verde, L., & Jimenez, R. 2007, ArXiv e-prints, 707

Deffayet, C., Dvali, G., & Gabadadze, G. 2002, Phys. Rev. D, 65, 44023

Dekel, A. 2000, in Astronomical Society of the Pacific Conference Series, Vol. 201, Cosmic Flows Workshop, ed. S. Courteau & J. Willick, 420–+

Desjacques, V. & Nusser, A. 2005, MNRAS, 361, 1257

Dickinson, C., et al. 2004, MNRAS, 353, 732

Dicus, D. A. et al. 1982, Phys. Rev., D26, 2694

Djorgovski, S. G., Castro, S., Stern, D., & Mahabal, A. A. 2001, ApJ, 560, L5

Dobler, G. & Finkbeiner, D. P. 2007, ArXiv e-prints, 712

Draine, B. T. 2003, ARA&A, 41, 241

Draine, B. T. & Lazarian, A. 1999, ApJ, 512, 740

Draine, B. T. & Li, A. 2007, ApJ, 657, 810

Duncan, A. R., Haynes, R. F., Jones, K. L., & Stewart, R. T. 1995, MNRAS, 277, 36

Dunkley, J., Bucher, M., Ferreira, P. G., Moodley, K., & Skordis, C. 2005, MNRAS, 356, 925

Dunkley, J., Bucher, M., Ferreira, P. G., Moodley, K., & Skordis, C. 2005, Phys. Rev. Lett., 95, 261303

Dunkley, J. et al. 2008, In preparation

Easther, R. & Peiris, H. 2006, JCAP, 0609, 010

Efstathiou, G. 2004, Mon. Not. Roy. Astron. Soc., 348, 885

Eisenstein, D. J., et al. 2005, ApJ, 633, 560

Eriksen, H. K., et al. 2004, ApJS, 155, 227

—. 2006, ApJ, 641, 665

—. 2007, ApJ, 656, 641

Fan, X., Bahcall, N. A., & Cen, R. 1997, ApJ, 490, L123+

Fan, X., Carilli, C. L., & Keating, B. 2006, ARA&A, 44, 415

Fan, X., et al. 2000, AJ, 120, 1167

—. 2001, AJ, 122, 2833

Fedeli, C. & Bartelmann, M. 2007, A&A, 461, 49

Ferreira, P. G. & Joyce, M. 1998, Phys. Rev. D, 58, 023503

Fields, B. D., Olive, K. A., & Vangioni-Flam, E. 2005, ApJ, 623, 1083

Finkbeiner, D. P., Davis, M., & Schlegel, D. J. 1999, ApJ, 524, 867

Freedman, W. L., et al. 2001, ApJ, 553, 47

Fu, L., et al. 2008, A&A, 479, 9

Fukugita, M., Futamase, T., & Kasai, M. 1990, MNRAS, 246, 24P

Fukugita, M. & Kawasaki, M. 2006, ApJ, 646, 691

Furlanetto, S. R., Oh, S. P., & Briggs, F. H. 2006, Phys. Rep., 433, 181

Garcia-Bellido, J. & Wands, D. 1996, Phys. Rev., D53, 5437

Gelfand, A. E. & Smith, A. F. M. 1990, Jour. Amer. Statist. Assn, 85, 398

Gelman, A. & Rubin, D. 1992, Statistical Science, 7, 457

Geweke, J. & Tanizaki, H. 2001, Computational Statistics & Data Analysis, 37, 151

Giannantonio, T., Scranton, R., Crittenden, R. G., Nichol, R. C., Boughn, S. P., Myers, A. D., & Richards, G. T. 2008, ArXiv e-prints, 801

Giannantonio, T., et al. 2006, Phys. Rev. D, 74, 063520

Gladders, M. D., Hoekstra, H., Yee, H. K. C., Hall, P. B., & Barrientos, L. F. 2003, ApJ, 593, 48

Gladders, M. D., Yee, H. K. C., Majumdar, S., Barrientos, L. F., Hoekstra, H., Hall, P. B., & Infante, L. 2007, ApJ, 655, 128

Gold, B. et al. 2008, ApJS

Gordon, C., Land, K., & Slosar, A. 2007, Physical Review Letters, 99, 081301

Gorski, K. M., Hivon, E., Banday, A. J., Wandelt, B. D., Hansen, F. K., Reinecke, M., & Bartlemann, M. 2005, ApJ, 622, 759

Grishchuk, L. P. 1975, Sov. Phys. JETP, 40, 409

Gruenwald, R., Steigman, G., & Viegas, S. M. 2002, ApJ, 567, 931

Guzzo, L., et al. 2008, Nature, 451, 541

Haiman, Z. & Holder, G. P. 2003, Astrophys. J., 595, 1

Hamann, J., Hannestad, S., Raffelt, G. G., & Wong, Y. Y. Y. 2007, JCAP, 0708, 021

Han, J.-L. 2006, Chinese Journal of Astronomy and Astrophysics, submitted (astro-ph/0603512)

Hanson, K. M. & Cunningham, G. S. 1998, Proc. SPIE, 3338, 371

Haugbølle, T., Hannestad, S., Thomsen, B., Fynbo, J., Sollerman, J., & Jha, S. 2007, ApJ, 661, 650

Hawkins, E., et al. 2003, MNRAS, 346, 78

Heiles, C. 2000, AJ, 119, 923

Hennawi, J. F., Dalal, N., Bode, P., & Ostriker, J. P. 2007, ApJ, 654, 714

Hennawi, J. F., et al. 2008, AJ, 135, 664

Hetterscheidt, M., Simon, P., Schirmer, M., Hildebrandt, H., Schrabback, T., Erben, T., & Schneider, P. 2007, A&A, 468, 859

Hilbert, S., White, S. D. M., Hartlap, J., & Schneider, P. 2007a, MNRAS, 382, 121

—. 2007b, ArXiv e-prints, 712

Hildebrand, R. H. & Dragovan, M. 1995, ApJ, 450, 663

Hill, R. et al. 2008, ApJS

Hinshaw, G., et al. 2007, ApJS, 170, 288

Hinshaw, G. et al. 2008, ApJS

Hirata, C. M., Ho, S., Padmanabhan, N., Seljak, U., & Bahcall, N. 2008, ArXiv e-prints, 801

Hirata, C. M., Mandelbaum, R., Ishak, M., Seljak, U., Nichol, R., Pimbblet, K. A., Ross, N. P., & Wake, D. 2007, MNRAS, 381, 1197

Hirata, C. M., Padmanabhan, N., Seljak, U., Schlegel, D., & Brinkmann, J. 2004, Phys. Rev. D, 70, 103501

Hivon, E., Górski, K. M., Netterfield, C. B., Crill, B. P., Prunet, S., & Hansen, F. 2002, ApJ, 567, 2

Ho, S., Hirata, C. M., Padmanabhan, N., Seljak, U., & Bahcall, N. 2008, ArXiv e-prints, 801

Hoekstra, H. 2007, MNRAS, 379, 317

Hoekstra, H., Yee, H. K. C., Gladders, M. D., Barrientos, L. F., Hall, P. B., & Infante, L. 2002, ApJ, 572, 55

Hoekstra, H., et al. 2006, ApJ, 647, 116

Holder, G. P., Haiman, Z., Kaplinghat, M., & Knox, L. 2003, ApJ, 595, 13

Hsieh, B. C., Yee, H. K. C., Lin, H., & Gladders, M. D. 2005, ApJS, 158, 161

Hu, W., Eisenstein, D. J., & Tegmark, M. 1998, Phys. Rev. Lett., 80, 5255

Huey, G., Cyburt, R. H., & Wandelt, B. D. 2004, Phys. Rev. D, 69, 103503

Ichikawa, K., Kawasaki, M., & Takahashi, F. 2007, JCAP, 0705, 007

Ichikawa, K., Sekiguchi, T., & Takahashi, T. 2007, ArXiv e-prints, 712

Ichikawa, K. & Takahashi, T. 2006, Phys. Rev. D, 73, 063528

Ilbert, O., et al. 2006, A&A, 457, 841

Iliev, I. T., Mellema, G., Shapiro, P. R., & Pen, U.-L. 2007, MNRAS, 376, 534

Iye, M., et al. 2006, Nature, 443, 186

Izotov, Y. I. & Thuan, T. X. 2004, ApJ, 602, 200

Jaffe, A. H. & Kamionkowski, M. 1998, Phys. Rev. D, 58, 043001

Jedamzik, K. 2004, Phys. Rev. D, 70, 063524

Jenkins, A., Frenk, C. S., White, S. D. M., Colberg, J. M., Cole, S., Evrard, A. E., Couchman, H. M. P., & Yoshida, N. 2001, MNRAS, 321, 372

Jungman, G., Kamionkowski, M., Kosowsky, A., & Spergel, D. N. 1996, Physical Review Letters, 76, 1007

Kamionkowski, M., Kosowsky, A., & Stebbins, A. 1997, Phys. Rev. D, 55, 7368

Kaplinghat, M., Chu, M., Haiman, Z., Holder, G. P., Knox, L., & Skordis, C. 2003, ApJ, 583, 24

Kashikawa, N., et al. 2006, ApJ, 648, 7

Keskitalo, R., Kurki-Suonio, H., Muhonen, V., & Valiviita, J. 2007, JCAP, 0709, 008

Khoury, J., Ovrut, B. A., Steinhardt, P. J., & Turok, N. 2001, Phys. Rev., D64, 123522

Kim, T.-S., Bolton, J. S., Viel, M., Haehnelt, M. G., & Carswell, R. F. 2007, MNRAS, 382, 1657

Kinney, W. H., Kolb, E. W., Melchiorri, A., & Riotto, A. 2006, Phys. Rev., D74, 023502

Koester, B. P., et al. 2007, ApJ, 660, 239

Kogut, A., et al. 2003, ApJS, 148, 161

—. 2007, ApJ, 665, 355

Komatsu, E. & Seljak, U. 2002, MNRAS, 336, 1256

Komatsu, E. et al. 2008, ApJS

Koopmans, L. V. E., Treu, T., Fassnacht, C. D., Blandford, R. D., & Surpi, G. 2003, ApJ, 599, 70

Korn, A. J., Grundahl, F., Richard, O., Barklem, P. S., Mashonkina, L., Collet, R., Piskunov, N., & Gustafsson, B. 2006, Nature, 442, 657

Kosowsky, A. & Turner, M. S. 1995, Phys. Rev. D, 52, 1739

Kravtsov, A. V., Vikhlinin, A., & Nagai, D. 2006, ApJ, 650, 128

Krisciunas, K., et al. 2005, AJ, 130, 2453

Kuo, C. L., et al. 2007, ApJ, 664, 687

Kurki-Suonio, H., Muhonen, V., & Valiviita, J. 2005, Phys. Rev., D71, 063005

Langlois, D. & Riazuelo, A. 2000, Phys. Rev., D62, 043504

Lawson, K. D., Mayer, C. J., Osborne, J. L., & Parkinson, M. L. 1987, MNRAS, 225, 307

Leitch, E. M., Kovac, J. M., Halverson, N. W., Carlstrom, J. E., Pryke, C., & Smith, M. W. E. 2005, ApJ, 624, 10

Lewis, A. 2006, ArXiv Astrophysics e-prints

Lewis, A. & Bridle, S. 2002, Phys. Rev. D, 66, 103511

Lewis, A., Challinor, A., & Lasenby, A. 2000, ApJ, 538, 473

Li, G. L., Mao, S., Jing, Y. P., Mo, H. J., Gao, L., & Lin, W. P. 2006, MNRAS, 372, L73

Lin, W. P., Jing, Y. P., Mao, S., Gao, L., & McCarthy, I. G. 2006, ApJ, 651, 636

Linde, A. 2005, New Astronomy Review, 49, 35

Linde, A. & Mukhanov, V. 1997, Phys. Rev. D, 56, 535

Linde, A. D. 1985, Physics Letters B, 158, 375

Lyth, D. H. & Riotto, A. 1999, Phys. Rept., 314, 1

Lyth, D. H., Ungarelli, C., & Wands, D. 2003, Phys. Rev. D, 67, 23503

Lyth, D. H. & Wands, D. 2002, Phys. Lett. B, 524, 5

Ma, C.-P. 1996, ApJ, 471, 13

Macri, L. M., Stanek, K. Z., Bersier, D., Greenhill, L. J., & Reid, M. J. 2006, ApJ, 652, 1133

Malhotra, S. & Rhoads, J. E. 2006, ApJ, 647, L95

Mangano, G., Melchiorri, A., Mena, O., Miele, G., & Slosar, A. 2007, JCAP, 0703, 006

Mangano, G., Miele, G., Pastor, S., & Peloso, M. 2002, Phys. Lett., B534, 8

Mantz, A., Allen, S. W., Ebeling, H., & Rapetti, D. 2007, ArXiv e-prints, 709

Mason, B. S., et al. 2003, ApJ, 591, 540

Massey, R., et al. 2007, ApJS, 172, 239

Masters, K. L., Springob, C. M., Haynes, M. P., & Giovanelli, R. 2006, ApJ, 653, 861

McDonald, P., et al. 2005, ApJ, 635, 761

McEwen, J. D., Vielva, P., Hobson, M. P., Martínez-González, E., & Lasenby, A. N. 2007, MNRAS, 376, 1211

Meiksin, A. A. 2007, ArXiv e-prints, 711

Melchiorri, A. & Serra, P. 2006, Phys. Rev., D74, 127301

Meléndez, J. & Ramírez, I. 2004, ApJ, 615, L33

Meneghetti, M., Argazzi, R., Pace, F., Moscardini, L., Dolag, K., Bartelmann, M., Li, G., & Oguri, M. 2007, A&A, 461, 25

Miknaitis, G., et al. 2007, ApJ, 666, 674

Miller, C. J., et al. 2005, AJ, 130, 968

Mitchell, J. L., Keeton, C. R., Frieman, J. A., & Sheth, R. K. 2005, ApJ, 622, 81

Miville-Deschenes, M. ., Ysard, N., Lavabre, A., Ponthieu, N., Macias-Perez, J. F., Aumont, J., & Bernard, J. P. 2008, ArXiv e-prints, 802

Mohapatra, R. N., et al. 2005, hep-ph

Montroy, T. E., et al. 2006, ApJ, 647, 813

Moodley, K., Bucher, M., Dunkley, J., Ferreira, P. G., & Skordis, C. 2004, Phys. Rev., D70, 103520

Moroi, T. & Takahashi, T. 2001, Phys. Lett., B522, 215

Mortonson, M. J. & Hu, W. 2008, ApJ, 672, 737

Motl, P. M., Hallman, E. J., Burns, J. O., & Norman, M. L. 2005, ApJ, 623, L63

Muchovej, S., et al. 2007, ApJ, 663, 708

Myers, S. T., et al. 2003, MNRAS, 341, 1

Nagai, D. 2006, ApJ, 650, 538

Neal, R. M. 1993, Technical Report, Tech. Rep. CRG-TR-93-1, University of Toronto

Nesseris, S. & Perivolaropoulos, L. 2008, Phys. Rev. D, 77, 023504

Neto, A. F., et al. 2007, MNRAS, 381, 1450

Nobili, S., et al. 2005, A&A, 437, 789

Nolta, M. R., et al. 2004, Astrophys. J., 608, 10

Nolta, M. R. et al. 2008, ApJS

O'Dwyer, I. J. et al. 2004, Astrophys. J., 617, L99

Oguri, M., et al. 2006, AJ, 132, 999

—. 2008, AJ, 135, 512

Olive, K. A. & Skillman, E. D. 2004, ApJ, 617, 29

O'Meara, J. M., Burles, S., Prochaska, J. X., Prochter, G. E., Bernstein, R. A., & Burgess, K. M. 2006, ApJ, 649, L61

Ota, K., et al. 2007, ArXiv e-prints, 707

P. Ade, et al. 2007, ArXiv e-prints, 705

Padmanabhan, N., et al. 2007, MNRAS, 378, 852

Page, L., et al. 2003, ApJ, 585, 566

—. 2007, ApJS, 170, 335

Park, C.-G. & Park, C. 2006, ApJ, 637, 1

Peacock, J. A., et al. 2001, Nature, 410, 169

Pearson, T. J., et al. 2003, ApJ, 591, 556

Peebles, P. J. E. 1987, Nature, 327, 210

Peebles, P. J. E. & Ratra, B. 1988, ApJ, 325, L17

Peimbert, M., Luridiana, V., & Peimbert, A. 2007, ApJ, 666, 636

Peiris, H. V., et al. 2003, ApJS, 148, 213

Percival, W. J., Cole, S., Eisenstein, D. J., Nichol, R. C., Peacock, J. A., Pope, A. C., & Szalay, A. S. 2007a, MNRAS, 381, 1053

Percival, W. J., et al. 2007b, ApJ, 657, 51

—. 2007c, ApJ, 657, 645

Perlmutter, S., et al. 1999, ApJ, 517, 565

Piacentini, F., et al. 2006, ApJ, 647, 833

Pierre, M., et al. 2006, MNRAS, 372, 591

Pietrobon, D., Balbi, A., & Marinucci, D. 2006, Phys. Rev. D, 74, 043524

Polarski, D. & Gannouji, R. 2007, ArXiv e-prints, 710

Polarski, D. & Starobinsky, A. A. 1994, Phys. Rev., D50, 6123

—. 1995, Phys. Lett., B356, 196

Readhead, A. C. S., et al. 2004, ApJ, 609, 498

Reich, P. & Reich, W. 1988, A&AS, 74, 7

Reichardt, C. L., et al. 2008, ArXiv e-prints, 801

Reid, B. A. & Spergel, D. N. 2006, ArXiv Astrophysics e-prints

Reiprich, T. H. & Böhringer, H. 2002, ApJ, 567, 716

Reyes, R., Mandelbaum, R., Hirata, C. M., Bahcall, N., & Seljak, U. 2008, ArXiv e-prints, 802

Richard, O., Michaud, G., & Richer, J. 2005, ApJ, 619, 538

Ricotti, M. & Ostriker, J. P. 2004, MNRAS, 352, 547

Ricotti, M., Ostriker, J. P., & Mack, K. J. 2007, ArXiv e-prints, 709

Riess, A. G., Press, W. H., & Kirshner, R. P. 1995, ApJ, 438, L17

Riess, A. G., et al. 1998, AJ, 116, 1009

—. 2004, ApJ, 607, 665

—. 2005, ApJ, 627, 579

—. 2007, ApJ, 659, 98

Ross, N. P., et al. 2007, MNRAS, 381, 573

Rozo, E., et al. 2007, ArXiv Astrophysics e-prints

Ruhl, J. E., et al. 2003, ApJ, 599, 786

Rybicki, G. B. & Lightman, A. 1979, Radiative Processes in Astrophysics (Wiley & Sons: New York)

Rykoff, E. S., et al. 2008, ArXiv e-prints, 802

Sand, D. J., Treu, T., Ellis, R. S., & Smith, G. P. 2005, ApJ, 627, 32

Sandage, A., Tammann, G. A., Saha, A., Reindl, B., Macchetto, F. D., & Panagia, N. 2006, ApJ, 653, 843

Schmidt, B. P., et al. 1998, ApJ, 507, 46

Seckel, D. & Turner, M. S. 1985, Phys. Rev. D, 32, 3178

Seljak, U. 1997, ApJ, 482, 6

Seljak, U., Slosar, A., & McDonald, P. 2006, JCAP, 0610, 014

Seljak, U., et al. 2005, Phys. Rev. D, 71, 103515

Shafieloo, A. & Souradeep, T. 2007, ArXiv e-prints, 709

Sheldon, E. S., et al. 2001, ApJ, 554, 881

—. 2007, ArXiv e-prints, 709

Sievers, J. L., et al. 2003, ApJ, 591, 599

—. 2007, ApJ, 660, 976

Slosar, A., Seljak, U., & Makarov, A. 2004, Phys. Rev., D69, 123003

Smith, K. M., Zahn, O., & Doré, O. 2007, Phys. Rev. D, 76, 043510

Spergel, D. N., et al. 2003, ApJS, 148, 175

—. 2007, ApJS, 170, 377

Spitzer, L. 1998, Physical Processes in the Interstellar Medium (Physical Processes in the Interstellar Medium, by Lyman Spitzer, pp. 335. ISBN 0-471-29335-0. Wiley-VCH , May 1998.)

Springob, C. M., Masters, K. L., Haynes, M. P., Giovanelli, R., & Marinoni, C. 2007, ApJS, 172, 599

Srbinovsky, J. A. & Wyithe, J. S. B. 2007, MNRAS, 374, 627

Stark, D. P., Ellis, R. S., Richard, J., Kneib, J.-P., Smith, G. P., & Santos, M. R. 2007, ApJ, 663, 10

Starobinsky, A. A. 1979, ZhETF Pis ma Redaktsiiu, 30, 719

Steigman, G. 2006, International Journal of Modern Physics E, 15, 1

—. 2007, Annual Review of Nuclear and Particle Science, 57, 463

Steigman, G., Schramm, D. N., & Gunn, J. E. 1977, Phys. Lett., B66, 202

Stompor, R., Banday, A. J., & Gorski, K. M. 1996, ApJ, 463, 8

Strauss, M. A. & Willick, J. A. 1995, Phys. Rep., 261, 271

Strong, A. W., Moskalenko, I. V., & Ptuskin, V. S. 2007, Annual Review of Nuclear and Particle Science, 57, 285

Strong, A. W., Moskalenko, I. V., & Reimer, O. 2000, ApJ, 537, 763

Taniguchi, Y., et al. 2005, PASJ, 57, 165

Tegmark, M., et al. 2004, ApJ, 606, 702

—. 2006, Phys. Rev. D, 74, 123507

Totani, T., Kawai, N., Kosugi, G., Aoki, K., Yamada, T., Iye, M., Ohta, K., & Hattori, T. 2006, PASJ, 58, 485

Trotta, R. 2007, Mon. Not. Roy. Astron. Soc. Lett., 375, L26

Trotta, R. & Hansen, S. H. 2004, Phys. Rev. D, 69, 023509

Turner, E. L. 1990, ApJ, 365, L43

Uyaniker, B., Fürst, E., Reich, W., Reich, P., & Wielebinski, R. 1999, A&AS, 138, 31

Valiviita, J. & Muhonen, V. 2003, Phys. Rev. Lett., 91, 131302

Vallée, J. P. 2005, ApJ, 619, 297

van Leeuwen, F., Feast, M. W., Whitelock, P. A., & Laney, C. D. 2007, MNRAS, 379, 723

Van Waerbeke, L., Mellier, Y., & Hoekstra, H. 2005, A&A, 429, 75

Verde, L. & Peiris, H. V. 2008, ArXiv e-prints, 802

Verde, L., et al. 2002, MNRAS, 335, 432

—. 2003, ApJS, 148, 195

Viel, M., Haehnelt, M. G., & Lewis, A. 2006, MNRAS, 370, L51

Viel, M., Weller, J., & Haehnelt, M. G. 2004, MNRAS, 355, L23

Wambsganss, J., Ostriker, J. P., & Bode, P. 2007, ArXiv e-prints, 707

Wandelt, B. D. 2003, ECONF, C030908, WELT001

Wandelt, B. D., Larson, D. L., & Lakshminarayanan, A. 2004, Phys. Rev. D, 70, 083511

Watkins, R. & Feldman, H. A. 2007, MNRAS, 379, 343

Wetterich, C. 1988, Nucl. Phys., B302, 668

Willott, C. J., et al. 2007, AJ, 134, 2435

Wittman, D., Dell'Antonio, I. P., Hughes, J. P., Margoniner, V. E., Tyson, J. A., Cohen, J. G., & Norman, D. 2006, ApJ, 643, 128

Wolleben, M., Landecker, T. L., Reich, W., & Wielebinski, R. 2006, A&A, 448, 411

Wood-Vasey, W. M., et al. 2007, ApJ, 666, 694

Wright, E. L. 2007, ApJ, 664, 633

Wright, E. L. et al. 2008, ApJS

Wyithe, J. S. B., Bolton, J. S., & Haehnelt, M. G. 2008, MNRAS, 383, 691

Wyithe, J. S. B. & Loeb, A. 2003, ArXiv Astrophysics e-prints

York, T., et al. 2005, MNRAS, 361, 259

Yoshida, N., Bromm, V., & Hernquist, L. 2004, ApJ, 605, 579

Zaldarriaga, M. & Seljak, U. 1997, Phys. Rev. D, 55, 1830

Zaroubi, S., Bernardi, M., da Costa, L. N., Hoffman, Y., Alonso, M. V., Wegner, G., Willmer, C. N. A., & Pellegrini, P. S. 2001, MNRAS, 326, 375

Zunckel, C. & Ferreira, P. G. 2007, Journal of Cosmology and Astro-Particle Physics, 8, 4